

EXPERIMENTAL INVESTIGATIONS INTO  
HIGH-ALTITUDE RELIGHT  
OF A GAS TURBINE



Robert William Read  
Homerton College  
University of Cambridge

This dissertation is submitted for  
the degree of Doctor of Philosophy

2008

*To my mother and father*

## Declaration

I hereby declare that this dissertation is the result of my own work and contains nothing that is the outcome of work done in collaboration except as declared in the preface and specified in the text. Furthermore, this dissertation is not substantially the same as any that I have submitted or will be submitting for a degree, diploma, or other qualification at this or any other University. The word and figure limit prescribed by the Engineering Degree Committee has not been exceeded.

Robert William Read

January 3, 2009

## Abstract

This thesis describes experiments to investigate high-altitude relight of a lean direct injection (LDI) combustor. The features that make LDI technology less polluting in terms of  $\text{NO}_x$  compared to conventional combustors are expected to impede relight performance. Therefore an improved understanding of ignition behaviour is required to ensure that stringent relight requirements can be satisfied.

Realistic operating conditions are simulated in a ground-based test facility. The application of laser diagnostics presents particular difficulties due to the large quantities of liquid fuel that impinge on the combustor walls during relight. Advances are made in the application of planar laser-induced fluorescence (PLIF) to monitor fuel placement in a combustor under these conditions. A novel apparatus is developed to deliver a laser sheet to the combustion chamber while protecting all optical surfaces from contamination. The PLIF images are compared with the cold flow field obtained from CFD modelling. These results indicate that fuel becomes trapped inside the central recirculation zone in high concentrations.

High-speed flame imaging performed simultaneously with the PLIF measurements provides important insights into the motion and breakup of flame during relight. An algorithm developed to track the flame activity reveals that the initial spark kernel is convected downstream, before breaking apart and moving upstream towards a recovery origin close to the fuel injector. Analysis of many ignition events has revealed several distinct modes of ignition failure.

Keywords: altitude relight, planar laser-induced fluorescence (PLIF), gas turbine, lean direct injection, spark ignition.

## Acknowledgements

I would like to thank my supervisor, Simone Hochgreb, for her support and guidance. Thanks also to my adviser, Nondas Mastorakos, particularly for the generous loan of his high-speed camera.

I owe a large debt of gratitude to my colleague and friend Jim Rogerson whose technical contribution, most notably to the development of the flame tracking algorithm, has generated key insights into the relight process. His editorial suggestions have improved the quality of this dissertation significantly, and his gentle encouragement has been much appreciated.

This work has been supported by Rolls-Royce plc and I would like to express my gratitude to the engineers at Derby, who have provided considerable technical assistance. My particular thanks go to Ken Young, Peter Schober, Mike Whiteman, Kevin Ronan, and Steve Harding. Chris Goddard and Marco Zedda generated valuable CFD data, and discussions with Arthur Rowe provided insight into gas turbine performance at altitude relight conditions. I am also grateful to the technical staff at the Strategic Research Centre, particularly Allan Collard and Peter Athey, who offered extensive help during experimental testing.

I thank the members of the Heat Gallery for providing the most stimulating of intellectual and social environments. Special thanks are due to Bryn Jones for sharing his knowledge of gas turbine design with both patience and alacrity, and to James Dawson, who provided many fruitful research ideas. The assistance of the workshop staff in the Engineering Department was also much appreciated with special thanks to Alistair Ross, Neil Houghton, and Davor Dukic for their expert design advice and uplifting good humour.

My mother and father have provided a continual source of support during my life and I thank them for giving me the curiosity to embark on a PhD, and the determination to see it through. My final thanks to Kathryn for her limitless love and encouragement.

# Contents

List of tables	ix
List of figures	xi
Nomenclature	xiv
<b>1 Introduction</b>	<b>1</b>
<b>2 Background</b>	<b>6</b>
2.1 The combustion system . . . . .	6
2.2 Altitude restart . . . . .	10
2.2.1 Restart conditions . . . . .	10
2.2.2 The restart process . . . . .	17
2.2.3 Design for altitude restart . . . . .	19
2.3 Review of ignition and flame stabilisation . . . . .	23
2.3.1 Paradigms of ignition research . . . . .	24
2.4 Fundamental experiments to study ignition . . . . .	33
2.4.1 Ignition of gaseous blends . . . . .	34
2.4.2 Quiescent droplet suspensions . . . . .	41
2.4.3 Flowing heterogeneous mixtures . . . . .	47
2.4.4 Laboratory-scale relight experiments . . . . .	51

---

<b>3</b>	<b>Experimental Method</b>	<b>55</b>
3.1	The altitude test facility . . . . .	55
3.1.1	Layout . . . . .	55
3.1.2	Operating condition set points . . . . .	58
3.2	PLIF . . . . .	59
3.2.1	Background . . . . .	59
3.2.2	Beam delivery configuration . . . . .	62
3.2.3	Optical table . . . . .	63
3.2.4	Periscope and sheet expansion assembly . . . . .	66
3.2.5	Air purges . . . . .	73
3.3	High-speed flame imaging . . . . .	79
3.3.1	Background . . . . .	79
3.3.2	Viewing angle . . . . .	81
3.4	Timing and data acquisition . . . . .	83
3.4.1	General setup . . . . .	84
3.4.2	Cold fuel imaging . . . . .	87
3.4.3	Fuel and flame imaging at unsafe condition . . . . .	87
3.4.4	Fuel and flame imaging at safe condition . . . . .	89
3.4.5	Test numbers . . . . .	90
<b>4</b>	<b>Results I: Preliminary Analysis</b>	<b>91</b>
4.1	Operating conditions . . . . .	91
4.2	Properties of laser beam and sheet . . . . .	92
4.2.1	Dye fluorescence . . . . .	93
4.2.2	Slit traverse . . . . .	94
4.3	Characteristic times . . . . .	96
4.3.1	Recovery and failure times . . . . .	96
4.3.2	Classification of PLIF images . . . . .	99
4.4	Spark effects . . . . .	100

---

4.4.1	Measured spark parameters . . . . .	102
4.4.2	Interaction between successive sparks . . . . .	105
<b>5</b>	<b>Results II: Fuel Imaging</b>	<b>109</b>
5.1	Analysis of uncorrected PLIF images . . . . .	109
5.1.1	Individual cold images . . . . .	109
5.1.2	Mean cold images . . . . .	115
5.1.3	Influence of flame . . . . .	120
5.2	PLIF image correction . . . . .	125
5.2.1	Scattering and reflections . . . . .	126
5.2.2	Sheet thickness . . . . .	129
5.2.3	Frontal area . . . . .	130
5.2.4	Beam energy distribution . . . . .	131
5.2.5	Interpretation of corrected images . . . . .	136
5.3	CFD comparison . . . . .	138
<b>6</b>	<b>Results III: Flame Imaging</b>	<b>141</b>
6.1	Flame tracking software . . . . .	141
6.1.1	Search principle . . . . .	142
6.1.2	Algorithm features . . . . .	143
6.2	Developing flame . . . . .	149
6.2.1	Flame trajectories . . . . .	149
6.2.2	Flame size distributions . . . . .	155
6.2.3	Spark kernel velocities . . . . .	159
6.3	Successful ignition . . . . .	162
6.3.1	Flame velocities . . . . .	162
6.3.2	Recovery origin . . . . .	165
6.3.3	Frequency content . . . . .	168
6.4	CFD comparison . . . . .	171

---

<b>7 Conclusion</b>	<b>173</b>
7.1 Operation of test facility . . . . .	173
7.1.1 Apparatus modifications . . . . .	174
7.1.2 Apparatus characterisation . . . . .	175
7.2 Main findings of fuel and flame imaging . . . . .	176
7.3 Recommendations for future work . . . . .	178
7.3.1 Measures to improve LDI relight performance . . . . .	178
7.3.2 Further investigations . . . . .	179
<b>Appendices</b>	<b>180</b>
<b>A Viewing Angle Corrections</b>	<b>181</b>
<b>B Geometry of Laser Sheet</b>	<b>185</b>
B.1 Lens calculations . . . . .	185
B.2 Frontal area calculation . . . . .	188
<b>References</b>	<b>191</b>

# List of Tables

2.1	Experiments investigating ignition of gaseous mixtures . . . . .	35
2.2	Experiments investigating ignition of quiescent aerosols . . . . .	36
2.3	Experiments investigating ignition of flowing droplet mixtures . . . . .	37
3.1	Safe and unsafe condition set points for relight testing . . . . .	59
3.2	Beam dimensions at principal point of each lens . . . . .	71
3.3	Number of tests recorded with high-speed flame camera . . . . .	90
3.4	Number of tests recorded with PLIF camera . . . . .	90
4.1	Experimental operating conditions during ignition testing . . . . .	92
4.2	Classification of PLIF images . . . . .	100
4.3	Mean measured spark parameters . . . . .	103
4.4	Standard deviation of measured spark parameters . . . . .	103
5.1	Region A PLIF intensity statistics . . . . .	118
5.2	Region B PLIF intensity statistics . . . . .	127
6.1	Ignition activity in three regions of the combustor . . . . .	153
6.2	Flame-centroid and CFD velocities at safe condition . . . . .	159
6.3	Flame-centroid and CFD velocities at unsafe condition . . . . .	159
A.1	Calibration target vertex coordinates . . . . .	184
A.2	Viewing angle transformation matrices and scaling factors . . . . .	184

---

B.1 Dimensions and focal distances of sheet-formation lenses . . . . . 187

# List of Figures

2.1	Aviation gas turbine combustor concepts . . . . .	8
2.2	The standard atmosphere . . . . .	11
2.3	Combustor entry conditions . . . . .	14
2.4	Ignition and stability loops . . . . .	21
2.5	Temperature profiles after point energy deposition . . . . .	26
3.1	Photograph of experimental apparatus . . . . .	56
3.2	The modified test section . . . . .	57
3.3	Fluorescence spectrum of Jet A fuel . . . . .	61
3.4	The optical table . . . . .	65
3.5	Laser beam path through modified test section . . . . .	67
3.6	The periscope assembly . . . . .	68
3.7	Excitation volume . . . . .	72
3.8	The combustor window purge system . . . . .	74
3.9	Air purge characteristic curves . . . . .	77
3.10	The periscope and sheet expansion purge systems . . . . .	78
3.11	Spectral sensitivity of high-speed camera . . . . .	81
3.12	Plan view of test section including cameras . . . . .	82
3.13	Timing and data acquisition hardware . . . . .	85
3.14	Timing of data acquisition . . . . .	86
4.1	Dye fluorescence measurements of beam energy profile . . . . .	94

---

4.2	Slit traverse measurements of beam and sheet energy profiles . . . . .	96
4.3	Definition of recovery and failure times . . . . .	98
4.4	Cumulative frequency plot of recovery and failure times . . . . .	99
4.5	Image of spark discharge . . . . .	101
4.6	Histograms of measured spark parameters . . . . .	104
4.7	Distributions of successful spark number . . . . .	106
5.1	Uncorrected, individual, safe, cold PLIF image . . . . .	110
5.2	Uncorrected, individual, unsafe, cold PLIF image . . . . .	111
5.3	Cold PLIF details . . . . .	112
5.4	Cold PLIF details with logarithmic scale . . . . .	113
5.5	High speed images of cold flow . . . . .	114
5.6	Uncorrected, mean, cold PLIF images . . . . .	116
5.7	Uncorrected, mean, cold PLIF image with logarithmic scale . . . . .	117
5.8	Histograms of cold PLIF signal in region A . . . . .	119
5.9	Scatter plot of PLIF intensity versus flame intensity . . . . .	120
5.10	Simultaneous images of fuel and flame . . . . .	122
5.11	Simultaneous images of fuel and high-intensity flame . . . . .	123
5.12	Fuel droplets following flame stabilisation . . . . .	124
5.13	Uncorrected, individual, cold PLIF image with logarithmic scale . . . . .	127
5.14	Histograms of cold PLIF signal in region B . . . . .	128
5.15	Radial correction effects . . . . .	132
5.16	Comparison of beam energy profile and fluorescence signal . . . . .	134
5.17	Angular correction effects . . . . .	135
5.18	Corrected, mean, cold PLIF images . . . . .	137
5.19	Time-averaged velocity in sheet plane predicted by CFD . . . . .	139
6.1	Flame tracking process . . . . .	142
6.2	Kernel search process . . . . .	144
6.3	Expanded search process . . . . .	146

---

6.4	Early high-speed images and corresponding kernel outlines . . . . .	147
6.5	Trajectory plot example . . . . .	148
6.6	Safe and unsafe flame trajectory plots . . . . .	150
6.7	Trajectory plots of safe failures . . . . .	152
6.8	Flame detection times in fuel-injector region . . . . .	154
6.9	Points of last activity during failed ignition events . . . . .	155
6.10	Variation in imaged flame area with time . . . . .	156
6.11	Distributions of measured kernel size . . . . .	158
6.12	Spark stream-wise velocity at safe condition . . . . .	161
6.13	Flame velocity development maps . . . . .	163
6.14	Average flame velocity development map . . . . .	164
6.15	Flame intensity variations during successful ignition . . . . .	165
6.16	Kernel number density map example . . . . .	166
6.17	Kernel number density maps . . . . .	167
6.18	Stabilised flame oscillations . . . . .	169
6.19	Spectral analysis of measured flame intensity signal . . . . .	170
6.20	Phase shift of stabilised flame oscillations relative to spark . . . . .	171
6.21	CFD streamlines passing below igniter tip . . . . .	172
A.1	Rotated square . . . . .	181
B.1	Sheet-formation optics . . . . .	186
B.2	Laser sheet geometry . . . . .	189

# Nomenclature

## Terms

safe	test condition conducive to successful ignition	} see Table 3.1
unsafe	test condition that prevents successful ignition	

## Abbreviations

AFR	air-to-fuel ratio
ATF	altitude test facility
CRZ	central recirculation zone
DNS	direct numerical simulation
FAR	fuel-to-air ratio
LDI	lean direct injection
LES	large-eddy simulation
PAH	polycyclic aromatic hydrocarbons
PLIF	planar laser-induced fluorescence
RANS	Reynolds-averaged Navier-Stokes
SMD	Sauter mean diameter

# Chapter 1

## Introduction

Air safety regulations demand that gas turbine manufacturers provide a means of restarting an engine at high altitude in the event of a flame-out (Federal Aviation Administration 2000; European Aviation Safety Agency 2003). Future-generation low- $\text{NO}_x$  combustors currently in development create a high-velocity, fuel-lean zone close to the spark igniter that has the potential to inhibit restart performance. Little research has been conducted to investigate this problem. The experimental study described here aims to increase understanding of ignition and flame stabilisation inside a lean direct injection (LDI) combustor operating at altitude restart conditions.

To understand the circumstances which have led to the development of the LDI concept, let us consider the three factors that dominate the design of modern aviation gas turbines: fuel consumption, noise, and emissions. In today's engines, fuel consumption and noise are largely controlled by overall engine design parameters such as the pressure ratio, turbine inlet temperature, and bypass ratio. They are also influenced by the detailed design of the compressor and turbine. The combustion system liberates virtually all of the heat present in the fuel and generates comparatively little noise directly, but is the major factor governing engine emissions. Hence the combustor design is heavily influenced by regulations governing emissions of carbon monoxide (CO), unburned hydrocarbons (UHC), smoke, and nitrogen

oxides ( $\text{NO}_x$ ) emitted during a standard landing-takeoff cycle (International Civil Aviation Organisation 2006).

For conventional combustion systems, the reduction of  $\text{NO}_x$  emissions presents the greatest challenge. Oxides of nitrogen are toxic to human health when emitted at ground level (Kampa and Castanas 2008), and react to increase ozone levels in the upper troposphere and lower stratosphere when deposited at altitude (Penner et al. 1999). Ozone is a greenhouse gas that also leads to the generation of photochemical smog in the lower atmosphere. As a consequence of these effects, nitrogen oxide emissions have been regulated with increasing stringency during recent years, and ambitious goals have been set for further reductions in the future (Advisory Council for Aeronautics Research in Europe 2002). While  $\text{NO}_x$  refers to both nitric oxide (NO) and nitrogen dioxide ( $\text{NO}_2$ ), NO produced via the extended Zeldovich or thermal mechanism constitutes the majority of the nitrogen oxides generated in a non-premixed combustion system (Glassman 1996). The formation rate of thermal NO increases rapidly when the flame temperature exceeds approximately 1800 K (Turns 1996).

Today's production engines restart readily at altitudes of up to 30000 ft (9.1 km) above sea level using conventional combustor designs, thanks to the stoichiometric, low-velocity conditions generated in the region between the fuel injector and the spark igniter. However, the high temperatures associated with stoichiometric combustion generate  $\text{NO}_x$  in concentrations that cannot be reduced below a certain level using conventional combustor technology. Changes in stoichiometry may limit formation of NO and  $\text{NO}_2$ , but the associated reduction in flame temperature tends to increase production of CO. The central objective of all low-emissions technology is therefore to maintain the combustion zone temperature within a narrow band between approximately 1670 K and 1900 K across the full engine power range.

A variety of alternative low- $\text{NO}_x$  combustor design concepts are presently being evaluated for aeronautical use. The lean premixed prevapourised (LPP) combustor

is a promising concept for low-NO<sub>x</sub> combustion of liquid fuels (Canepa et al. 2006; Allouis et al. 2008). The principle of operation is to create a fully homogeneous fuel-air mixture prior to combustion with an equivalence ratio close to the lean flammability limit ( $\phi \approx 0.6$ ). The comparatively low flame temperature that results produces a low concentration of NO<sub>x</sub> that does not increase with residence time. The thorough premixing of fuel and air coupled with extended residence times ensures that emissions of CO and UHC are also low. However, the principal difficulty with this approach is that the time required for vapourisation and mixing in the fuel preparation duct can exceed the autoignition delay time at high power (Brandt et al. 1997). The resulting migration of flame poses a safety hazard. Furthermore, LPP systems are prone to damaging thermoacoustic instabilities that result from a feedback between pressure and heat release (Dowling and Hubbard 2000). These concerns have so far limited the use of LPP combustors to ground-based gas turbines.

The rich-burn/quick-quench/lean-burn (RQL) combustor is a low-NO<sub>x</sub> design concept that is also being developed (Anacleto et al. 1996; Blomeyer et al. 1999). A fuel-rich primary combustion zone is created where NO<sub>x</sub> formation is limited by the low reaction temperatures and a lack of oxygen. The additional air required to ensure full oxidation and to reduce the exit gas temperature is injected into a secondary zone in a manner that ensures rapid and uniform mixing with the primary zone gases. Compared to a conventional design, the RQL combustor has inherently stronger ignition and lean blowout performance. However, improvements in the effectiveness of the secondary mixing are required to deliver the full benefits of this concept (Lefebvre 1995).

The principle of modifying the equivalence ratio in two or more combustion zones according to the engine power setting has been investigated more generally. A variable geometry arrangement can be used to adjust the distribution of air between the primary and dilution zones of a conventional combustor to maintain a consistent primary zone flame temperature (Gupta et al. 1991; Li and Hales 2003). Alterna-

---

tively, the added weight and complexity of a variable geometry mechanism may be avoided by using staged combustion systems such as lean direct injection. An example of a LDI design is the low- $\text{NO}_x$  combustion system developed by Rolls-Royce plc as part of the ANTLE (advanced near-term low-emissions) programme. In this combustor, a central pilot atomiser creates a comparatively rich mixture close to the combustor centre-line, providing low-power stability. The additional fuel required for high-power operation is introduced through a larger diameter main atomiser, mounted concentrically with the pilot. At take-off and cruise, a lean flame is created around the pilot by admitting a large proportion of the engine air-flow through the fuel injector. At the pilot-only altitude restart condition, a comparatively high-velocity, fuel lean region is thus generated between the igniter and the fuel injection point. These features hinder the processes of ignition, flame propagation and flame stabilisation required to successfully restart the engine.

This thesis describes an investigation into ignition and flame stabilisation inside a LDI combustor sector operating under altitude restart conditions. Chapter 2 presents background information concerning the altitude restart requirement and its context in the overall engine design process. A survey of fundamental combustion research describing ignition of gaseous and droplet mixtures and flame development in simplified flow geometries is also included.

Experimental testing was conducted using the altitude test facility (ATF) at the Rolls-Royce Strategic Research Centre, Derby, UK. The fuel and flame distributions inside the combustion chamber were recorded using kerosene planar laser-induced fluorescence (PLIF) and high-speed flame emission imaging respectively, as described in Chapter 3. Also presented in this chapter are novel measures to enable high-resolution imaging at the restart condition, where the presence of liquid fuel impinging on optical surfaces makes PLIF unusually difficult.

Having established the experimental apparatus, preliminary results are used in Chapter 4 to characterise the operational variability of the facility including such

---

factors as flow rates, spark performance, and laser energy. The results of the PLIF measurements are analysed in detail in Chapter 5, where the fuel placement prior to the spark is identified, and the effect of flame on the PLIF signal is also assessed. Chapter 6 is concerned with interpretation of the high-speed flame recordings. The development of image processing software to analyse the motion and breakup of flame is described in some depth. The findings from the simultaneous PLIF and flame imaging experiments are summarised in Chapter 7, where recommendations for further work are also given.

# Chapter 2

## Background

### 2.1 The combustion system

The role of the combustion system in a gas turbine is to heat the compressor outlet air before it flows to the turbine. This is invariably achieved in aviation applications by generating a kerosene-fuelled flame that releases stored chemical energy as it burns. To maximise the efficiency of the gas turbine cycle, the fuel must be fully oxidised whilst ensuring that the air-flow through the combustion chamber experiences the smallest possible stagnation pressure drop.

This task is complicated, however, by various additional design requirements. Ignition of the fuel-air mixture must occur reliably, both on the ground during start-up and at high altitude following flame extinction. Once established, the flame must remain stable and free from combustion-induced oscillations when subjected to the wide-ranging inlet conditions and fuel-to-air ratios that occur during different phases of the flight cycle. A uniformly distributed hot gas must be delivered to the turbine, containing minimal concentrations of CO, UHC, smoke, and  $\text{NO}_x$ . In addition, the combustion system as a whole must be small, light, durable, and simple to manufacture and maintain. This set of conflicting requirements constitutes a formidable design challenge that requires a large degree of technical compromise.

Figure 2.1(a) illustrates the concept most widely employed to satisfy these design requirements in production aviation gas turbines (Nicholas 2005). Air leaves the compressor with a velocity of approximately 150 m/s. Since the pressure drop associated with combustion is proportional to the square of the air velocity, an inlet diffuser slows the flow velocity to around 100 m/s. To further reduce the velocity to a level that can sustain a hydrocarbon flame, less than half of the air-flow is introduced into an upstream region of the flame tube known as the primary combustion zone. Roughly 10% of the flow is directed into this zone through one or more swirlers situated close to the fuel injection point. Vortex breakdown associated with the induced swirl generates a highly-turbulent region of strongly recirculating flow, referred to as the central recirculation zone (CRZ).

Liquid kerosene fuel is injected into the primary combustion zone in the form of a finely atomised spray. Droplets are formed either by forcing the liquid through a small orifice under pressure, or by using the momentum of the air to create shear between the liquid and gas phases, thereby inducing atomisation. The fuel-air reaction occurs in the gas phase on a molecular scale, and the highly turbulent air-flow in the primary zone is therefore designed to cause rapid evaporation of the liquid kerosene and fast fuel-air mixing.

The comparatively low-velocity recirculating flow in this region is conducive to flame development and stabilisation, and the tip of the spark igniter that provides the ignition energy is therefore often situated at the edge of the primary zone. Following successful ignition, recirculation of the combustion products stabilises the flame by providing a high-temperature source to ignite the incoming fuel-air mixture. This feature ensures stable flame operation across a wide range of flow conditions and air-to-fuel ratios (AFR). Moreover, the turbulent diffusivity increases in direct proportion to the air flow rate, producing an increase in the fuel-air mixing rate (Cant and Mastorakos 2008). The size of flow structures such as the CRZ are thus insensitive to changes in bulk velocity, allowing operation of fixed volume

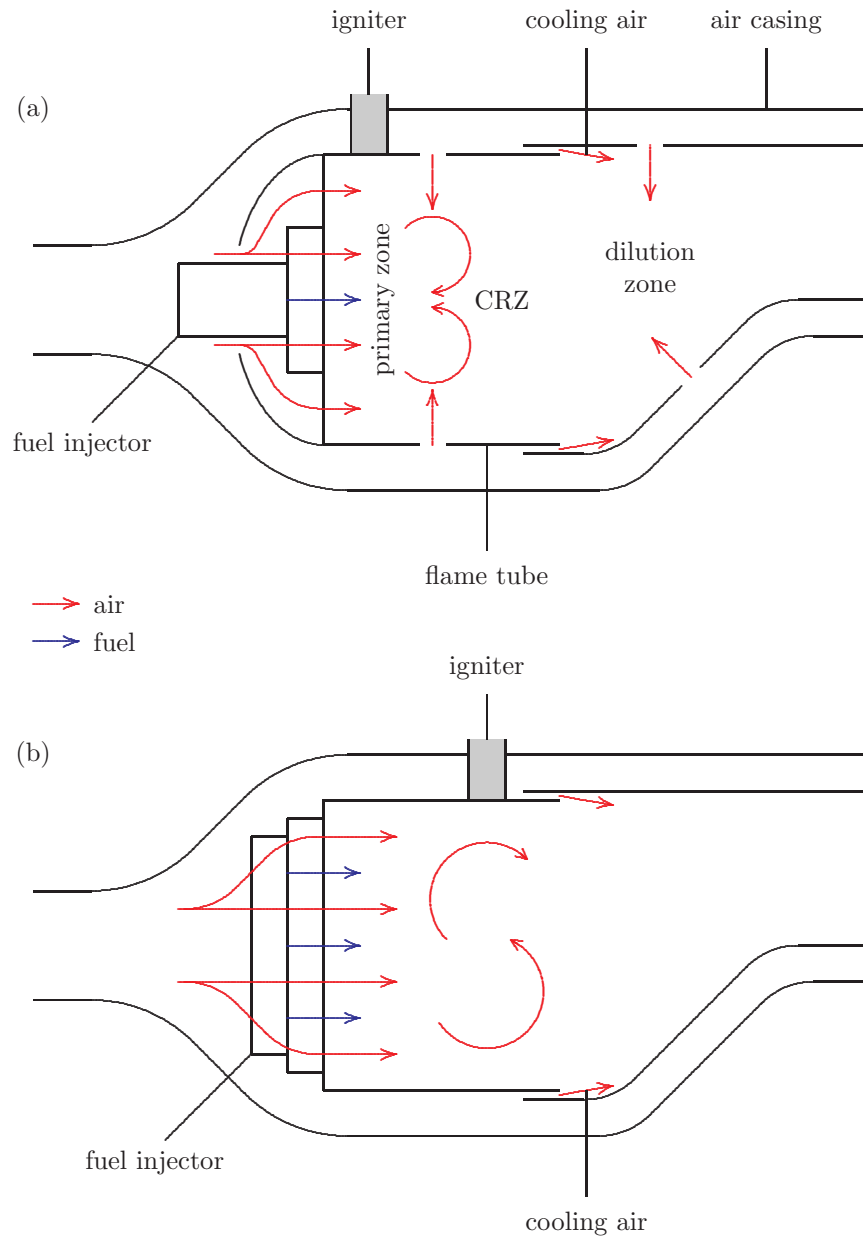


Fig. 2.1: Gas turbine combustor concepts: (a) conventional; (b) LDI ANTLE.

combustors across a range of flow rates without any increase in flame length. At high-power conditions, fuel and air are introduced into the primary combustion zone in roughly stoichiometric proportions, and the high temperature, pressure, and turbulence intensity are sufficient to achieve essentially complete combustion of the fuel-air mixture.

The high air pressure produced by the compressor coupled with the intense fuel-air mixing resulting from an extremely high turbulence intensity lead to remarkable rates of heat release. In the primary zone of a typical aviation gas turbine combustor the heat release rate at take-off is approximately  $500 \text{ MW/m}^3$  – 100 times more intense than that generated in the furnace of a large coal-fired power-plant (Hill and Peterson 1992). The temperature of the hot gases produced by such a flame is approximately 2400 K, and this is sufficiently high to damage the walls of the flame tube. Approximately 40% of the combustor air-flow is therefore employed to protect these surfaces. The remaining 20% of the flow is introduced into the dilution zone, where it mixes with the primary zone gases to generate an exit flow with a temperature distribution acceptable to the turbine.

A comparison of Figures 2.1(a) and 2.1(b) indicates that the flow conditions and fuel placement in the low- $\text{NO}_x$  LDI ANTLE combustor introduced in Chapter 1 are substantially different from those generated inside the conventional combustor described above. The principal difference is the large increase in the proportion of the air-flow passing through the fuel injector – some 65% compared to the 10% typical for a conventional design. The velocities in the upstream portion of the ANTLE combustion chamber are thus comparatively high, and a conventional primary combustion zone cannot be identified. The AFR adjacent to the igniter tip also varies with the configuration. In a conventional combustor, the spark igniter and the fuel injector are separated by a small distance, with a comparatively rich fuel-air mixture created in the space between them. In contrast, the distance between the ANTLE igniter and injector is large, with a particularly lean mixture expected immediately

below the igniter tip. This combination of increased velocity and reduced equivalence ratio has the potential to hinder the combustion processes required to achieve altitude restart. It is this concern that has prompted the present experimental study of the processes occurring inside the ANTLE combustion chamber during altitude restart.

## 2.2 Altitude restart

High-altitude flame extinction inside a gas turbine can be caused by transient disturbances to the air-flow through the engine, or by severe ingestion of ice, water, or dust. Though such an event is rare, the capability to perform an in-flight engine restart is mandatory. American and European air safety authorities presently require the submission and validation of a flight envelope defining restart capability (Federal Aviation Administration 2000; European Aviation Safety Agency 2003). This section considers the conditions generated inside the combustor following flame-out, and the influence of the engine restart requirement on the overall combustor design.

### 2.2.1 Restart conditions

The conditions inside a gas turbine combustor following a high-altitude flame-out vary with both the altitude and the flight speed of the aircraft. The International Civil Aviation Organisation has formulated a standard atmosphere to represent the variation in air temperature, pressure, and density as a function of altitude (International Civil Aviation Organisation 1993). Subsonic civil aircraft fly in the troposphere and lower stratosphere at an average cruise altitude of between 35000 and 38000 ft (10.5 and 11.5 km) (Penner et al. 1999). The atmospheric temperature, pressure and density at altitudes up to 20 km above sea level are plotted in Figure 2.2. These data are expressed as a fraction of their sea-level values.

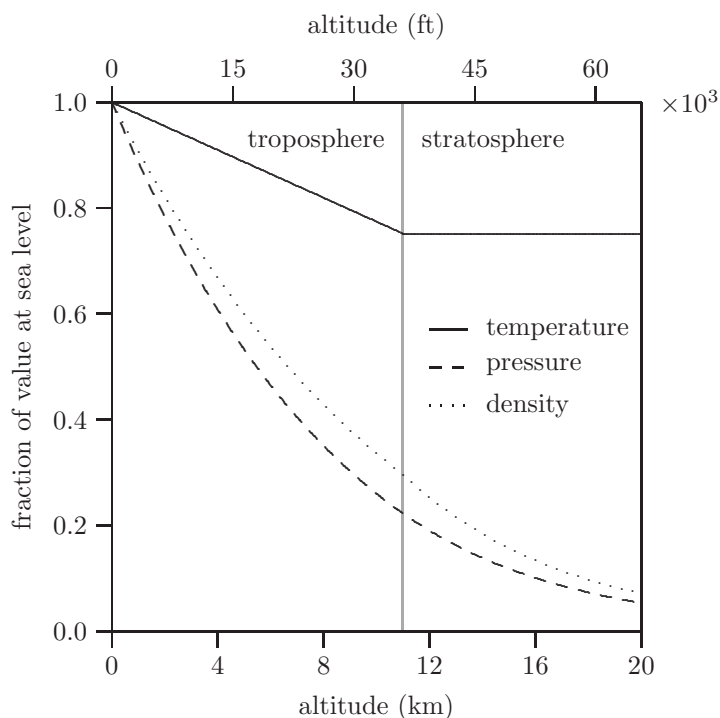


Fig. 2.2: The standard atmosphere. Each parameter is plotted as a fraction of its value at sea level ( $T_{sl} = 288.15$  K,  $P_{sl} = 101.3$  kPa, and  $\rho_{sl} = 1.23$  kg/m<sup>3</sup>).

The standard atmosphere is based on average values recorded at a latitude of 45° N, and significant excursions from the plotted data occur with location and season. The temperature varies more than the pressure in this respect, and these fluctuations are greatest close to the ground. For example, it is not uncommon for the ground temperature at an airport to range from  $-40$  °C to  $40$  °C. Sufficient margin must be provided for these variations to ensure engine ground start-up capability.

Figure 2.2 shows that the temperature, pressure, and density all decrease with altitude. It is assumed that below the tropopause (11 km above sea level) the temperature falls linearly at a rate of 6.5 K/km, while above the tropopause the temperature remains constant at 216.65 K. The pressure at a given altitude is given

by

$$P = P_{sl} \left( \frac{T}{T_{sl}} \right)^{g/kR}, \quad (2.1)$$

where  $g$  is the acceleration due to gravity at sea level,  $k$  is the rate of decrease of temperature with altitude, and  $R$  is the gas constant for dry air. From the ideal gas law, the density is then

$$\rho = \frac{P}{RT}. \quad (2.2)$$

Though strongly influenced by the temperature and pressure outside the aircraft, the thermodynamic conditions inside the combustor also vary with flight speed. In addition, the conditions are affected by various engine design parameters including the bypass ratio, power offtake, and exhaust configuration (Braig et al. 1999). In this study, a simplified analysis has been performed to illustrate changes in the combustor conditions with flight condition. Software has been developed to calculate the combustor inlet air temperature, pressure and mass flow rate corresponding to a range of flight Mach numbers and altitudes. These results are presented in Figure 2.3.

Calculations of the combustor inlet conditions were based on several assumptions concerning the air-flow through the engine. Following an in-flight flame-out, the gas turbine cools rapidly and the engine spools decelerate to a comparatively low speed which is maintained by the ram pressure at the compressor inlet. Immediately prior to a restart attempt, the heat and work transfers from the compressor to the air-flow are therefore negligible. In addition, the velocity inside the combustion chamber is only a small fraction of the flight speed. It is therefore valid to assume that the combustor inlet temperature is equal to the stagnation temperature defined by the speed and altitude of the aircraft. Thus, the combustor temperature is given by

$$T_c = T \left[ 1 + \left( \frac{\gamma - 1}{2} \right) M^2 \right], \quad (2.3)$$

where  $T$  is the atmospheric temperature at the flight altitude,  $\gamma$  is the specific heat ratio of dry air, and  $M$  is the flight Mach number. While the stagnation temperature

of the air is not significantly modified as it passes through the compressor, the rotating blades generate highly irreversible, non-isentropic flow processes, leading to a significant drop in stagnation pressure between the engine inlet and the combustion chamber. It is reasonable to assume that half of the engine inlet dynamic head is lost in the compressor (Rowe 2005), and in this case the combustor inlet pressure is given by

$$P_c = \frac{P_0 + P}{2}, \quad (2.4)$$

where  $P_0$  is the engine inlet stagnation pressure and  $P$  is the atmospheric pressure at the flight altitude. Since the flow velocity inside the combustion chamber is comparatively low, the static and stagnation values of both temperature and pressure are approximately equal.

The total mass flow rate of air through the engine is controlled by the throat area of the nozzle guide vanes (NGV) situated at the entrance to the high-pressure turbine. A one-dimensional compressible flow calculation has been performed to calculate the mass flow rate. This calculation assumes that the air-flow through the NGV is steady, adiabatic, and isentropic. If it is also assumed that the pressure drop across the NGV represents two thirds of the drop between the combustion chamber and the engine exhaust, then the Mach number at the nozzle throat is

$$M = \left[ \frac{2}{\gamma - 1} \left( \left( \frac{P_c}{P_t} \right)^{\gamma-1/\gamma} - 1 \right) \right]^{1/2}, \quad (2.5)$$

where  $P_t$  is the static pressure at the throat. This may be expressed in terms of the combustion chamber pressure as follows

$$P_t = \frac{P_c + 2P}{3}. \quad (2.6)$$

The air mass flow rate through the engine is given by

$$\dot{m} = AMP_c \sqrt{\frac{\gamma}{RT_c}} \left[ 1 + \left( \frac{\gamma - 1}{2} \right) M^2 \right]^{-(\gamma+1)/2(\gamma-1)}, \quad (2.7)$$

where  $A$  is the total throat area of the NGV.

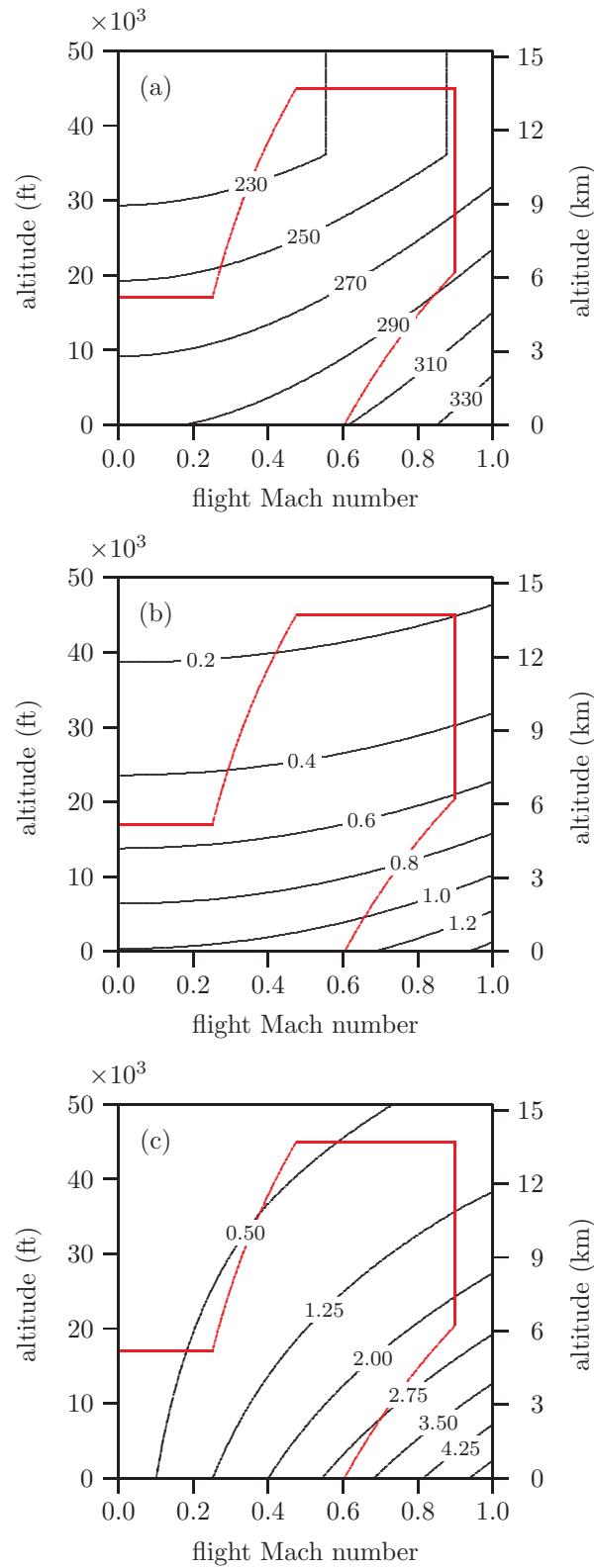


Fig. 2.3: Combustor entry conditions: (a) temperature (K); (b) pressure (bar); (c) mass flow rate (kg/s). A typical flight envelope is shown in red.

Figure 2.3 illustrates that an increase in altitude at a fixed flight Mach number leads to a decrease in combustion chamber air temperature, pressure and mass flow rate. Conversely, an increase in flight Mach number at a fixed altitude increases the temperature, pressure and mass flow rate inside the combustion chamber.

Airframe and engine manufacturers agree a maximum restart altitude that typically ranges from 20000 to 30000 ft (6.1 to 9.1 km) above sea level. Following a flame-out at 30000 ft, the combustor inlet temperature and pressure are typically 265 K and 0.4 bar respectively. Furthermore, the air mass flow rate through the combustion chamber is much lower than that generated at cruise, resulting in lower combustor flow velocities. Despite the reduced velocities the Reynolds number remains extremely high, and the flow is consequently highly turbulent.

These operating conditions impede several key physical and chemical mechanisms required to achieve high-altitude restart. Perhaps foremost amongst these is atomisation of the liquid kerosene fuel. As noted in Section 2.1, the air-blast atomiser that is often employed in modern gas turbine combustion systems operates by creating a high-velocity airstream to fragment a sheet of fuel discharged from the edge of a pre-filming surface. The comparatively low density, velocity, and in turn momentum of the air-flow, results in a significant degradation in atomisation quality at restart conditions (Beck et al. 1991). Indeed Caines et al. (2001) have observed droplets as large as 300  $\mu\text{m}$  in diameter at sub-atmospheric operating points.

The formation of fine droplets may be further hampered by low fuel temperatures. The temperature of fuel in the aircraft storage tanks decreases during flight to a minimum of around  $-35\text{ }^\circ\text{C}$  (Nicholas 2005), and for this reason the freezing point of Jet A kerosene must not exceed  $-45\text{ }^\circ\text{C}$  (ASTM 2008). During cruise operation the fuel is heated as it passes through the injector feed arm. Since the engine cools rapidly following flame-out, this warming does not occur and the viscosity of the fuel increases appreciably as a result (Coordinating Research Council 2004; Atkins et al. 2005), further impeding atomisation (Lefebvre 1989).

Ballal and Lefebvre (1979) have shown that the minimum energy required to ignite a flowing heterogeneous mixture varies with the fourth power of mean droplet diameter (see Section 2.4.3). This relationship results from the slower evaporation of larger droplets by virtue of their smaller surface area to volume ratio. Furthermore, Richards and Lefebvre (1989) have demonstrated that for droplet diameters greater than 40  $\mu\text{m}$ , the speed of an ambient kerosene-air flame is inversely proportional to the Sauter mean diameter (SMD - the diameter of a drop with a surface area to volume ratio equal to that of the spray as a whole). This supports independent observations that the combustion efficiency is also adversely affected by increasing droplet size (Lefebvre 1999).

Following injection, the evaporation of fuel is further limited by the low gas and liquid-phase temperatures. As described above, the liquid fuel temperature is likely to be low, with a correspondingly low vapour pressure. Prior to restart, the greater mass of fuel is therefore likely to be contained in liquid droplets that are considerably larger than those produced at any other engine operating point. Fuel-air mixing is thus comparatively poor. The inertia of these large liquid droplets often causes them to deviate significantly from the streamline of the surrounding air. Coupled with low evaporation rates, this results in significant impingement of liquid fuel on the internal surfaces of the combustor.

In principle, the quantity of fuel injected into a LDI combustion chamber can be modified to provide the optimum AFR for successful restart. In practice however the temperature rise inside the combustion chamber must be limited to avoid compressor surge and high-temperature damage to the turbine, and the global AFR is consequently set leaner than stoichiometric. However, large fluctuations and point-to-point differences in equivalence ratio undoubtedly exist due to high rms turbulence levels and significant spatial and temporal variations in gas velocity and droplet size.

The ignition, stabilisation, and efficiency of kerosene-air flames generated under

altitude conditions are all adversely affected by the comparatively low air temperature and pressure inside the combustion chamber. To achieve ignition, the temperature of the reactants must be raised to a point where the thermal energy release is sufficient to sustain a chemical reaction. Ignition of low-temperature reactants therefore requires more energy than at ambient conditions. The temperature of the reacting gases is also reduced by the cold fuel and excess air. The rate of most chemical reactions varies with temperature according to the Arrhenius relationship

$$k = A \exp\left(-\frac{E_A}{RT}\right), \quad (2.8)$$

where  $A$  is known as the pre-exponential factor,  $E_A$  is the activation energy, and  $R$  is the universal gas constant (Glassman 1996). The reaction rate decreases exponentially with reductions in temperature.

The rate of chemical reaction is also adversely affected by reductions in pressure; at low pressures the reaction rate is approximately proportional to the square of pressure (Kerrebrock 1977). These temperature and pressure dependencies result in a dramatically reduced reaction rate under restart conditions. This extended reaction time limits combustion efficiency and reduces the stability limits of the flame (Hill and Peterson 1992).

### 2.2.2 The restart process

Lefebvre (1999) has proposed that the in-flight engine restart process can be separated into three phases:

1. a spark discharge giving rise to the formation of a flame kernel containing sufficient heat to propagate successfully;
2. migration of this kernel to the fuel injector face and stabilisation of the flame at a single fuel injector;
3. flame spread around the combustor annulus to all fuel injectors (known as ‘light-round’).

To this list one final phase might be added:

4. the generation of sufficient heat release to accelerate the gas turbine to its operational speed (known as ‘pull-away’).

Pull-away generally requires a combustion efficiency exceeding 80% (Lefebvre 1999). All four phases must be successful in order to restart the engine. In the current study, phases 1 and 2 of the engine restart process are considered, and these will be collectively referred to as relight from now on.

Though ignition of a combustible mixture may be accomplished using a variety of methods, a spark discharge is a simple and effective means of generating the large temperature increase necessary to create a viable flame kernel. For this reason spark ignition has been universally adopted in aviation gas turbine applications. A modern ignition system consists of an exciter unit connected to a surface-discharge igniter via a lead. Typically two of these systems are installed in each engine. A reservoir capacitor inside the voltage generator unit is charged by means of a transistor, and discharges through the igniter when the breakdown voltage is exceeded.

The two igniters are mounted radially on opposite sides of the combustor annulus. In a conventional combustion system, the tip of each igniter is generally situated at the upstream edge of the primary zone, flush with the external surface of the flame tube. The igniter tip is usually located further downstream in a LDI combustor, above the central recirculation zone. The surface-discharge igniter used in aircraft engines consists of two concentric electrodes separated by a ceramic insulator. The outer electrode is grounded, and the open end of the insulator is coated with a thin layer of silicon carbide. This semiconducting layer promotes ionisation between the electrodes, allowing the generation of sparks at comparatively low voltages ( $\approx 2$  kV). When the breakdown voltage is exceeded, the current that begins to flow through the semiconductor is concentrated into a fine filament. Having created an ionisation path between the electrodes, the main discharge follows as a powerful arc. This process is unaffected by the pressure of the surrounding air.

For large turbofan engines the stored energy is normally between 4 and 12 J with a typical sparking rate of 1 Hz. Lefebvre (1999) has reported that only a quarter of the energy discharged from the capacitor reaches the igniter tip. Furthermore, only a third of this energy directly heats the fuel-air mixture, the remainder being either conducted to the igniter face or dissipated as light and sound. Large quantities of fuel deposited on the igniter tip can further reduce the spark energy (Odgers and Coban 1977), in addition to significantly shortening the igniter operating life (Burland et al. 1984). As detailed in Section 2.4 below, previous studies have demonstrated that spark ignition of a droplet mixture is influenced by various attributes of the spark discharge. Ignition probability has, for example, been shown to increase with spark size, energy, duration and frequency. While these effects have been quantified in well-characterised mixtures, their significance during gas turbine restart has received little attention.

### 2.2.3 Design for altitude restart

As discussed above in Section 2.2.1, the fuel preparation, mixing, ignition and heat release processes that are necessary for successful restart are all slowed by the low air temperatures and pressures inside the combustion chamber following flame-out. The residence time of the reactants inside the combustor must therefore be comparatively long to ensure that the heat released is sufficient to create and sustain a flame. For this reason, the overall combustion chamber volume is determined by the restart requirement (Nicholas 2005). However, an unnecessarily large combustor volume must be avoided, both to limit the time available for  $\text{NO}_x$  formation at high power, and to minimise the size and weight of the combustion subsystem. From an engine design perspective, it is therefore necessary to develop a good understanding of the combustor volume required to ensure ignition, flame stabilisation and the required combustion efficiency.

At present, the combustion chamber volume is determined using a set of empirical

correlations developed during the design of conventional combustion systems. These design rules are proving inappropriate for the development of future-generation LDI combustors, as the combustor aerodynamics and fuel placement generated by these systems are radically different from those produced by conventional designs. In addition, the use of computational modelling as a design tool is severely limited by the complex turbulence-chemistry interactions that occur in gas turbine flames (Cant and Mastorakos 2008).

The lack of design data for LDI combustion systems coupled with the limited modelling capability described above has led to increased use of ground-based altitude testing to determine restart performance. Altitude test facilities have been constructed that can simulate the conditions inside the combustion chamber following flame-out. These facilities provide a flexible means of evaluating and developing combustor designs. Though costly in comparison to computational modelling work, ground-based testing is significantly less expensive than flight testing on board an aircraft.

The objective of ground-based relight testing of the kind conducted using the Rolls-Royce ATF (see Section 3.1), is to identify those combinations of air temperature, pressure, mass flow rate, and fuel-air ratio (FAR) that allow ignition and flame stabilisation at a single fuel injector. While maintaining a constant temperature, pressure and mass flow rate, relight is attempted across a range of FAR. A relight attempt is regarded as successful if ignition occurs within a predefined period of the first spark, and the flame sustains itself for a further interval following termination of the spark (both periods are typically 10 s). The procedure is repeated for a range of air mass flow rates.

As illustrated schematically in Figure 2.4, these results are presented in the form of an ignition loop. This loop separates regions of successful and unsuccessful relight at a given temperature and pressure. Relight is successful inside the area enclosed by the loop, and the point identified as ‘safe’ is therefore conducive to ignition. Above

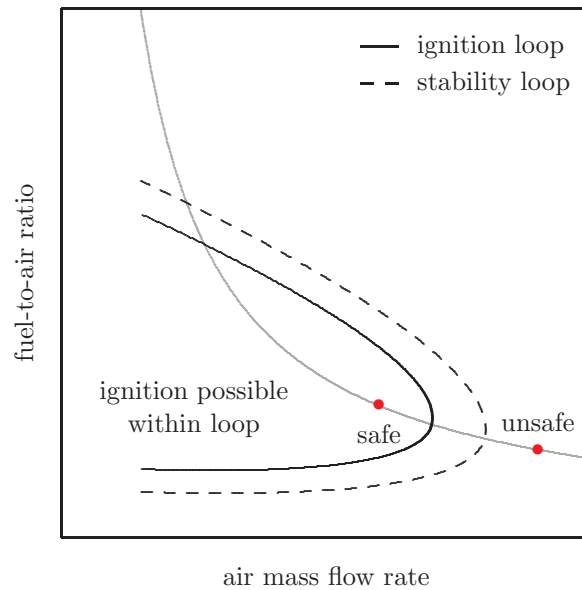


Fig. 2.4: Ignition and stability loops. A line of constant fuel flow rate is shown in grey.

and below this region the mixture is too rich and too lean respectively to ignite. As the air mass flow rate increases, the relight limits narrow until the flame can no longer stabilise. Ignition cannot therefore occur at the point marked 'unsafe'. In general, several ignition loops obtained at different temperatures and pressures are sufficient to determine the relight behaviour of the engine. Given knowledge of the maximum permissible fuel flow rate at restart, it is then possible to estimate the aircraft relight envelope as a function of flight altitude and speed.

Similar loops can be plotted to represent the stability limits of established flame. Following successful ignition at a given operating point, the fuel flow rate is reduced until flame extinction occurs. After recording the FAR at this lean blowout point, combustion is again established, and the fuel flow rate incrementally increased until rich extinction occurs. As before, this process is repeated at a variety of air mass flow rates. Since ignition and flame stability are influenced by similar factors, we may expect the two loops to coincide. As Lefebvre (1999) has noted however, the ignition

kernel has a comparatively large surface area to volume ratio and is surrounded by cold air, while a stabilised flame is larger and is bounded by the hot combustion chamber. The higher heat losses during ignition therefore make the developing flame kernel more susceptible to extinction, and for this reason the ignition loop always lies inside the stability loop. The relative position of these loops indicates to the combustor designer the measures required to improve relight performance. For instance, if the ignition loop lies well within the stability loop then relight performance may be improved by increasing the spark energy. On the other hand, if the ignition and stability loops are closely spaced and there still exists a relight problem, then wider measures are required to encourage flame stabilisation, such as changes to the combustor aerodynamics to ensure appropriate transport of the developing kernel.

Though constructed primarily for development testing, ground-based altitude facilities also provide a means of more closely exploring the physical and chemical processes occurring during restart. For example, optical access to these facilities allows the use of advanced non-intrusive laser techniques to understand flow structure, fuel placement, and flame development. From a design perspective, identifying the role and significance of the spark in the relight process may also lead to beneficial design changes. For example, the spark energy provided by the igniter exceeds the minimum ignition energies recorded under similar operating conditions (Ballal and Lefebvre 1978b; Ballal and Lefebvre 1979), suggesting that ignition success or failure is determined during the later stages of flame development. If the spark energy requirement could be reduced by more favourable spark placement in the flow field, then it may be possible to minimise the igniter hardware bulk and extend igniter life.

## 2.3 Review of ignition and flame stabilisation

Ignition is defined as the initiation of a self-sustaining exothermic reaction in an inflammable mixture. This is typically achieved by mixing the fuel and oxidant in appropriate proportions, and raising the temperature of the mixture to generate chemical radicals that react to initiate a flame. The initial temperature increase may be generated by a global heating process such as that occurring during the compression stroke in a diesel engine, or by a localised deposition of energy such as that produced by an electric spark. A spark generates an ignition kernel; a confined region of high chemical reactivity and heat release. The probability of this kernel evolving successfully into a self-propagating flame is governed by features of the spark coupled with parameters describing the state of the local mixture. The influence of these parameters is assessed by determining, either experimentally or theoretically, the heat addition required to generate a self-sustaining flame. This quantity of heat is referred to as the minimum ignition energy.

The ability of a spark to provide a rapid, highly-localised deposition of energy to a flowing fuel-air mixture has led to the universal adoption of surface-discharge igniters on aviation gas turbines. Numerous studies have been conducted examining the ground-level and high-altitude ignition performance of specific combustion system configurations (Xiong et al. 1981; Naegeli and Dodge 1991; Pucher and Allan 2004). However, as noted by Rao and Lefebvre (1976) the heterogeneous flow through a gas turbine combustion chamber is highly complex, producing marked fluctuations in the equivalence ratio, flow velocity, and turbulence properties below the igniter tip. Understanding derived from these investigations, while contributing to the development of a particular combustor, fails to provide generic information concerning ignition energy requirements. To achieve a sounder understanding of the underlying mechanisms governing flame development, it is necessary to evaluate the minimum ignition energy under well controlled conditions.

### 2.3.1 Paradigms of ignition research

Glassman (1996) notes that the theory of thermal ignition is based on a simple concept: an explosive condition exists if the rate of thermal energy release within a system exceeds the rate of thermal energy transfer from the system. The generation of a radially-propagating combustion wave following a spark discharge has thus been viewed as a process regulated by the competition between chemical energy release within the flame kernel and heat loss across the wave boundary. Deflagration models developed to characterise the nature of this thermal balance share several conceptual principles which are outlined below.

The spark discharge generates a small volume of high temperature gas. It has been suggested that in order to propagate through the mixture, the inflamed kernel must attain a minimum size before the internal temperature falls below the normal flame temperature. At this critical diameter, the surface area to volume ratio of the kernel is just small enough to ensure growth. The minimum ignition energy is defined as the quantity of energy required to heat the contents of this critical sphere to the mixture flame temperature. As such, the critical diameter and minimum ignition energy are closely related. If the supplied spark energy is less than the minimum ignition energy, the flame fails to become established as the mixture is quenched by the surrounding ambient gas and the electrodes.

During experimental ignition studies, heat transfer from the flame kernel to the electrodes causes an increase in the recorded minimum ignition energy when the electrode separation is less than a minimum value known as the quenching distance. Though the critical diameter and quenching distance have been viewed by some authors as directly equivalent (Lewis and von Elbe 1961), their distinct definitions should be noted.

Treating the spark discharge as a point source of heat, Glassman (1996) recommends the use of Zeldovich's thermal model for spark ignition. This theory proposes that for a quiescent premixed system, flame propagation will proceed provided that

the characteristic cooling time exceeds the combustion reaction time. The time-dependent temperature distribution generated by a point source of heat can be calculated from the heat diffusion energy equation. Expressed in spherical polar coordinates this is

$$\frac{\partial T}{\partial t} = \frac{\alpha}{r^2} \frac{\partial}{\partial r} \left( r^2 \frac{\partial T}{\partial r} \right), \quad (2.9)$$

where  $T$  is the mixture temperature,  $\alpha$  is the thermal diffusivity of the mixture ( $\alpha \equiv k/\rho c_p$ ), and  $r$  is the radial distance from the energy deposition point. The boundary conditions are

$$T \rightarrow T_0 \text{ as } r \rightarrow \infty \quad \text{and} \quad \frac{\partial T}{\partial r} = 0 \text{ at } r = 0. \quad (2.10)$$

The solution satisfying these boundary conditions has the form

$$T = T_0 + A(t) \exp(-r^2/4\alpha t). \quad (2.11)$$

Energy is conserved, and thus

$$E = 4\pi\rho c_p \int_0^\infty (T - T_0) r^2 dr, \quad (2.12)$$

where  $E$  is the deposited heat,  $\rho$  is the mixture density, and  $c_p$  is the specific heat at constant pressure of the mixture. Substituting Eq. (2.11) into the integral and integrating by parts, we find

$$\begin{aligned} \int_0^\infty (T - T_0) r^2 dr &= A(t) \int_0^\infty r^2 \exp(-r^2/4\alpha t) dr \\ &= 2\alpha t A(t) \int_0^\infty \exp(-r^2/4\alpha t) dr \\ &= 2\pi^{1/2} (\alpha t)^{3/2} A(t). \end{aligned} \quad (2.13)$$

Combining Eqs. (2.12) and (2.13) gives

$$A(t) = \frac{E}{\rho c_p (4\pi\alpha t)^{3/2}}, \quad (2.14)$$

and so the solution to Eq. (2.9) is

$$T = T_0 + \left[ \frac{E}{\rho c_p (4\pi\alpha t)^{3/2}} \right] \exp\left(\frac{-r^2}{4\alpha t}\right). \quad (2.15)$$

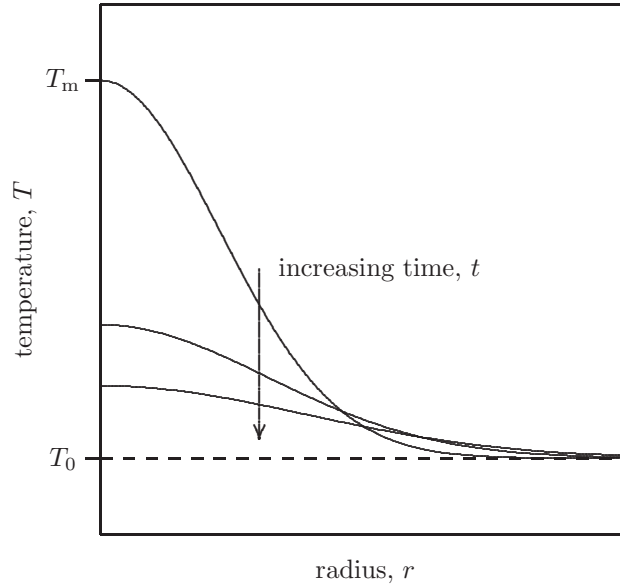


Fig. 2.5: Temperature profiles after point energy deposition (see Eq. (2.15)).

The spatial and temporal form of this solution is illustrated in Figure 2.5.

The maximum temperature,  $T_m$ , occurs at  $r = 0$  and is therefore

$$T_m = T_0 + \frac{E}{\rho c_p (4\pi\alpha t)^{3/2}}. \quad (2.16)$$

The characteristic cooling time,  $\tau_c$ , is defined as the period required for the temperature at  $r = 0$  to decrease by a small value

$$\theta = \frac{RT_m^2}{E}, \quad (2.17)$$

where  $R$  is the universal gas constant. The cooling time is thus approximated by

$$\tau_c = \frac{\theta}{(dT_m/dt)_{T_m=T_f}}. \quad (2.18)$$

The rate of change of temperature is evaluated when the temperature at  $r = 0$  is close to the adiabatic flame temperature of the mixture,  $T_f$ . Differentiating Eq. (2.16) with respect to time and substituting into Eq. (2.18) gives

$$\tau_c = \frac{\theta}{6\pi\alpha (T_f - T_0)} \left[ \frac{E}{\rho c_p (T_f - T_0)} \right]^{2/3}. \quad (2.19)$$

Supposing that the input energy  $E$  is equal to the energy required to heat a spherical volume of gas with diameter  $d_{\text{cr}}$  from temperature  $T_0$  to temperature  $T_f$ , then

$$E = \frac{\pi}{6} d_{\text{cr}}^3 \rho c_p (T_f - T_0). \quad (2.20)$$

Substituting Eq. (2.20) into Eq. (2.19)

$$\tau_c = 0.034 \frac{\theta}{(T_f - T_0)} \left( \frac{d_{\text{cr}}^2}{\alpha} \right). \quad (2.21)$$

The thermal flame theory proposed by Semenov and Frank-Kamenetskii provides the approximate reaction duration time associated with the combustion zone of a laminar flame

$$\tau_r \approx 2 \frac{\theta}{(T_f - T_0)} \left( \frac{\alpha}{S_L^2} \right), \quad (2.22)$$

where  $S_L$  is the laminar flame speed. The thermal flame thickness is

$$\delta = \frac{\alpha}{S_L}. \quad (2.23)$$

Combining Eqs. (2.21), (2.22), and (2.23), and applying the condition that  $\tau_c \geq \tau_r$  gives the condition for ignition as

$$d_{\text{cr}} \geq 7.6\delta. \quad (2.24)$$

This implies that the critical diameter must exceed the thermal flame thickness by a factor of approximately 8 for successful ignition to occur. Experimental confirmation of this relationship has proved challenging due to difficulties in determining the exact heat input generated by an air-gap spark. Despite this, experimental results suggest that for ignition to occur the critical diameter must be at least 6 times the flame thickness (Blanc et al. 1949).

Substituting Eqs. (2.23) and (2.24) into Eq. (2.20), and using the ideal gas law to re-express density in terms of temperature and pressure, gives a relationship between the minimum ignition energy,  $E_{\text{min}}$ , the far-field temperature,  $T_0$ , and the mixture pressure,  $P$

$$E_{\text{min}} \propto \left( \frac{k}{S_L} \right)^3 \left( \frac{T_0}{P c_p} \right)^2 (T_f - T_0). \quad (2.25)$$

Though temperature and pressure are clearly influential, the highest order dependences are associated with the thermal conductivity of the mixture and the laminar flame speed. Mixtures with a low thermal diffusivity that generate high flame speeds require less ignition energy by virtue of their thin thermal flame fronts.

Following an extensive series of experimental measurements, Lewis and von Elbe (1961) presented an alternative description of gaseous spark ignition in terms of adiabatic combustion wave theory. These authors proposed that kernel propagation occurs provided that the temperature gradient between the reactants and the combustion products is similar to that generated in the steady-state wave. They argue that exceptionally steep temperature gradients lead to a fast reduction in temperature throughout the combustion volume, with the ambient unburned gas quenching the flame. The quenching phenomenon is attributed to flame stretch.

To investigate this hypothesis the authors estimated the fractional increase in flame area when a combustion wave propagates a distance equal to the thermal flame thickness. Assuming that the ratio of the critical diameter to flame thickness is large i.e.  $d_{cr} \gg \delta$ , the critical stretch factor is

$$K = 4 \frac{\delta}{d_{cr}} \frac{\rho_u}{\rho_b}, \quad (2.26)$$

where  $\delta$  is the thermal flame thickness (see Eq. (2.23)),  $d_{cr}$  is the critical diameter of the flame sphere,  $\rho_u$  is the density of the unburned mixture, and  $\rho_b$  is the density of the burned products. By identifying  $d_{cr}$  as the experimental quenching distance, the data reported by Blanc et al. (1949) were used to calculate the critical stretch factor for a wide range of fuel-oxidant mixtures.

Stretch factors of between 0.5 and 1 were consistently reported, implying a degree of correlation between the measured quenching distances and the burning velocities, densities, and specific heats of the explosive gases. This finding is consistent with the Zeldovich analysis described above since the critical stretch factor, and thus the ratio of flame thickness to critical diameter, must be less than a threshold value to ensure flame propagation.

Lewis and von Elbe (1961) also evaluated the relationship between measured values of the minimum ignition energy, and two reference energy parameters, denoted  $E'$  and  $E''$ . The increase in sensible heat contained in the minimum flame sphere following a complete conversion of reactants to combustion products is

$$E' = \frac{\pi}{6} d_{\text{cr}}^3 \rho_b c_p (T_b - T_u), \quad (2.27)$$

where  $T_b$  and  $T_u$  are the temperatures of the burned and unburned gas mixtures respectively. Assuming that  $c_p$  does not vary significantly with temperature, and that the variation in density with temperature is given by  $\rho T = \rho_b T_b$ , then the sensible heat contained in the minimum flame can be approximated by

$$\begin{aligned} \int_0^{d_{\text{cr}}/2} 4\pi \rho c_p (T - T_u) r^2 dr &\approx 4\pi \rho_b c_p \int_0^{d_{\text{cr}}/2} \frac{T_b}{T} (T - T_u) r^2 dr \\ &< 4\pi \rho_b c_p \int_0^{d_{\text{cr}}/2} (T_b - T_u) r^2 dr \\ &= \frac{\pi}{6} d_{\text{cr}}^3 \rho_b c_p (T_b - T_u) \\ &= E' \quad (\text{by Eq. (2.27)}). \end{aligned} \quad (2.28)$$

Although  $E'$  is thus an overestimate of the sensible heat contained in the minimum flame sphere, it is within an order of magnitude of the true value. Considering the energy balance in a plane combustion wave, the total heat per unit area that is conducted through the flame thickness from hotter to cooler layers is approximately given by  $k(T_b - T_u)/S_L$ . Treating the minimum flame as planar, the total conducted heat stored within the kernel is thus

$$E'' = \pi d_{\text{cr}}^2 \frac{k}{S_L} (T_b - T_u). \quad (2.29)$$

The difference between the volume integrals of sensible and conducted heat inside the minimum flame kernel,  $(E' - E'')$ , represents the heat released by chemical reaction. Despite an order of magnitude correspondence, the measured values of  $E_{\text{min}}$  are generally less than both  $E'$  and  $E''$ , indicating that the heat in the minimum flame derives partly from the ignition source and partly from early chemical heat release.

The authors also suggested that all combustion waves possess excess enthalpy that maintains the correct temperature profile to ensure a balance between heat flow into the preheat zone and heat release in the reaction zone. A spherically propagating combustion wave thus requires a continuous source of excess enthalpy from an external source in proportion to the surface area of the flame front. To enable the flame to grow to a viable size, the ignition source must supply a minimum ignition energy equal to the excess enthalpy requirement of the minimum flame sphere. Though this hypothesis remains unproven, the authors maintain that it is consistent with the observation that measured values of  $E_{\min}$  are generally smaller than the corresponding approximate values of the conducted heat,  $E''$ .

A characteristic time approach has been developed by Peters and Mellor (1980) to examine the more complex phenomenon of spray ignition. This theory assumes that mixing and chemical reaction occur infinitely fast, and that the rate of heat release in the developing kernel is limited by the fuel evaporation rate. Having formulated order of magnitude expressions for quenching and evaporation timescales, these authors proposed that the kernel cooling period must exceed the total fuel evaporation time if successful flame propagation is to occur.

Assuming that heat is removed from the developing flame kernel by conduction, the cooling time is

$$\tau_c = \frac{\pi d^2}{\alpha}, \quad (2.30)$$

where  $d$  is the diameter of the kernel. In the absence of fuel vapour, the evaporation time of a monodisperse spray is defined as the ratio of the fuel mass contained in the kernel to the fuel evaporation rate

$$\tau_e = \frac{\rho_f c_p D^2}{8k_a \ln(1+B)}, \quad (2.31)$$

where  $\rho_f$  is the liquid fuel density,  $c_p$  is the specific heat capacity at constant pressure of the air,  $D$  is the drop size,  $k_a$  is the thermal conductivity of air, and  $B$  is the fuel transfer number (physically, the ratio of the energy available for evaporation to the energy required).

Identifying  $d$  as the quenching distance, and using the experimental data of Ballal and Lefebvre (1978a), a linear relationship was observed between the evaporation time and the kernel cooling time for a wide range of fuel transfer numbers, equivalence ratios, and droplet diameters. Based on this finding, the critical diameter could be identified for a defined set of system parameters. Having identified this diameter, the minimum ignition energy was calculated according to Eq. (2.20).

The values of minimum ignition energy derived from this model showed reasonable agreement with experimental results. Discrepancies were however noted in cases where the test conditions produced rates of chemical reaction and fuel evaporation that were comparable. This occurs in lean, low pressure sprays containing small, highly volatile fuel droplets. This deficiency, together with the possibility of fuel vapourisation prior to the spark, led Ballal and Lefebvre (1981) to devise a general model of fuel-air ignition that applies to both quiescent and flowing mixtures of air with any combination of gaseous or liquid fuel.

In addition to the cooling and evaporation times identified by Peters and Mellor (1980), a chemical reaction timescale,  $\tau_r$  was included. Thus for a flame kernel with the critical diameter,

$$\tau_c = \tau_e + \tau_r . \quad (2.32)$$

For a gaseous fuel this simplifies to

$$\tau_c = \tau_r . \quad (2.33)$$

If the right-hand side of Eqs. (2.32) or (2.33) is less than the cooling time then successful flame propagation will occur. Conversely, if they are greater than the cooling time then the ignition attempt will be unsuccessful. The general expression for the cooling time is

$$\tau_c \propto \frac{d^2}{\alpha + Au'd} , \quad (2.34)$$

where  $A$  is a constant and  $u'$  is the rms value of fluctuating velocity. The fuel

evaporation time is given by

$$\tau_e \propto \frac{(1 - \Omega) \rho_f c_p D^2}{k_a \phi \ln(1 + B) \left(1 + C \text{Re}_D^{1/2}\right)}, \quad (2.35)$$

where  $\Omega$  is the prevapourised fraction of the fuel,  $\phi$  is the equivalence ratio,  $C$  is a constant, and  $\text{Re}_D$  is the Reynolds number based on the droplet diameter and the rms value of fluctuating air velocity. The chemical reaction times in quiescent, low-turbulence, and high-turbulence conditions respectively are

$$\tau_r \propto \frac{\alpha}{S_L^2}, \quad \tau_r \propto \frac{\alpha}{(S_L - Eu')^2}, \quad \text{and} \quad \tau_r \propto \frac{\alpha}{u' (S_T - Fu')}, \quad (2.36)$$

where  $E$  and  $F$  are constants and  $S_T$  is the turbulent flame speed.

Each characteristic time is influenced by the flow Reynolds number. The evaporation time decreases with Reynolds number, while induced turbulence reduces both the cooling and reaction timescales. Again assuming the critical diameter and the quenching distance to be identical, the critical diameter and minimum ignition energy were calculated using Eqs. (2.20), (2.32), and (2.33).

Theoretical predictions produced by this model correlated well with experimental data for a wide range of fuel, flow and droplet parameters. As expected, chemical kinetic effects proved increasingly important with reductions in equivalence ratio and pressure. Inclusion of the chemical reaction time for these conditions produced a marked improvement in correspondence between theory and experiment. Using a virtually identical approach to analyse ignition of an n-decane spray, Dietrich et al. (1990) demonstrated good agreement with experimental results by using a chemical reaction timescale based on the Arrhenius reaction rate law.

In recent years the theoretical and empirical approaches to ignition research outlined above have been complemented by computational fluid dynamics (CFD) approaches that solve the fundamental transport equations for mass, momentum, and energy. Advances in numerical methods and parallel computing have enabled the application of direct numerical simulation (DNS) to the ignition of turbulent gaseous mixtures under conditions of both homogeneous (Klein et al. 2006) and

heterogeneous (Chakraborty et al. 2007) fuel distribution. Some agreement between DNS results and experimental data has also been demonstrated. For example, a study undertaken by Kaminski et al. (2000) of a turbulent premixed methane-air spark kernel showed reasonable agreement between the OH mole fraction predicted by DNS and that measured by high-speed PLIF. However, the comparison of DNS with experiments, or the use of DNS in place of experiments to validate theoretical ignition models is restricted by the computational difficulty of simulating realistic Reynolds numbers and complex chemical reactions.

Ignition modelling in practical combustion devices has been demonstrated by Boileau et al. (2008a, 2008b), who performed large-eddy simulations (LES) of ignition and light-round in a helicopter gas turbine. Flagship simulations such as these point to the future use of LES and DNS as design tools for improving the restart performance of gas turbines. However, the massive computational effort involved (700 parallel processors in the case of Boileau et al. (2008b)), currently limits their applicability in general. Ignition and flame development in a real gas turbine is a highly stochastic process, sensitive to initial conditions. To identify a representative range of ignition behaviour inside a gas turbine combustion chamber would therefore require many simulations; an approach that is prohibitively expensive at present. This difficulty is not encountered in experiments where a large sample of results can be obtained relatively easily. Experiments investigating ignition are reviewed in the next section.

## 2.4 Fundamental experiments to study ignition

As Warnatz et al. (2006) have highlighted, experimental research into spark-induced ignition is hampered by the necessary proximity of the spark electrode to the developing flame kernel, raising questions concerning surface chemistry and conductive heat losses. Revealing the relative proportions of spark energy responsible for local temperature increases and independent radical generation is similarly fraught with

difficulty. Despite these obstacles, numerous experimental studies have been undertaken to identify how the spark energy required to ignite a fuel-oxidant mixture is influenced by a variety of system parameters. These investigations have provided quantitative assessments of the independent effects on ignition performance of variations in the spark gap and timing, reactant temperature and pressure, mixture chemical composition and fuel phase, as well as flow velocity and turbulence characteristics. Lengthy description of the system parameters for each of the reviewed studies has been avoided by providing details of individual experimental configurations in tabular format. Tables 2.1, 2.2, and 2.3 provide information relating to ignition studies of gaseous blends, quiescent droplet suspensions, and flowing heterogeneous mixtures respectively.

It has been widely reported that, other things being equal, the measured minimum ignition energy varies markedly with both electrode separation distance and discharge duration. Endeavouring to report the true minimum energy requirement, the majority of the highlighted studies included optimisation procedures for both spark duration and gap width. This practice was not universally adopted however, with some researchers electing to maintain constant electrode separation and spark duration throughout the experimental data collection.

### 2.4.1 Ignition of gaseous blends

Blanc et al. (1947, 1949) developed apparatus to investigate the spark ignition of homogeneous combustible gas mixtures. Two glass-flanged electrodes were mounted near the centre of a spherical test bomb. Accurate adjustment of the spark gap was provided by a micrometer. Several fixed and variable capacitors and a static voltmeter were connected in parallel to provide a reservoir of known voltage. Initially, a rotary charger was used to transfer charge from a high voltage source to the electrode capacitor system, but this was later replaced by a paper rod impregnated with Bakelite. Fine adjustment of the system capacitance was achieved using numerous

Table 2.1: Experiments investigating ignition of gaseous mixtures.

	Blanc et al. (1947, 1949)	Ballal and Lefebvre (1977a)	Ballal and Lefebvre (1977b)
working section	spherical bomb, 127 mm internal diameter	horizontal box chamber, 90 mm × 90 mm × 310 mm	horizontal box chamber, 90 mm × 90 mm × 310 mm
electrodes	glass-flanged, 1.6 mm diameter	unflanged, 2 mm diameter	unflanged, 2 mm diameter
fuel specification	numerous, mainly alkanes	propane and methane	propane and methane
oxidant ratio	$\frac{O_2}{O_2+N_2} = 0.21-1$ , $\frac{O_2}{O_2+x} = 0.21$ , where $x = \text{He, Ar, CO}_2$	$\frac{O_2}{O_2+N_2} = 0.21-1$ , $\frac{O_2}{O_2+x} = 0.21$ , where $x = \text{He, Ar, CO}_2$	$\frac{O_2}{O_2+N_2} = 0.21-1$ , $\frac{O_2}{O_2+x} = 0.21$ , where $x = \text{He, Ar, CO}_2$
mixture temperature	ambient	ambient	ambient
mixture pressure (bar)	0.2-1.0	0.08-0.50	0.08-0.35
mixture velocity (m/s)	–	0-30	0-15.3
turbulence intensity (%)	–	2.5-15	2.5-15
turbulence scale (mm)	–	$\leq 10$	$\leq 12$
quenching distance (mm)	0.2-20	1.5-40	4-30
spark duration ( $\mu\text{s}$ )	not reported	not reported	$\approx 60$ , optimised
$E_{\min}$ (mJ)	0.002-100	0.4-90	0.02-60

Table 2.2: Experiments investigating ignition of quiescent aerosols.

	Ballal and Lefebvre (1978a)	Singh et al. (1986)	Danis et al. (1988)	Dietrich et al. (1990)
working section	vertical box chamber, 90 mm × 90 mm × 310 mm	vertical nozzle, 10 mm diameter	vertical tube, 16 mm diameter	vertical tube, 16 mm diameter
electrodes	glass-flanged, 2 mm diameter	1 mm diameter	flattened cathode, 1 mm diameter	flattened cathode, 1 mm diameter
fuel specification	six liquid fuels	Tetralin	methanol and n-heptane	n-decane
equivalence ratio, $\phi$	0.4-0.9	0.7-1.2	0.44-1.8	0.75-2.2
prevapourised fraction, $\Omega$	neglected	neglected	0.35, 0.45	< 0.07
air temperature (K)	290	ambient	ambient	ambient
air pressure (bar)	0.2-1.0	ambient	ambient	ambient
flow details	air velocity $\approx$ 0.2 m/s	nozzle Re = 300	tube Re = 100-300	air flow rate = 0.27–0.45 m <sup>3</sup> /min
means of atomisation	spinning cup atomiser	controlled condensation	vibrating orifice aerosol generator	twin vibrating orifice aerosol generators
droplet size parameters	SMD = 30-180 $\mu$ m Rosin-Rammler ind. = 8-11	SMD = 6.7-40 $\mu$ m std. dev. = 6-13%	SMD = 30-57 $\mu$ m	bidisperse, with peaks at 30 $\mu$ m and 90 $\mu$ m
quenching distance (mm)	2-15	3-4	2-7	not determined
spark duration ( $\mu$ s)	60-100, optimised	40-130, optimised	30-100, optimised	60, constant
$E_{\min}$ (mJ)	0.1-1000	1-50	0.2-100	0.4-40

Table 2.3: Experiments investigating ignition of flowing droplet mixtures.

	Rao and Lefebvre (1976)	Ballal and Lefebvre (1978b)	Ballal and Lefebvre (1979)
working section	horizontal box chamber, 75 mm $\times$ 75 mm $\times$ 350 mm	horizontal box chamber, 75 mm $\times$ 75 mm $\times$ 350 mm	horizontal box chamber, 75 mm $\times$ 75 mm $\times$ 350 mm
electrodes	tapered tungsten, 1 mm diameter	tapered stainless steel, 2 mm diameter	tapered stainless steel, 2 mm diameter
fuel specification	aviation kerosene	aviation kerosene	six liquid fuels
equivalence ratio, $\phi$	0.35-1.05	0.3-0.9	0.4-1.9
prevapourised fraction, $\Omega$	neglected	0.15	neglected
air temperature (K)	ambient	228-350	290
air pressure (bar)	ambient	0.2-0.9	0.2-1.0
air velocity (m/s)	19.0-49.5	9-38	15-40
turbulence intensity (%)	not reported	not reported	2.5-15
means of atomisation	five simplex atomisers	simplex, acoustic, and spinning cup atomisers	twelve simplex atomisers
SMD ( $\mu\text{m}$ )	30-80	20-180	40-150
quenching distance (mm)	not determined	not reported	2-22
optimum spark duration ( $\mu\text{s}$ )	30-80	30-100	40-100
$E_{\text{min}}$ (mJ)	3-90	2-800	0.02-1000

detachable rod and ball capacitors mounted on the high-voltage terminal. Ignition tests were performed with mixtures of oxygen, nitrogen and a variety of hydrocarbon fuels, mainly alkanes. The results of hydrogen ignition tests were also published at a later date (Lewis and von Elbe 1961). By replacing the nitrogen component of air with individual inert gases, it was possible to assess the flame-quenching effects of helium, argon and carbon dioxide.

Following adjustment of the spark gap to the required distance, the bomb was filled with an explosive mixture of defined composition and pressure. The electrode system was slowly charged and the breakdown voltage,  $V$ , noted. Ignition was confirmed by visual observation of a flame. If flame propagation did not occur, then the capacitance,  $C$  was incrementally increased until a developing flame kernel was produced. The minimum ignition energy was then identified as the energy stored in the ignition circuit prior to the spark discharge given by

$$E_{\min} = \frac{1}{2}CV^2. \quad (2.37)$$

Typical plots of minimum ignition energy versus electrode separation indicated that for large electrode separations, increasing spark gap distances require greater ignition energies. For well separated electrodes, heat generation occurs throughout a comparatively large volume, and increasing energies are therefore required to produce the high-temperature, initial kernel necessary to ensure flame development. As the spark gap width is reduced below the quenching distance, an increasing proportion of the deposited energy is drained from the kernel by conductive heat transfer to the electrodes. With the flanged electrodes mounted, this produced a sharp rise in ignition energy requirements. Free electrode tips showed a more gradual increase in minimum ignition energy as the spark-gap width was reduced below the critical separation.

For mixture pressures exceeding 0.33 bar, the minimum ignition energy is constant for mid-range values of electrode separation. Though the cause of these energy plateaux remains unclear, they may represent a fundamental lower energy limit as-

sociated with chemical and physical properties of the system, independent of electrode quenching characteristics. If true, this implies that electrode quenching may result in overestimates of ignition energy for configurations producing no observable plateaux.

Minimum ignition energies corresponding to the lowest points on each energy-separation curve were recorded for a variety of gaseous mixtures and total pressures. The results are generally consistent with the trends observed by Calcote et al. (1952). Both the quenching distance and minimum ignition energy increase with reductions in pressure and oxygen concentration. Remarkably, the energy curve minima for a variety of fuel-air mixtures at atmospheric pressure consistently fell within a narrow range between 0.23 and 0.28 mJ. It was also noted that the minima shifted to fuel-rich mixtures as the number of carbon atoms in the fuel increased. These features reflect variations in mixture flame speed with equivalence ratio.

As is true for surface-discharge sparks, much of the electrical energy delivered between the electrodes of an air-gap spark does not produce heating of the combustible mixture, but is instead transferred away by radiation, shock wave formation, and conductive heat losses along the electrodes. Rose and Priede (1959) have demonstrated that parameters such as the spark-gap geometry, electrode material and discharge interval play a significant role in determining the magnitude of these losses.

Ballal and Lefebvre (1977a, 1977b) extended this research to examine the ignition behaviour of flowing, turbulent gaseous mixtures. The ignition test section was mounted in a closed-circuit wind tunnel, allowing sub-atmospheric circulation of the combustible mixtures at ambient temperature. Several interchangeable perforated plates mounted upstream of the working section generated near isotropic turbulence in the ignition zone. The fuels studied were methane and propane, with nitrogen in the air partially replaced by oxygen or totally replaced by various inert gases (CO<sub>2</sub>, He, Ar). A wide variation was thus achieved in the physical and chemical

properties known to affect quenching distance and minimum ignition energy, namely thermal conductivity, pressure, specific heat capacity, laminar flame speed and flame temperature (see Eq. (2.25)). Two high voltage probes recorded traces of electrode current and voltage as a function of time. The spark energy was then evaluated by integrating the product of these values over the spark duration.

The required mixture was circulated at the appropriate pressure and velocity and the spark energy was gradually increased until the onset of ignition, confirmed by the appearance of flame. The spark-gap width was incrementally adjusted to generate a plot of ignition energy versus electrode separation. The plateaux observed by Blanc et al. (1947) at the base of each curve was not evident for the low pressure data presented. The quenching distance was therefore defined as the electrode separation at the point of minimum ignition energy. The spark duration was also optimised at each test condition.

Initial experiments to confirm the ignition behaviour of quiescent propane mixtures at sub-atmospheric pressures showed quenching distances in good agreement with previous data. However, the minimum ignition energies reported were substantially lower than suggested by earlier data, possibly due to the authors' efforts to optimise spark duration. All other parameters being equal, larger flow velocities increased the minimum ignition energy requirements. This was attributed to increasing turbulence intensity rather than to the mean flow rate; though turbulence raises the burning velocity, the rate of heat loss from the developing spark kernel also increases, and it is this effect that dominates. In line with trends observed for quiescent gases, the minimum ignition energy of flowing mixtures was significantly reduced by relatively small increases in pressure and oxygen concentration. Furthermore, ignition energy minima coincided with points of maximum burning velocity for a range of fuel and oxygen mass fractions, suggesting that for flowing mixtures, transport processes are more significant than preferential diffusion effects.

In addition to laying foundations later incorporated into a general model of spark

ignition, this work provided two informative insights into the spark ignition process. Firstly, having derived a theoretical expression for the kernel critical diameter assuming a linear variation with flame thickness, empirical minimum ignition energy data were observed to vary with the cube of critical diameter. This relationship was demonstrated for a wide range of mixture composition and turbulence intensity. Secondly, contrary to the earlier assumption of Lewis and von Elbe (1961), Ballal and Lefebvre demonstrated that the kernel critical diameter and quenching distance are not equal, but proportional to each other. For the gaseous mixtures examined, the critical diameter corresponded to approximately 20% of the quenching distance.

### 2.4.2 Quiescent droplet suspensions

A central feature of heterogeneous ignition is that flame propagation may result from one, or a combination of several distinct physical mechanisms. Aggarwal (1998) has identified three ignition modes for two-phase fuel-air mixtures. Individual droplet ignition (mode 1) is characterised by the development of a diffusion flame surrounding, and of similar characteristic dimension to an isolated droplet. In contrast, spray ignition (mode 3) is associated with the propagation of a sheath flame, several orders of magnitude larger than any drop. The droplet cluster mechanism (mode 2) represents an intermediate regime, providing a link between the local droplet and global sheath ignition modes. While the dominant burning mechanism has important effects on pollutant formation (Rah et al. 1986), the variation in flame speed between these modes is highly significant when assessing ignition energy trends.

In a seminal paper, Burgoyne and Cohen (1954) examined the influence of droplet size on both flame propagation modes and rates in aerosol mixtures. A novel apparatus was developed to generate monodisperse suspensions of Tetralin (tetrahydronaphthalene) by controlled condensation. Following dilution of the aerosol with appropriate quantities of air, a conical inverted flame was established at the base of a cooled burner tube. The burning velocity was calculated for a range of drop sizes

by measuring the suspension flow rate and the flame geometry.

The authors observed a transition in the flame propagation process as the droplet size was increased from 7 to 55  $\mu\text{m}$ . For droplet diameters below 10  $\mu\text{m}$ , vaporisation and mixing of fuel with the surrounding air occurred prior to the reaction zone, producing a coherent blue flame front. As the droplet size increased beyond the full vaporisation limit, white combustion centres became evident, resulting from diffusion burning of individual droplets. Above 20  $\mu\text{m}$  there appeared insufficient preliminary vaporisation to sustain a coherent front, with the flame forming a brush-like spray of yellow centres, lacking visible interconnection.

In light of these observations the authors proposed that convection processes facilitate the particulate mode of propagation, generating a solid network of flame passing through the mixture, whilst leaving appreciable cells of relatively cool excess air. For droplet dimensions exceeding 30  $\mu\text{m}$ , experimental results indeed confirmed that the transmission of flame between droplets was possible over distances of up to 30 diameters. Experimental data also suggested that a significant increase in flame propagation speed with droplet diameter occurs during the transition from a fully-vaporised flame to combustion of isolated droplets. For instance, maintaining the same mass concentration of fuel, droplet enlargement from 9 to 30  $\mu\text{m}$  produced a two-fold increase in the burning velocity.

Polymeropoulos and Das (1975) have reported a similar trend for polydisperse kerosene-air mixtures. A peak in burning velocity was noted for a droplet size distribution centred at 30  $\mu\text{m}$ , with a decrease in propagation speed for larger drops. Richards and Lefebvre (1989) also noted an optimum droplet diameter while investigating flame development in monodisperse, rich, kerosene-air mixtures with droplet sizes of less than 110  $\mu\text{m}$ . At an overall equivalence ratio of 1.46, the authors reported a peak in burning velocity corresponding to a mixture droplet diameter of approximately 45  $\mu\text{m}$ .

To measure the effect of droplet size on minimum ignition energy, a fuel air mix-

ture must be generated containing droplets that are the same size, or monodisperse. Considerable experimental challenges have been overcome to create monodisperse aerosols containing droplets ranging from 10 to 200  $\mu\text{m}$  in diameter. The droplet size parameter most widely employed to characterise liquid sprays is the Sauter mean diameter. This dimension represents the diameter of a drop with a volume to surface area ratio equal to that of the whole spray. Thus

$$\text{SMD} = \frac{\sum_{i=1}^N D_i^3}{\sum_{i=1}^N D_i^2}, \quad (2.38)$$

where  $N$  is the total number of droplets and  $D_i$  is the diameter of an individual droplet. Though a range of mean diameters can be formulated by averaging droplet diameters, surface areas, and volumes, Lefebvre (1989) notes that the SMD alone offers a reliable indication of atomisation quality for combustion applications. Investigating the ignition behaviour of a bidisperse spray, Dietrich et al. (1990) have shown that for a polydisperse mixture the SMD is the only droplet size parameter that reflects the increase in ignition energy with droplet diameter expected for an evaporation-controlled process.

Clearly no mean dimension alone can uniquely represent the partition of mass in a fuel spray. However, a single additional parameter representing the drop size dispersion can often be combined with a representative diameter to describe the distribution more completely. The most widely employed expression for drop size distribution was devised by Rosin and Rammler (1933) and may be expressed as

$$Q = 1 - \exp \left[ - \left( \frac{-D}{X} \right)^q \right], \quad (2.39)$$

where  $Q$  is the fraction of the total fuel volume contained in droplets of diameter less than  $D$ ,  $X$  is the representative diameter, and  $q$  is the dispersion parameter. As the dispersion parameter increases, the distribution of droplet size becomes more uniform. This dispersion parameter lies between 1.5 and 4 for most atomisers, though values exceeding 11 have been achieved using some rotary designs.

Having demonstrated means of creating heterogeneous fuel-air mixtures containing droplets of well defined size and distribution, Ballal and Lefebvre (1978a) investigated the influence of equivalence ratio, pressure and droplet size on the minimum ignition energy of quasi-stationary fuel mists. Fuel volatility effects were also measured following earlier work highlighting the significance of fuel properties in determining ignition performance. Postulating that successful ignition occurs when the mass of fuel vapour generated by the spark exceeds a threshold value, the atomiser and spark electrodes were positioned in close proximity to create a fuel-air mixture containing minimal fuel vapour. The mixture velocity between these locations was minimised, subject to ensuring negligible fuel evaporation.

Though mounted vertically, the test section was virtually identical to that designed for earlier studies of homogeneous ignition (see Section 2.4.1). Glass flanges were mounted on the electrodes to minimise variations in the spark breakdown voltage due to fuel wetting. A spinning cup atomiser was located a small distance upstream of the test section, producing an essentially monodisperse, falling spray, while allowing independent control of fuel flow rate and droplet size. The mixture SMD was measured using a laser scattering technique described by Lorenzetto and Lefebvre (1977). The equivalence ratio was calculated from the total flow rates of air and fuel into the ignition zone. All mixtures tested were sub-stoichiometric, and the significance of evaporation processes during ignition was investigated by testing six fuels with different evaporation properties. Care was taken to ensure that values of minimum ignition energy were recorded following optimisation of both spark duration and electrode separation.

In accordance with earlier findings for homogeneous mixtures, quenching distance and minimum ignition energy were shown to increase with reductions in both pressure and equivalence ratio. The minimum ignition energy was also found depend strongly on droplet size, increasing with the cube of drop diameter. Predictably, greater energies were required to ignite mixtures containing fuels with a compara-

tively low volatility.

Adopting an approach similar to that advocated by Peters and Mellor (1980), the authors proposed a model for the ignition of quiescent droplet mists. They assumed that ignition success is governed solely by the fuel evaporation rate. This model agreed well with experimental results, strengthening the assertion that fuel evaporation is the rate-controlling step for a diverse range of conditions. This evaporative control was confirmed by supplementary experiments designed to produce wide variations in flame temperature, thereby revealing any kinetic dependence. For the heterogeneous mixtures examined, the critical diameter corresponded to approximately 80% of the quenching distance; significantly larger than the value of 20% reported for homogeneous mixtures.

Though offering pioneering insight into the ignition of fuel mists, the study of Ballal and Lefebvre (1978a) was limited to lean mixtures containing relatively large droplets. In addition, a single value of the minimum ignition energy was reported for each test condition. Several researchers have noted that ignition is an innately stochastic process. Consequently, at a specific test condition ignition is possible for a range of spark energies, albeit with different probabilities of success. Singh and Polymeropoulos (1986) have suggested that these probabilistic features result from differences in the shape and position of the spark discharge channel, coupled with spatial non-uniformities in the droplet distribution.

Working independently, Singh and Polymeropoulos (1986) and Danis et al. (1988) investigated the ignition behaviour of both lean and rich monodisperse mixtures. Though examining dissimilar fuels and using different means of atomisation, these studies shared several common features. Both researchers characterised droplet size by means of laser diffraction techniques. In addition, mixture equivalence ratio was regulated by the addition of oxygen or air to the droplet suspension. Ignition energies were evaluated at ambient conditions throughout, and standard spark discharge apparatus was used, allowing independent control of spark energy and

duration. Ignition energies were principally recorded following optimisation of both spark duration and electrode separation.

Singh and Polymeropoulos (1986) investigated the influence of oxygen concentration, equivalence ratio and droplet size on the spark energy required to ignite Tetralin aerosols. Utilising the technique developed by Burgoyne and Cohen (1954), droplet generation was achieved by controlled condensation of fuel vapour on sodium chloride nuclei. Metered oxygen and air flows were introduced, inhibiting droplet aggregation, whilst providing control of the overall equivalence ratio. Isokinetic sampling at the spark gap confirmed these values.

Maintaining constant oxygen concentration and drop size, increasing spark energy predictably produced a higher probability of ignition success. However, this improvement in performance approached an asymptotic limit that was often constrained to a comparatively low ignition probability. This was apparent for a  $6.7\ \mu\text{m}$  mixture, where the success rate never exceeded 20% for spark energies less than 50 mJ. It was also evident that the maximum ignition probability for a given spark energy occurred for a specific droplet diameter. The measurements indicated an optimum droplet size of between  $22\ \mu\text{m}$  and  $26\ \mu\text{m}$ . In line with the change in equivalence ratio, the increase in oxygen concentration produced improvements in ignition performance due to the accompanying increase in flame velocity.

A model was also developed to estimate the non-reactive fuel vapour concentration and droplet motion generated following a spark discharge. This analysis was based on earlier observations that rapid compression of a gaseous medium during the early stages of an electrical discharge generates two primary features: a high-speed shock wave and a constant-pressure hot gas kernel. Results suggested that the fuel vapour concentration generated at the kernel centre was close to stoichiometric for sprays containing droplets  $24\ \mu\text{m}$  in diameter. Larger drops produced a leaner mixture while the vapour equivalence ratio exceeded 3 for a droplet diameter of  $6.7\ \mu\text{m}$ . The model also indicated that smaller droplets are displaced radially by gas motion

produced by the expanding shock wave, creating a fuel lean annular region around the kernel. It was suggested that this fuel free region inhibits flame growth, resulting in low ignition frequencies for droplet diameters of less than 10  $\mu\text{m}$ .

Further evidence supporting the optimum droplet size hypothesis was provided by Danis et al. (1988). Varying both equivalence ratio and droplet size, this study compared ignition energy requirements for n-heptane and methanol sprays with those for similar prevapourised mixtures. A vibrating orifice aerosol generator was used to generate extremely uniform sprays, with the standard deviation in droplet diameter typically less than 1% of the mean value.

Ignition events again appeared highly stochastic. For example, a lean n-heptane spray containing 53  $\mu\text{m}$  droplets required an order of magnitude increase in spark energy to raise the ignition probability from 20% to 85%. The minimum ignition energy was arbitrarily defined as the spark energy corresponding to an ignition frequency of 50%. A plot of minimum ignition energy versus equivalence ratio for prevapourised n-heptane corresponded closely to that reported by Lewis and von Elbe (1961), suggesting an optimum equivalence ratio of between 1.5 and 2. An optimum droplet size of between 10 and 30  $\mu\text{m}$  was reported, and the lean ignition limit was extended by the presence of droplets. This phenomenon was also observed by Cohen et al. (1996) while examining Tetralin mixtures, and is believed to result from regions of favourable gas-phase stoichiometry that form locally around evaporating droplets.

### 2.4.3 Flowing heterogeneous mixtures

The minimum energy required to initiate a flame kernel in a gas turbine combustion chamber depends on the flow field adjacent to the igniter. Recognising this, Ballal and Lefebvre (1978b, 1979) extended the scope of their generic studies to assess ignition energy variations with local flow velocity and turbulence intensity. The influence of air pressure, droplet diameter and equivalence ratio on minimum ignition

energy was again examined for flowing two-phase mixtures, with air temperature effects also assessed.

The test facility remained largely unmodified throughout the experimental measurements, incorporating a test section virtually identical to that designed for earlier gaseous ignition studies (Ballal and Lefebvre 1977a). Fuel was admitted to the test section through an interchangeable assortment of simplex, acoustic and spinning cup atomisers mounted upstream of the test section. The principal fuel investigated was aviation kerosene, though five hydrocarbon fuels of differing volatility were also introduced during the later stages of the study. Droplet diameter was recorded for the full range of fuel and air flow rates using the light-scattering technique developed for quiescent aerosol measurements.

Prior to ignition testing, isokinetic sampling of the mixture in the spark gap allowed calculation of the equivalence ratio for a range of flow conditions. To reduce the risk of damage to the apparatus the prepared mixtures were all lean. Though initial testing was conducted at ambient conditions, an altitude test facility was later incorporated, generating air temperatures and pressures as low as 228 K and 0.2 bar respectively. Physical conditions at the electrodes thus reflected those encountered at altitudes in excess of 30000 ft (see Figure 2.3). A flow conditioner installed immediately upstream of the fuel injector was later replaced by a gauze grid, generating near isotropic turbulence in the ignition zone.

A preliminary investigation revealed those mixture parameters influencing spark discharge energy and optimum duration. Maintaining a fixed spark current, a considerable increase in discharge voltage and thus spark energy was observed for mixtures flowing at higher velocities. It was suggested that the associated increase in discharge pathway resistance, resulted from ‘stretching’ of the spark during the discharge period. This is plausible given that a 100  $\mu$ s spark is displaced through 5 mm in a mixture flowing at 50 m/s. Though unsubstantiated, the authors also proposed that this extension of the spark pathway reduced conductive heat losses

to the electrodes. It was incidentally noted that the breakdown voltage required for liquid fuel sprays was considerably higher than that necessary in gaseous mixtures. This was reportedly due to the inevitable deposition of liquid fuel at each electrode tip.

At the operating conditions considered, the optimum spark duration increased with droplet diameter and decreased with flow velocity. These results are arguably unsurprising given the finite time required for fuel evaporation together with the need to ensure highly localised heat deposition. With the exception of the earliest study, which was conducted with a fixed spark gap, values of minimum ignition energy were recorded following optimisation of both spark duration and electrode separation.

Results confirmed that higher equivalence ratios and fuel volatility promote successful ignition. The dependence of minimum ignition energy on droplet size was found to be stronger for heterogeneous flowing mixtures than for quiescent sprays:  $E_{\min} \propto D^{4.5}$  compared to  $E_{\min} \propto D^3$ . Furthermore, despite following consistent trends, the measured droplet size exponent appeared to increase as the studies progressed. Ballal (2004) later suggested several possible reasons for these inconsistencies. Early kerosene-air studies used an assortment of simplex, acoustic and spinning cup atomisers to generate the required range of droplet diameters. Later research, investigating the ignition behaviour of multiple fuels, employed 12 carefully matched simplex atomisers producing consistent drop size distributions and minimising liquid fuel deposition at the duct walls. Perhaps more critically, as research progressed, the authors recognised the need to maintain constant turbulence intensity while examining the influence of other variables. Only during the later studies could it be argued that independent control of equivalence ratio, fuel volatility, droplet size, flow velocity, pressure and turbulence intensity had been maintained.

In agreement with the behaviour reported for gaseous mixtures, the minimum ignition energy was found to increase with turbulence intensity, and, as before, the

influence of mean velocity on spark energy did not appear to extend beyond those effects resulting from this increased turbulence intensity. The detrimental impact of low air temperatures on ignition performance was also apparent. For a stoichiometric mixture the decrease in temperature associated with high-altitude flight required a three-fold increase in ignition energy, independent of pressure changes. A similar deterioration in ignition performance with reductions in pressure was also confirmed for a range of fuels. The measured decrease in minimum ignition energy with pressure appeared more pronounced than predicted by theory. The nature of this dependence appears consistent with the general form

$$E_{\min} \propto \frac{1}{P^n}. \quad (2.40)$$

Experimental ignition data acquired during the later studies suggested that the pressure exponent,  $n$ , was between 1 and 1.3, varying with equivalence ratio. Theoretical analysis suggested a much weaker dependence, with the exponent equal to 0.5. This inconsistency derived from an inaccurate assumption associated with the physical model employed.

Extending concepts developed for the analysis of quiescent fuel mists, the devised model proposed that ignition of a heterogeneous mixture is governed solely by the rate of fuel evaporation, remaining independent of chemical reaction rate for a wide range of flow conditions. Good agreement was obtained between measured and predicted values of minimum ignition energy for intermediate to large droplet diameters at atmospheric pressure. As highlighted above however, theoretical projections proved less accurate for conditions producing similar rates of evaporation and chemical reaction; specifically low equivalence ratio mixtures of fine fuel droplets and low-pressure air. Further limitations were apparent for moderate to high turbulence levels. It was suggested that these conditions promoted fuel vapour formation prior to ignition, leading to overestimation of the minimum ignition energy if Eq. (2.31) is used.

Comparison of critical diameter expressions for flowing homogeneous and het-

erogeneous mixtures produced expressions for a critical mean droplet size, below which kinetic effects predominate. For a stoichiometric, monodisperse suspension of kerosene droplets in ambient air, critical droplet sizes of 20  $\mu\text{m}$  and 36  $\mu\text{m}$  were derived for quiescent and flowing mixtures respectively. This theoretical work contributed significantly to the development of a general model for spark ignition, incorporating terms to account for both chemical kinetic effects and fuel vapour formation prior to ignition. Including the chemical reaction time for conditions of low equivalence ratio and pressure yielded a marked improvement in correspondence between theory and experiment.

#### 2.4.4 Laboratory-scale relight experiments

While many studies have investigated the creation of a viable spark kernel, relatively little research has examined the migration and subsequent stabilisation of flame during the second phase of the altitude restart process. These have been explored by Mastorakos and co-workers in several studies using simplified flow configurations that incorporate key aspects of the relight process. These studies are summarised below.

In a simple experiment Ahmed and Mastorakos (2006) investigated spark ignition of a turbulent methane jet in a concentric air-flow. The air-gap spark igniter used to initiate ignition could be positioned at any point in the flow. The developing flame was visualised using a high-speed camera and PLIF of the OH radical. The flame kernel created by the spark was initially spherical, but quickly evolved into a cylinder with a propagating edge that moved upstream. If successful, this flame stabilised at an appropriate liftoff height. The propagation speed of this edge flame relative to the flow was between three and six times the laminar burning velocity, increasing with jet velocity.

Repeated ignition trials were conducted at a variety of spark locations, and the ignitable region of the jet identified. The gas velocity between the electrodes at the

instant of the spark was found to strongly influence ignition outcome, with higher velocities leading to failure. The mean mixture fraction distribution, or flammability map, was estimated using an empirical correlation. The ignitable region was found to be somewhat wider than the flammable region, based on mean mixture fraction contours, indicating that turbulent fluctuations of mixture fraction can cause a lean region to become instantaneously enriched. The convection of developing kernels away from the stabilisation point resulted in an ignition probability of zero in the downstream portion of the jet, despite a favourable mean mixture fraction.

A difference in the areas covered by the flammable and ignitable regions was also observed in a study of turbulent non-premixed counterflow flames (Ahmed et al. 2007b). These results indicated that ignition was possible when the spark was positioned at locations where the mixture fraction lay outside the rich and lean flammability limits. In these cases the mechanism permitting ignition was strong convection of the hot gas kernel from the spark gap to a region of flammable mixture up to 10 mm away.

Ahmed et al. (2007a) designed and constructed a turbulent non-premixed bluff-body burner to study the ignition process in a complex flow field more accurately representing that produced in a gas turbine combustor. A conical bluff body was mounted at the burner exit, and the flame area was enclosed by a quartz cylinder with a diameter of 70 mm. Methane was injected radially into a concentric air-flow, creating a well-defined central recirculation zone. The velocity and mixture fraction fields were determined by means of laser Doppler anemometry (LDA) and acetone PLIF respectively, while the ignition events were again visualised using a high-speed camera and OH PLIF.

Without induced swirl, the mixture fraction in the CRZ was found to be uniform and steady. When the spark occurred inside this zone, successful flame propagated towards the bluff-body edges where it stabilised. When the spark electrodes were located outside the CRZ, successful flame first propagated axially before expand-

ing radially and tangentially to the opposite side of the quartz cylinder. Perhaps unsurprisingly, the highest rate of successful ignition occurred when the spark was located close to the stoichiometric mixture fraction contour at the edge of the CRZ. However, ignition was still achieved inside the CRZ where the mixture was apparently rich. In this case the discrepancy between the flammable and ignitable areas was attributed to local and global fluid mechanics effects and to the comparatively high turbulence levels. Three types of ignition failure were observed corresponding to a spark generating no kernel, kernel initiation followed by subsequent blow-off, and global extinction following successful stabilisation.

Introducing swirl to the air-flow changed the fuel distribution markedly, with the mixture becoming too lean inside the CRZ while mixing improved around the edges of the cylinder. The stability limits were expanded considerably by the swirl, and the ignition and stability limits became closer. Under these conditions a flame kernel generated by a spark at the edge of the quartz cylinder was seen to move tangentially with the flow.

By adding an atomiser to the upstream face of the bluff body it was possible to investigate ignition of a liquid fuel, namely n-heptane, in the same recirculating flow (Marchione et al. 2007, July). As before, the highest rate of successful ignition occurred when the spark was located close to the the edge of the CRZ. Phase Doppler anemometry (PDA) measurements revealed that the mean droplet size decreased considerably along the burner centre-line indicating that large droplets had impinged on the quartz cylinder due to the swirling motion of the flow. Inside the CRZ, the droplets moved away from the injector, against the direction of the mean air velocity. Ignition tests revealed that flame can successfully propagate back towards the burner face under these conditions.

In a separate study undertaken by Marchione et al. (2007, Sep), the influence of multiple sparks on the ignition of recirculating sprays has been assessed. The sparks generated were large and long compared to the length and time scales of the flow.

---

Sparks with an energy of 30 mJ and a duration of approximately 8 ms were repeated at a rate of 100 Hz for periods of between 1 and 5 s. A long spark sequence was found to make ignition possible at a test condition where a single spark consistently failed. This was attributed to the heat deposited during early sparks increasing the ignition probability of later sparks. Furthermore, the likelihood of ignition was a strong function of the igniter's axial location at the edge of the quartz cylinder. Flame kernels generated by the spark were stretched as far as 20 mm from the electrodes by the turbulent motion of the local fluid. This work thus indicated that the energy deposited in multiple sparks can have a spatially far-reaching effect that can significantly increase the likelihood of ignition.

In summary, these laboratory-scale experiments have contributed valuable insight into ignition and flame development processes in gaseous and liquid-fuelled burners operating at atmospheric conditions. It remains to be demonstrated that these phenomena occur inside gas turbine combustion chambers operating at the low temperatures and pressures encountered during high-altitude relight. The current work will clarify the nature of these processes in an actual combustor.

# Chapter 3

## Experimental Method

The objective of the experimental work performed in this study is to characterise the fuel distribution and flame development inside a gas turbine combustor during high-altitude relight. These have been examined using two imaging techniques simultaneously: kerosene PLIF to map fuel placement (see Section 3.2), and high-speed flame emission imaging to record flame activity (Section 3.3). This chapter introduces the techniques and apparatus employed to investigate relight phenomena.

### 3.1 The altitude test facility

The Altitude Test Facility at Rolls-Royce, Derby, was used to simulate the operating conditions generated inside an aeronautical gas turbine combustor following an altitude flameout. Significant modifications to the ATF were necessary to permit high-resolution fuel and flame imaging, to be discussed later in Section 3.2. Firstly, a general description of the layout and operating conditions are given.

#### 3.1.1 Layout

The modified test section is illustrated in Figures 3.1 and 3.2. A two-sector combustion chamber was mounted inside a pressure vessel. The combustion chamber

was a LDI design housing a single fuel injector in the far-side sector. Though the injector was fuel staged, only the pilot atomiser was fuelled during relight tests. The Jet A kerosene fuel fed through the injector was stored at ambient conditions, and supplied in controlled quantities via a mass flow controller.

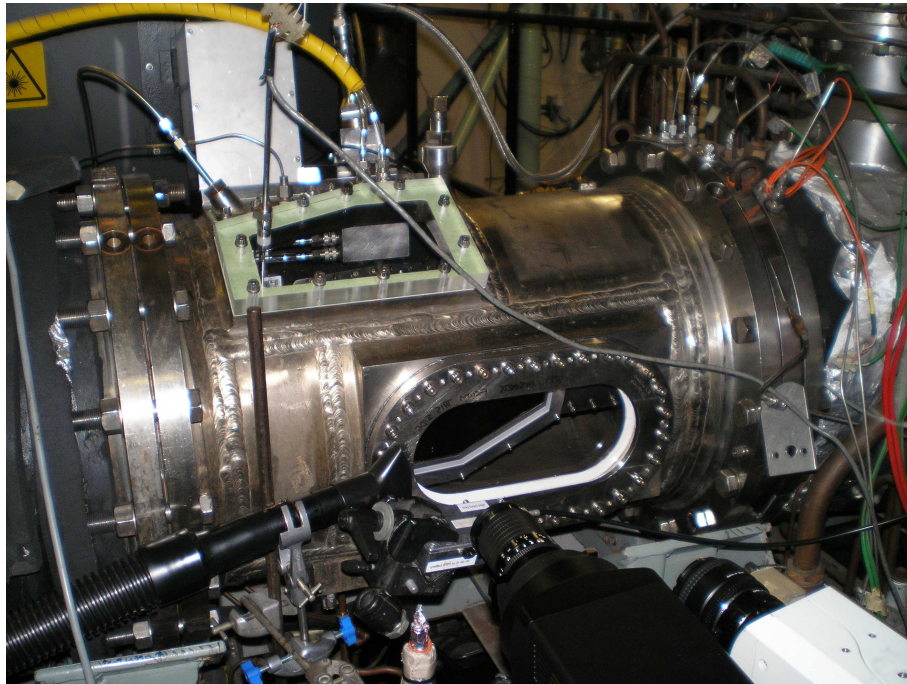


Fig. 3.1: Photograph of experimental apparatus. Flow is from left to right.

A refrigeration unit upstream of the combustor chilled the inlet air. This cold air was drawn through the combustion chamber by a vacuum pump. A drilled plate at the outlet of the combustion chamber restricted the air mass flow rate through the test section. The air pressure and mass flow rate in the combustion chamber were independently regulated by adjusting the pressure drop generated by the pump and the air flow through an upstream control valve. In this manner, it was possible to replicate the conditions inside a lean-burn combustor prior to relight. The two condition set points used during this study are discussed below in Section 3.1.2.

Optical access to the combustion chamber was provided by two quartz windows

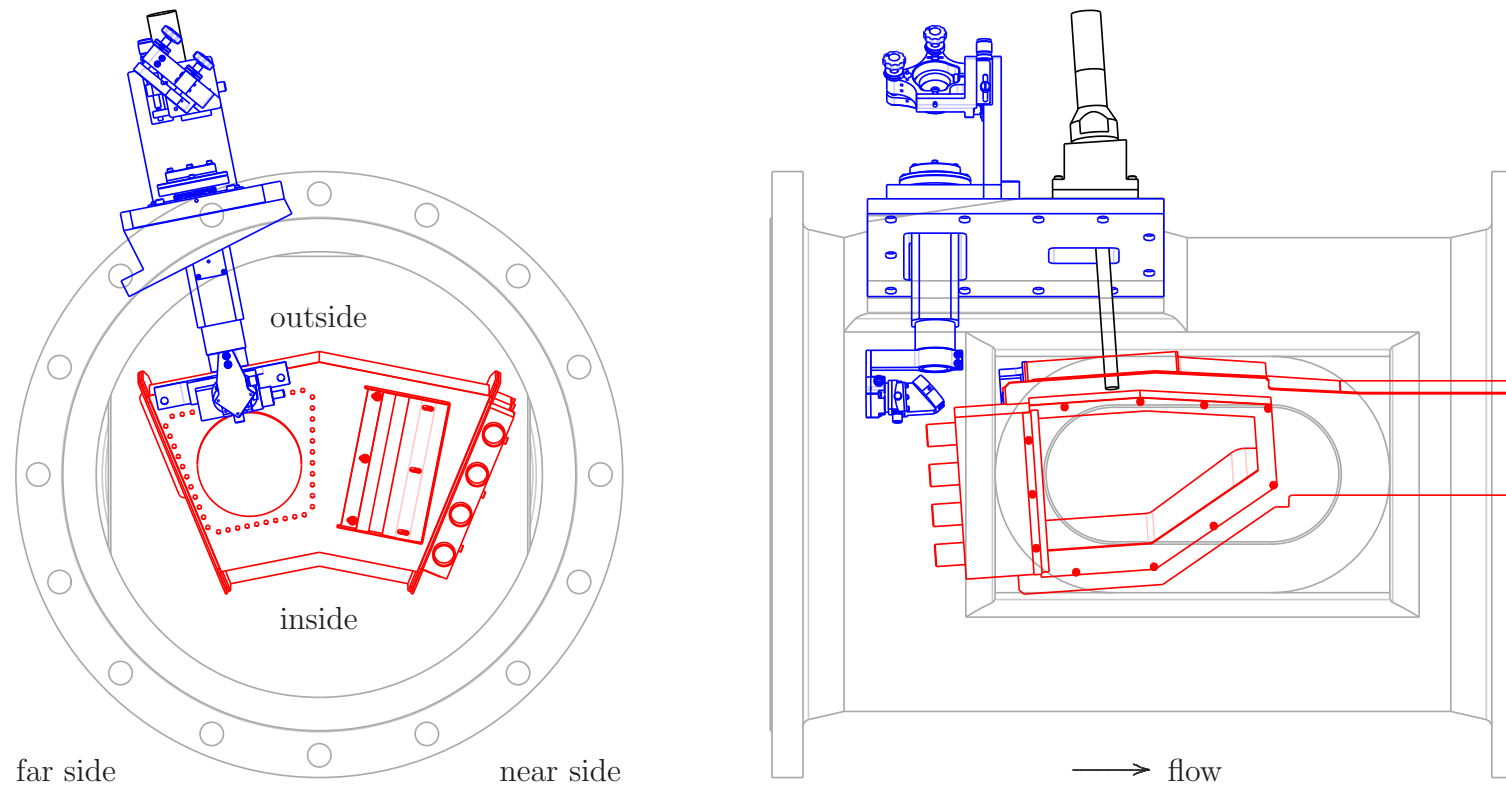


Fig. 3.2: The modified test section. The combustion chamber is shown in red, the igniter in black, the periscope in blue, and the pressure vessel in grey. The internal and external periscope covers are omitted.

on the near side of the test section. The internal window, mounted in the side of the combustor, was susceptible to liquid fuel contamination prior to and following ignition. The near-side injector was therefore replaced by a vertical slot that created an air curtain to prevent fuel deposition on the combustor window. The slot area was adjusted to match the effective area of the fuel injector, thus ensuring an equal air mass flow rate into the combustor at each injector location. Air-flow through the injector and the slot together represented approximately 70% of the total combustor air-flow (not including the additional purge air flows described in Section 3.2.5). In addition, the external pressure-vessel window was warmed to prevent condensation on its outside surface.

The sparks required for ignition were generated by a Champion SK00241 surface-discharge igniter. Introduced from above, the igniter tip was located flush with the outside combustor wall in the injector mid-plane. The energy required to generate each spark was supplied by a Unison Trent exciter unit rated to deliver 10 J per spark at a frequency of approximately 1.3 Hz.

### **3.1.2 Operating condition set points**

Ignition testing was conducted at two high-altitude operating conditions referred to as ‘safe’ and ‘unsafe’ in accordance with the likelihood of achieving ignition; relight is possible at the safe condition but impossible at the unsafe set point. The conditions generated inside the combustion chamber at these two set points are listed in Table 3.1. The safe point corresponds to the conditions inside a lean-burn combustor prior to relight, when the aircraft is flying at 30000 ft (9.1 km) above sea level. These conditions were calculated using the procedure described in Section 2.2.1 to predict the thermodynamic state of the cold combustor air as a function of altitude and air speed.

The sole difference between the two operating conditions is the larger air mass flow rate at the unsafe point. This influences the ignition process in two important

Table 3.1: Safe and unsafe condition set points for relight testing.

	safe	unsafe
$T_{\text{air}}$ (K)	265.0	265.0
$P_{\text{air}}$ (kPa)	41.4	41.4
$T_{\text{fuel}}$ (K)	288.0	288.0
AFR	33.0	60.5

respects. Firstly, as the air flow rate through an air-blast atomiser increases, a finer fuel spray is generated (see Section 2.2.1). The minimum energy required to ignite a droplet spray increases markedly with drop size (Rao and Lefebvre 1976; Ballal and Lefebvre 1978a). A larger air-flow might therefore be expected to favour ignition. However, flame stabilisation is impaired by the reduction in residence time and increase in aerodynamic strain associated with high flow rates (Cohen et al. 1996). These combined effects enable ignition within fourteen sparks at the safe condition, while preventing all successful flame development at the unsafe set point.

## 3.2 PLIF

### 3.2.1 Background

The distribution of fuel inside the ATF facility has been studied using planar laser-induced fluorescence of kerosene fuel. This technique uses a planar sheet of monochromatic light from a laser to excite fluorescent compounds present in the fuel. When a molecule of one of these compounds absorbs an excitation photon, its electronic energy is raised from a ground state to a higher level. In a process known as Stokes fluorescence, some of these excited molecules relax to intermediate energy levels, emitting photons with a longer wavelength than the laser light. By imaging these fluorescence emissions, a two-dimensional representation of the fuel distribution in the sheet plane is recorded. This non-intrusive technique has

been used previously to characterise fuel placement inside internal combustion engines (Arnold et al. 1992; Nygren et al. 2002) and various gas turbine combustion systems operating at simulated take-off or cruise conditions (McDonell et al. 1996; Locke et al. 1998; Kohse-Höinghaus and Jeffries 2002). Fuel PLIF has not, however, been used previously to investigate the altitude relight process.

Numerous commercial fuels, including Jet A kerosene, contain a wide variety of unsaturated and aromatic hydrocarbons that readily absorb ultraviolet light and generate strong fluorescence. Examples of such compounds include the mono-aromatics, benzene and toluene, the di-aromatic, naphthalene, and the polycyclic aromatic hydrocarbon, fluoranthene. Each of these components generates a fluorescence signal that varies with the concentration of the fluorescing species, together with other factors such as the temperature, pressure and composition of the surrounding gases. Furthermore, though aviation fuel standards in the United Kingdom and the United States specify the maximum permissible aromatic content (UK Ministry of Defence 2002; ASTM 2008), significant variation in the concentration of these fluorescent compounds can occur from batch to batch (Goodger 1994). A well-characterised fluorescent compound is therefore frequently added to a non-fluorescing fuel during quantitative studies of fuel concentration inside practical combustors (Schulz and Sick 2005). In the current study the goal is solely to provide a qualitative comparison of the two test conditions, and such measures are consequently unnecessary provided that the fuel used throughout testing is drawn from a single batch.

The low air temperatures at relight conditions coupled with the low vapour pressure of ambient Jet A kerosene (Coordinating Research Council 2004), suggested that the fuel imaged inside the combustion chamber would be largely liquid. The optical performance of the PLIF system was therefore specified according to the fluorescence behaviour of liquid Jet A kerosene. Previous spectroscopic studies indicate that Jet A fuel fluoresces strongly when excited at 266 nm (Black 1995; Löfström

et al. 1996). This wavelength can be readily generated by using non-linear crystals to quadruple the fundamental output of an Nd:YAG laser (1064 nm). Though slight differences are evident, the emission spectra reported in the work of Löfström et al. (1996) and Black (1995) are remarkably consistent, with the signal extending from approximately 300 to 450 nm and containing a single peak at 340 nm. Given the possible batch-to-batch variations in composition noted above, a kerosene sample was drawn from the ATF fuel tank prior to testing, and analysed using a spectrofluorometer. The emission spectrum generated by excitation at 266 nm is plotted in Figure 3.3, and shows good agreement with the profiles reported previously.

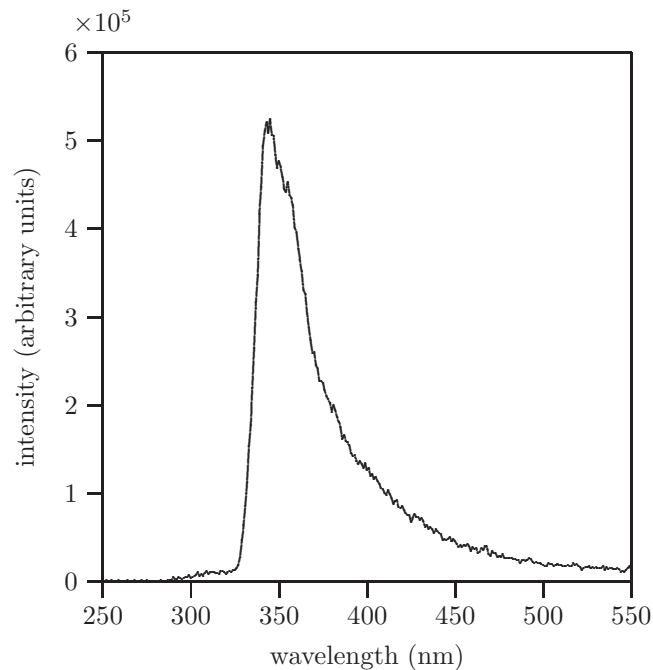


Fig. 3.3: Fluorescence spectrum of Jet A fuel when excited at 266 nm.

While the emission spectrum of the fuel is clearly required for specification of the imaging system, the absorption properties of Jet A are also critical to the success of this work. Measurements reported in Coordinating Research Council (2004) suggest that the fuel is virtually transparent to wavelengths exceeding 300 nm. Re-absorption of emitted photons, a process known as fluorescence trapping, is therefore

avoided. However, ultraviolet light at 266 nm is absorbed extremely strongly by the fuel. This has two important implications for the present study. Firstly, it is critical that the laser sheet is introduced into the combustion chamber via a series of clean optical surfaces, as fuel deposited on a mirror or lens can strongly attenuate the sheet energy. Maintaining the cleanness of optics inside the ATF required the development of several air purge protection systems, as described in Section 3.2.5. Secondly, the laser energy may be significantly attenuated as it passes through a dense spray. If this occurs, then the fluorescence signal does not represent the true distribution of fuel. This phenomenon has been observed in previous studies (McDonnell and Samuelsen 2000; Bazile and Stepowski 1995), and its magnitude in the present work is assessed in Section 5.2.1.

With a knowledge of the absorption and fluorescence characteristics of undoped Jet A kerosene, the PLIF imaging in this study was conducted as follows. The fundamental output beam from a pulsed Nd:YAG laser was frequency quadrupled to 266 nm and formed into a thin sheet. This ultraviolet light sheet was projected into the region of the combustion chamber immediately below the igniter tip.

The induced fluorescence was imaged using a Princeton Instruments PI-MAX2 intensified charge-coupled device (ICCD) camera fitted with a Resolve Optics 60 mm f/3.5 ultraviolet lens and a Hoya B-370 filter. This imaging system recorded the broad-band fluorescence between 300 and 480 nm, registering a peak sensitivity at 370 nm. It was not possible for the camera to view the laser sheet at right angles due to the limited optical access available. The correction required to compensate for this viewing angle is discussed in Section 3.3.2.

### **3.2.2 Beam delivery configuration**

The PLIF measurements of fuel distribution required the projection of a thin laser sheet into the combustion chamber to illuminate the region immediately below the igniter tip. As noted above, it was important to ensure that the projection optics

were protected from fuel droplets and flame products. With this in mind, several sheet projection and imaging configurations were considered.

An initial survey of the ATF suggested passing the laser sheet into the combustor through a quartz window located downstream of the exhaust. This concept was rejected, however, as the exhaust plate obstructed the line of sight to the igniter, and the window was exposed to sooty combustion products. Horizontal projection of the sheet through the near-side window was also discounted due to difficulties in recording unobstructed fluorescence images from above. Furthermore, the incoming laser sheet would have been significantly attenuated by fuel deposited on the internal, side window. This fuel contamination problem also prohibited introducing the laser sheet from above. However, projecting the laser sheet from upstream provided coverage below the igniter tip, while helping to maintain cool, uncontaminated optical surfaces. For these reasons, the laser sheet was introduced into the combustion chamber from upstream through a slit in the heatshield that surrounds the fuel injector.

The path and profile of the laser beam and sheet are illustrated in Figures 3.4 and 3.5. The beam separation, attenuation, and elements of the sheet formation were performed by optics mounted on a table positioned alongside the ATF. A detailed description of this optical table is given below in Section 3.2.3. The partially-formed sheet was projected into the combustor through a custom-built periscope, and expanded by a planar lens mounted above the fuel injector. The design and development of this periscope and sheet expansion assembly is discussed in Section 3.2.4.

### **3.2.3 Optical table**

The Nd:YAG laser required to generate the PLIF excitation wavelength was mounted on an optical board together with the optics responsible for separating, attenuating and geometrically modifying the beam. To reduce the required number of reflective

optics and thus simplify the alignment process, the optical board was supported approximately 1.5 m above the ground by a steel frame. The optical table, comprising this board and frame, is illustrated in Figure 3.4.

The optical table was stably supported by three adjustable feet at the base of the frame, with the centre of mass lying well within the triangle formed by the ground contact points. The length of each foot could be adjusted to set the table height and to level the steel frame relative to the test facility. Two further degrees of freedom were incorporated into the optical table to allow accurate alignment of the laser sheet with the central plane of the far-side combustor sector. Firstly, the upper sub-assembly of the support frame could translate parallel to the flow direction, allowing accurate projection of the beam onto the top mirror of the periscope. Secondly, the optical board could pivot about a horizontal axis located close to its downstream edge. The slight inclination of the optical board apparent in Figure 3.4 ( $\approx 0.8^\circ$ ), was necessary to compensate for the pitch of the upstream combustor wall on which the final sheet-formation lens was mounted.

A Continuum Surelite III-10 laser was used to generate the ultraviolet light sheet required for kerosene PLIF. This pulsed Nd:YAG laser was operated with a Q-switch delay of 300  $\mu\text{s}$ , generating 250 mW at 10 Hz. The shot-to-shot variation in beam energy produced by the laser is considered in Chapter 4. As illustrated in Figure 3.4, the laser head was positioned along the far-side edge of the optical table. The fundamental frequency of the laser (1064 nm) was quadrupled by two non-linear optical crystals to produce light at 266 nm. As each crystal had a doubling efficiency of approximately 50%, the laser beam at the exit aperture contained a mixture of three wavelengths: 266, 532, and 1064 nm. It was therefore necessary to isolate the 266 nm wavelength using a pair of harmonic separators.

Having dumped the residual wavelengths, the ultraviolet beam was directed through a variable power attenuator constructed from a half-wave plate and a thin-film polariser. Using this arrangement, the power in the laser sheet was modulated

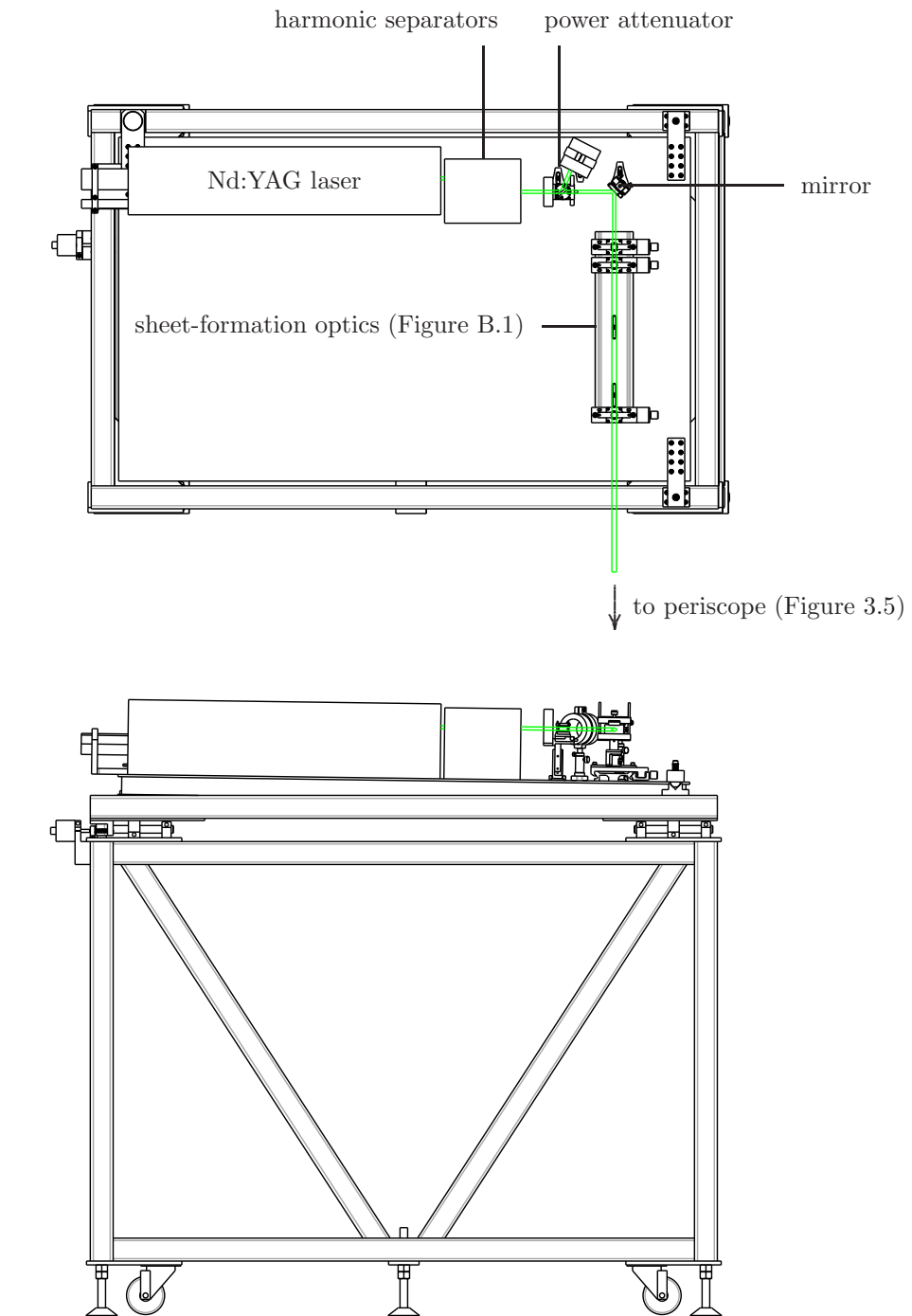


Fig. 3.4: The optical table. The laser beam was projected from the table onto the top mirror of the periscope (see Figure 3.5). The beam path is shown in green.

by rotating the half-wave plate to direct a fraction of the highly-polarised input beam to a dump (Kolner 1991; Krüger et al. 2005). The period between ignition tests could extend to several minutes, as large numbers of images were saved to disk. The attenuator was therefore used to reduce the laser intensity to a minimum during this period, thereby reducing the risk of damaging optics further along the laser path without having to adjust the Q-switch delay.

The initial stages of forming the laser beam into a sheet were performed by three planar lenses mounted on an optical rail. The first two lenses formed a Galilean telescope that expanded the beam in the plane of the optical board. The third lens, mounted at the end of the rail, had a comparatively long focal length ( $\approx 1.4$  m at 266 nm), and caused a gradual thinning of the sheet as it passed through the periscope and into the combustion chamber. This progressive thinning approach was used to reduce the risk of laser damage to the optical components mounted in the periscope and final lens assembly. Dielectric-coated optics were used throughout to maximise the proportion of transmitted or reflected light as appropriate. The changes in beam cross-section produced by these three optics are calculated in Appendix B, and summarised in Table 3.2.

Though elevating the optical board to the height of the periscope simplified the beam alignment and reduced the number of mirrors required, projecting a class IV laser beam at eye level presented a safety hazard. To avoid injury, the laser and optics were fully enclosed throughout testing. During beam alignment, the components mounted on the optical board required adjustment, and an elevated walkway was provided for this purpose.

### **3.2.4 Periscope and sheet expansion assembly**

A periscope was manufactured to direct the laser light from the optical table, through the pressure vessel, and into the combustion chamber. In addition, a final lens assembly mounted on the outside surface of the combustor provided the sheet expansion

necessary to maximise the region of excitation below the igniter tip. The path of the laser light through the modified test section is highlighted in Figure 3.5, while details of the periscope and sheet expansion assembly are illustrated in Figure 3.6.

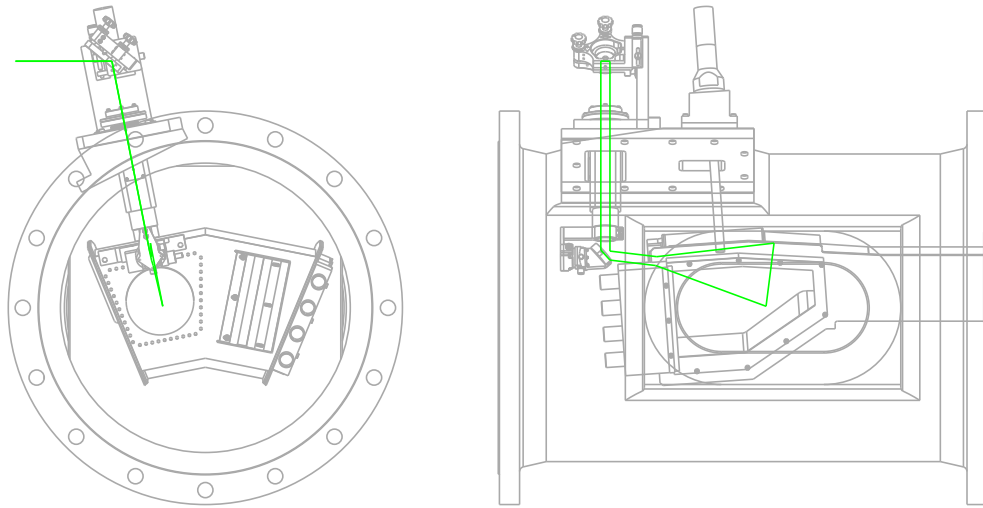


Fig. 3.5: Laser beam path through modified test section. Note that the unclipped sheet extents are illustrated.

The incoming laser sheet struck the centre of the top periscope mirror, and was reflected down along the periscope axis through a quartz window and into the pressure vessel. The sheet continued down before being projected forwards by the bottom periscope mirror into the sheet expansion assembly. This assembly, mounted on the upstream outside surface of the combustor, contained a planar-concave lens that created a diverging sheet in the centre plane of the far-side sector. This sheet passed below the centre of the igniter tip.

The periscope and sheet expansion assembly were designed to fulfil several requirements. Both assemblies were required to fit onto the existing test section, without unduly disrupting the position of the combustor, fuel injector or igniter. As the position of the combustion chamber relative to the pressure vessel was known only approximately, it was necessary to incorporate means of adjusting the posi-

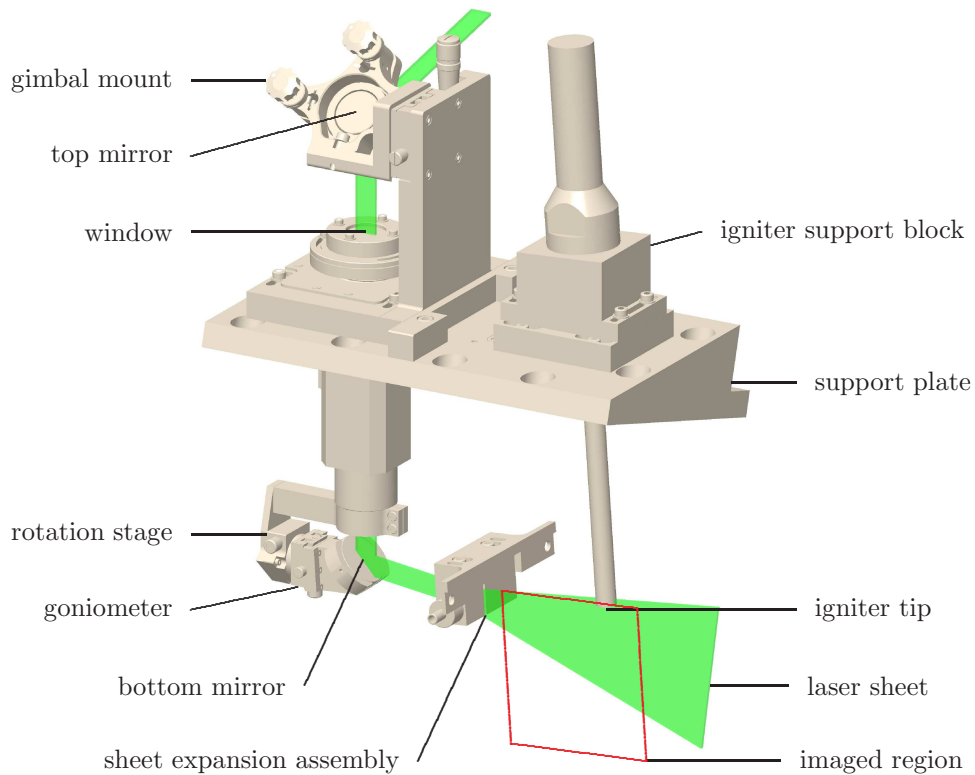


Fig. 3.6: The periscope assembly. The unclipped sheet extents are shown, and the red square indicates the area of the PLIF image.

tion and orientation of the mirrors and lens to ensure accurate alignment of the laser sheet. Notwithstanding these degrees of freedom, stable retention of the optics following alignment was also necessary. An additional requirement was that all components must either tolerate or be protected from condensation and liquid kerosene. As the operating pressure is sub-atmospheric, the periscope as a whole also needed to seal the pressure vessel effectively. A final design requirement was that cooling the periscope and sheet expansion assembly from ambient temperatures to the 265 K test condition must not adversely affect the adjustment mechanisms or cause additional leakage of air into the pressure vessel.

As illustrated in Figure 3.2, the periscope support plate was mounted on the far side of the pressure vessel, replacing the original igniter mounting plate. An

adjustable igniter support block was manufactured to ensure that the igniter tip could be accurately positioned relative to the internal surface of the combustion chamber.

Adjustments to the upper and lower mirror positions and orientations were achieved by several means. The periscope shaft consisted of three concentric tubes that provided two degrees of freedom. The outside support tube remained stationary. The middle cylinder could translate  $\pm 15$  mm axially by rotating a threaded drive ring. The inside tube could rotate  $\pm 45^\circ$  relative to the middle cylinder. The quartz window was mounted at the top end of this inside tube. Despite the axial load on this assembly that resulted from the sub-atmospheric operating conditions inside the pressure vessel ( $\approx 36$  N), free rotation was provided by incorporating a needle roller thrust bearing. The bottom mirror assembly was clamped to the inside tube, and could thus rotate and translate in a controlled manner.

To ensure free movement while minimising leakage, the concentric periscope tubes were manufactured according to tight geometric tolerances, with dissimilar materials at interfacing surfaces. The materials used were an austenitic stainless steel (BS EN 1982:1999), and a phosphor bronze (BS EN 10088-2:2005). These widely-available metals are corrosion-resistant and have an identical linear coefficient of thermal expansion, preventing differential thermal expansion or contraction. Both the inside and middle cylinders were clamped in position following laser alignment, though little force was required to achieve this due to the low vibration levels and aerodynamic loading generated by the air-flow.

The height and angle of the top periscope mirror were adjusted to ensure that the sheet was projected along the axis of the periscope shaft. This was achieved using the translation stage and gimbal mount illustrated in Figure 3.6. The pitch and roll of the bottom mirror were controlled independently by a goniometer and a rotation stage respectively. In addition to the positional and rotational adjustments described above, the lateral position of the periscope assembly relative to its support

plate could also be modified.

To prevent air leakage into the pressure vessel, glass and aramid fibre gaskets were used to seal flat metal contact surfaces. The periscope window was supported between polytetrafluoroethylene (PTFE) seals that protected the anti-reflection coating, while spreading the load generated by the sub-atmospheric operating pressure. The bottom mirror, goniometer and rotation stage of the periscope were enclosed by a protective cover (see Figure 3.10(b)). As discussed in Section 3.2.5, ingress of dust and fuel droplets through the laser exit slit was prevented by a purge of clean air.

Condensation of water vapour on the periscope optics as a result of the low operating temperatures would have compromised the quality of the PLIF results and caused subsequent laser damage to the dielectric coatings. While driers removed virtually all water vapour from the air flowing through the test facility, condensation on the outside surface of the test section was likely due to the sub-zero operating temperature. The severity of this condensation is determined by the atmospheric conditions in the test cell, and the specific heat capacity of the test section. If the relative humidity in the test cell is  $\psi$  at temperature  $T_{\text{amb}}$ , then the corresponding dew-point temperature is given by

$$T_{\text{dp}} = T_{\text{sat}}(P_v) \quad \text{where} \quad P_v = \psi P_{\text{sat}}(T_{\text{amb}}) \quad (3.1)$$

(Çengel and Boles 1998). Thus, if  $\psi = 75\%$  at  $T_{\text{amb}} = 20 \text{ }^\circ\text{C}$ , then

$$T_{\text{dp}} = 15.3 \text{ }^\circ\text{C}. \quad (3.2)$$

As each test session was envisaged to last for several hours, there was a significant risk that the surface temperature of the periscope would fall below this value. Two mats containing heating elements were therefore installed to prevent condensation forming on the periscope optics. A small mat generating 2 W of heat was wrapped around the window housing. A larger, 5 W, mat was attached to the vertical plate supporting the top mirror assembly. Thermocouples monitored the temperature of

each heating mat and a thermostatic controller regulated the supply of energy to maintain a local temperature of 70 °C. This system successfully prevented misting of the top mirror and window.

The sheet expansion assembly was mounted above the fuel injector, on the far-side, upstream face of the combustion chamber. The space required for the assembly was provided by inverting the fuel injector so that the fuel lines that normally occupy this space were moved to the bottom. The expansion lens was positioned as close as possible to the upstream combustor face to maximise the excitation area. This lens was mounted in a brass cylinder that rotated inside a housing to permit adjustment of the inclination. The sheet passed into and out of the lens through a slit in the housing. As described in Section 3.2.5 and illustrated in Figure 3.10(c), clean purge air introduced into the brass cylinder flowed out through the slot, thus preventing the admission of fuel droplets and dust.

Table 3.2: Beam dimensions at principal point of each lens.

lens number	width (mm)	thickness (mm)
1	8.0	8.0
2	12.0	8.0
3	12.0	8.0
4	12.0	1.8

Burn marks produced on photographic paper suggested that the diameter of the beam was approximately 8 mm on exiting the laser head. A computer-aided design (CAD) model of the optical table and periscope recorded the position and orientation of each optical component. Using this information, the beam cross-section was calculated at every point along the optical axis, as described in Appendix B. The cross-sectional dimensions of the beam at the appropriate principal plane of each lens are summarised in Table 3.2.

An investigation of the beam dimensions performed following testing revealed

that the upper and lower sheet boundaries had been slightly clipped by the lens mount and the fuel injector respectively. The boundary angles were therefore recalculated from geometric information provided by the CAD model. The unclipped sheet expansion angle was recorded to provide a reference for the beam energy distribution correction. The position of the sheet relative to the combustion chamber was also calculated from the model.

The clipped region of excitation is illustrated in Figure 3.7. Note that the sheet thickness varies considerably inside the combustion chamber. Coupled with the  $27.3^\circ$  expansion, this causes significant point-to-point differences in the laser irradiance. PLIF image corrections for these variations are described in Section 5.2.

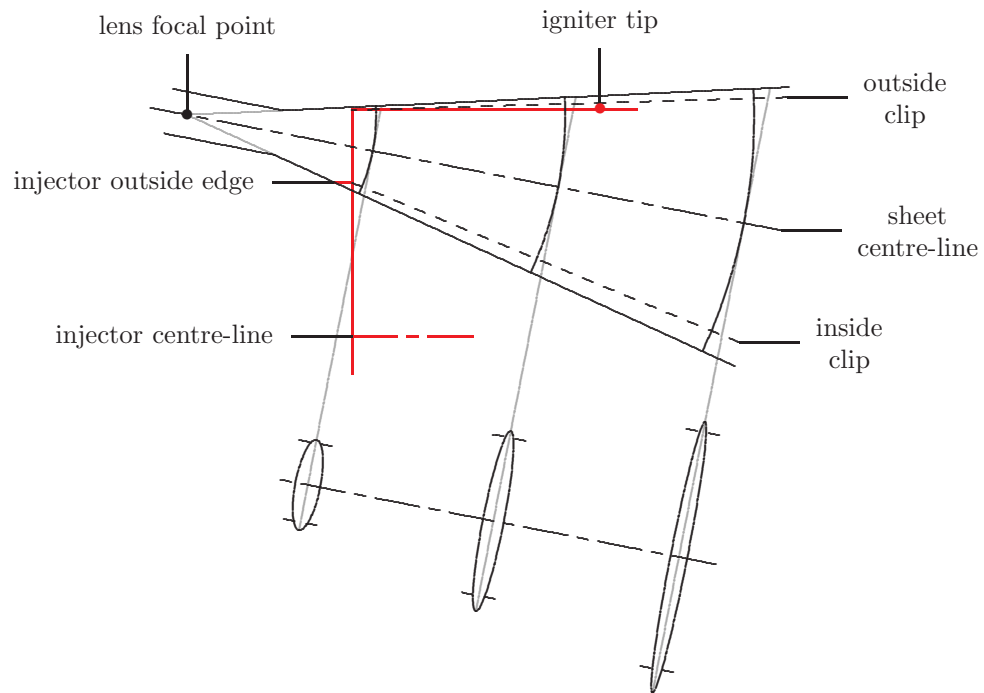


Fig. 3.7: The excitation volume inside the combustion chamber. Note that the sheet thickness in each cross-section has been scaled by a factor of four.

### 3.2.5 Air purges

Three air purge systems were developed to keep the optics clear of fuel. The internal surface of the combustor window was protected by a curtain of filtered purge air drawn into the combustion chamber from outside the pressure vessel. In addition, comparatively small flow rates of cylinder air were introduced separately into the enclosures surrounding the periscope bottom mirror and the sheet expansion lens. Contamination of the optical surfaces was prevented by discharging this air through apertures provided for the laser sheet.

As noted in Section 3.1.1, the near-side fuel injector mounted inside the ATF was replaced by a vertical slot. Though the resulting air curtain reduced liquid fuel impingement on the combustor window, an additional purge system was required to minimise contamination and thereby improve the quality of all acquired images.

The combustor window purge system is illustrated in Figure 3.8. The sub-atmospheric operating pressure inside the combustion chamber draws air in from outside the pressure vessel and discharges it along the upstream edge of the combustor window. Incoming air passes through a filter and a ball valve before flowing into a manifold. Four pipes, each with an internal diameter of 19 mm, feed the air through the pressure vessel wall and into a plenum 18 mm × 52 mm × 145 mm situated immediately upstream of the combustor window. The flow then accelerates through a slot 3 mm × 123 mm onto the internal surface of the window.

The ball valve provides a means of regulating the mass flow rate of purge air. Though the ATF vacuum pump was capable of maintaining the set point pressure with the valve completely open, introducing significant extra quantities of air in this manner has the potential to modify the processes under investigation. It was therefore necessary to assess the air mass flow rate entering the combustion chamber through this system.

The mass flow rate of air passing through the slot has been estimated by performing a one-dimensional compressible flow calculation. The air is assumed to have

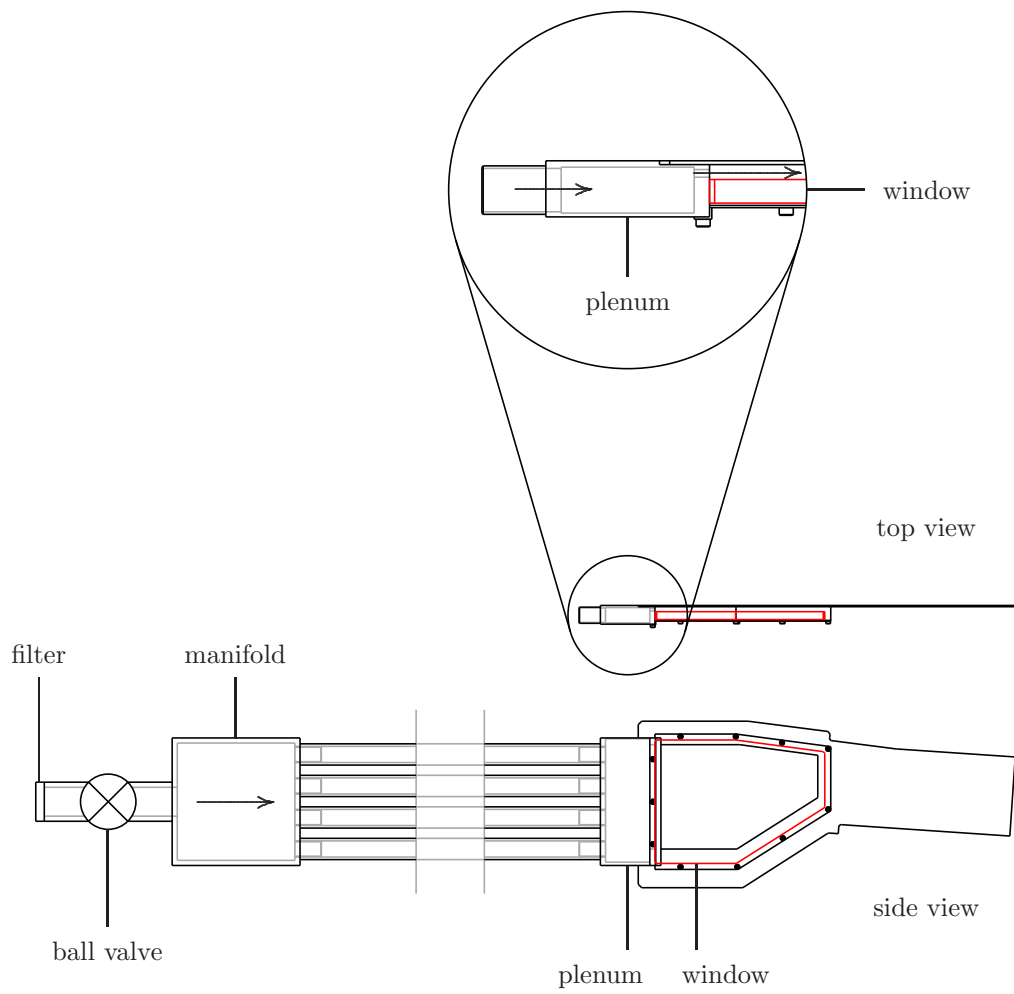


Fig. 3.8: The combustor window purge system. The window itself is shown in red.

negligible kinetic energy as it enters the plenum. In addition, if the flow through the slot is adiabatic and isentropic then the stagnation temperature and pressure,  $T_0$  and  $P_0$  respectively, remain constant throughout. Assuming the flow is steady, the mass flow rate through a slot of area  $A$  is

$$\dot{m} = \rho AV = AMP \sqrt{\frac{\gamma}{RT}}, \quad (3.3)$$

where  $M$  is the local Mach number,  $P$  is the static pressure,  $T$  is the static temperature, and  $\gamma$  and  $R$  are the specific heat ratio and gas constant of air respectively. For an ideal gas flowing isentropically, the static and stagnation values of temperature and pressure are related as follows

$$\frac{T_0}{T} = 1 + \left( \frac{\gamma - 1}{2} \right) M^2, \quad (3.4)$$

$$\frac{P_0}{P} = \left[ 1 + \left( \frac{\gamma - 1}{2} \right) M^2 \right]^{\gamma/(\gamma-1)}. \quad (3.5)$$

Re-expressing Eqs. (3.4) and (3.5) in terms of  $T$  and  $P$  respectively, and substituting into Eq. (3.3) gives

$$\dot{m} = AMP_0 \sqrt{\frac{\gamma}{RT_0}} \left[ 1 + \left( \frac{\gamma - 1}{2} \right) M^2 \right]^{-(\gamma+1)/2(\gamma-1)}. \quad (3.6)$$

The mass flow rate of air is therefore governed by the stagnation properties, the slot area and the Mach number at the slot. If the plenum stagnation temperature and combustor static pressure are assumed to remain constant, then the mass flow rate is governed solely by the plenum stagnation pressure. This pressure increases as the ball valve is opened.

The flow becomes choked when the following condition is satisfied

$$\frac{P_0}{P} \geq \left( \frac{\gamma + 1}{2} \right)^{\gamma/(\gamma-1)} = 1.89. \quad (3.7)$$

When the valve is first opened, the stagnation pressure is not significantly higher than the static pressure at the slot. In this unchoked case, the throat static pressure is equal to the combustor pressure, and the Mach number is identified from Eq. (3.5).

The mass flow rate then follows from Eq. (3.6). As the valve is opened further however, the slot becomes choked and  $M = 1$ . In this case, Eq. (3.6) simplifies to

$$\dot{m} = AP_0 \sqrt{\frac{\gamma}{RT_0}} \left( \frac{\gamma + 1}{2} \right)^{-(\gamma+1)/2(\gamma-1)}. \quad (3.8)$$

In this manner the mass flow rate was calculated for a range of stagnation pressures, and the characteristic curve is plotted in Figure 3.9(a). The plenum pressure was monitored during testing using a digital manometer, and the valve adjusted to maintain a set point value of 56 kPa (cf. combustor pressure of 41.4 kPa). The purge air discharged at this set point was sufficient to essentially eliminate fuel impingement on the window. Importantly, the calculated purge mass flow rate does not constitute a significant fraction of the total combustor air, so the combustor flow patterns are not expected to be radically disturbed by the influx of purge air.

The air mass flow rate plotted in Figure 3.9(a) is almost certainly an overestimate of the true flow rate. While the assumptions of negligible kinetic energy in the plenum and adiabatic flow are broadly accurate, flow through the slot is likely to be highly non-isentropic. Furthermore, the cross-sectional area of the vena contracta associated with this flow is significantly smaller than the slot area. A discharge coefficient has not been applied to account for these effects, and the mass flow rate estimates are therefore conservative.

Relatively small flow rates of air were used to protect the periscope bottom mirror and sheet expansion lens, each purge representing 0.5% of the air mass flow rate flowing through a single injector sector at the safe condition. Polyurethane tubing carried clean, dry air from high-pressure cylinders to enclosures surrounding each optic. This air then flowed from the two enclosures through slots machined to allow passage of the laser sheet, thus preventing the ingress of dust and fuel droplets. Drawings of the protective enclosures are provided in Figures 3.10(b) and 3.10(c).

The mass flow rate of air introduced in this manner was regulated by inserting a short metal pipe containing a 1 mm diameter orifice into each supply line. This pipe is illustrated in Figure 3.10(a). As the combustor set point pressure was only

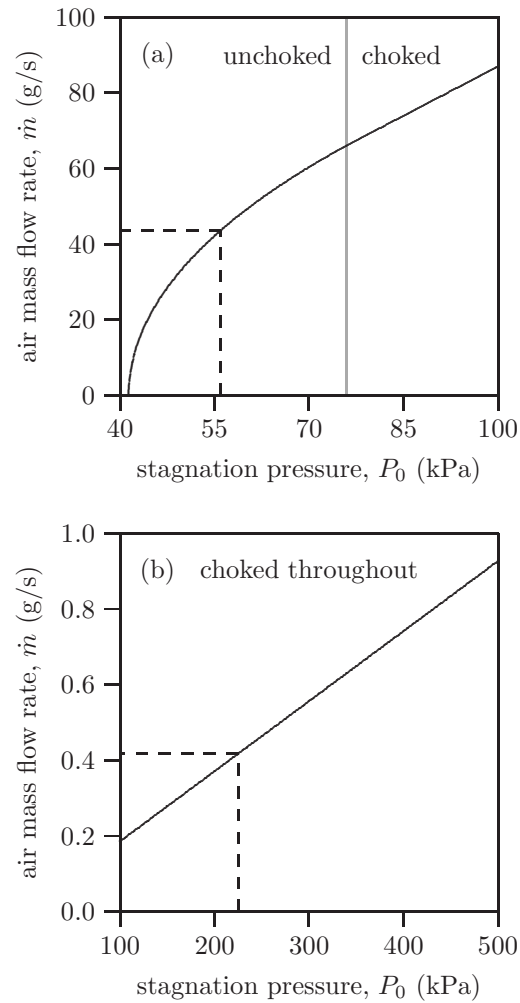


Fig. 3.9: Air purge characteristic curves: (a) combustor window; (b) periscope bottom mirror and sheet expansion lens. The operating points are indicated by dashed lines.

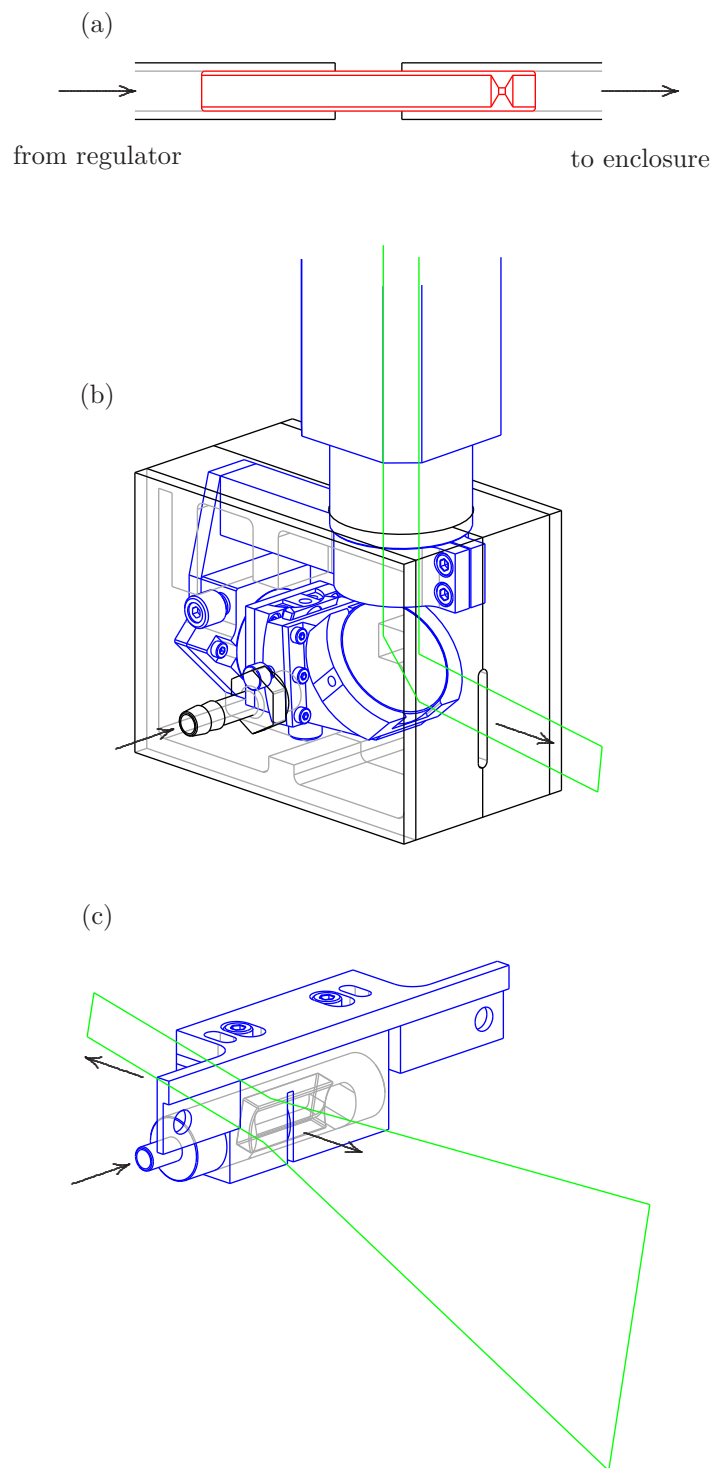


Fig. 3.10: The periscope and sheet expansion purge systems: (a) choking pipe; (b) periscope enclosure; (c) sheet expansion lens enclosure. Arrows indicate the direction of air-flow.

41.4 kPa, any upstream pressure supplied by the regulator was sufficient to choke the orifice (see Eq. (3.7)), thus fixing the mass flow rate through each enclosure. Using Eq. (3.8) it was therefore possible to derive a characteristic curve relating the air mass flow rate to the upstream stagnation pressure set using the regulator. This curve is plotted in Figure 3.9(b).

A set point pressure of 225 kPa was used throughout testing and proved effective in preventing contamination. The additional mass of air introduced through the periscope and sheet expansion lens enclosures is clearly insignificant compared to that associated with the combustor window purge.

### **3.3 High-speed flame imaging**

#### **3.3.1 Background**

Combustion of a hydrocarbon fuel causes the emission of electromagnetic radiation. The spectrum of this emitted light provides information concerning the species present in the flame. For small, Bunsen-type flames the maximum emission usually occurs in the near infra-red part of the spectrum, where distinct bands reveal transitions in the vibrational energy levels of H<sub>2</sub>O, CO<sub>2</sub>, and CO molecules (Gaydon 1974). While the stable products of combustion do not emit strong visible or ultra-violet radiation, many of the unstable free radicals produced in the flame reaction zone generate characteristic bands in these spectral regions. This process, referred to as chemiluminescence, results from electronic transitions in molecules such as OH, CH, and C<sub>2</sub>. For example, excited OH and CH produce strong discrete emissions at 306.4 and 431.5 nm respectively, while the Swan bands, generated by the excited C<sub>2</sub> radical, have outstanding heads at 473.7, 516.5, and 563.6 nm.

While point-wise and two-dimensional measurements of these narrow-band emissions have provided insights into reaction zone equivalence ratio (Muruganandam et al. 2005) and flame structure (Ikeda et al. 2002) respectively, small particles

formed inside some flames profoundly affect the emission spectrum. Most important amongst these is the soot that is often produced in fuel-rich flames (Gaydon and Wolfhard 1970). The radiation emitted by these large organic compounds has a broadly continuous spectrum resembling that of a black body at the flame temperature.

The spectra produced by liquid-fuelled gas turbine flames of the type considered in this study, depends on the composition and state of the fuel and oxidant, together with the mixture equivalence ratio and droplet size. When the fuel is pre-vapourised or very finely atomised, a premixed flame results that emits a Bunsen-type spectrum featuring clear OH, CH, and C<sub>2</sub> bands. However, most flames generated inside aviation gas turbine combustors are only partially premixed and may therefore contain large droplets that are surrounded by a local diffusion flame. In these flames the continuum emission generated by hot particles is dominant, resulting in a yellow appearance. The low temperatures and poor atomisation generated during the present study produced a highly nonpremixed, sooty, yellow flame.

The high-speed flame imaging performed in this study recorded broad-band emissions generated during spark ignition and flame development. A Vision Research Phantom high-speed camera situated on the near side of the ATF, and viewing roughly perpendicular to the flow direction, recorded line-of-sight flame emissions during both successful and unsuccessful ignition events. The spectral sensitivity of this camera is illustrated in Figure 3.11, and extends from approximately 400 to 1000 nm, with a peak quantum efficiency of 40% at 660 nm. The high-speed camera was fitted with a Nikon 28 mm f/2.8 lens that transmitted wavelengths between approximately 350 and 900 nm.

As the flame emission due to soot is predominantly generated in areas of rich combustion, regions of stoichiometric or lean combustion are more clearly identified by imaging an individual excited radical (Smith and Sick 2005). However, the weaker narrow-band emissions generated by CH, or C<sub>2</sub> were not individually filtered and

recorded due to the limited dynamic range of the camera at high recording rates. Indeed, as explained in Section 4.3.1, even without a filter the camera could not retain the broad-band signal at all times due to large changes in the measured flame intensity during each ignition event. An intensifier was not fitted to the camera due to the associated reduction in spatial resolution.

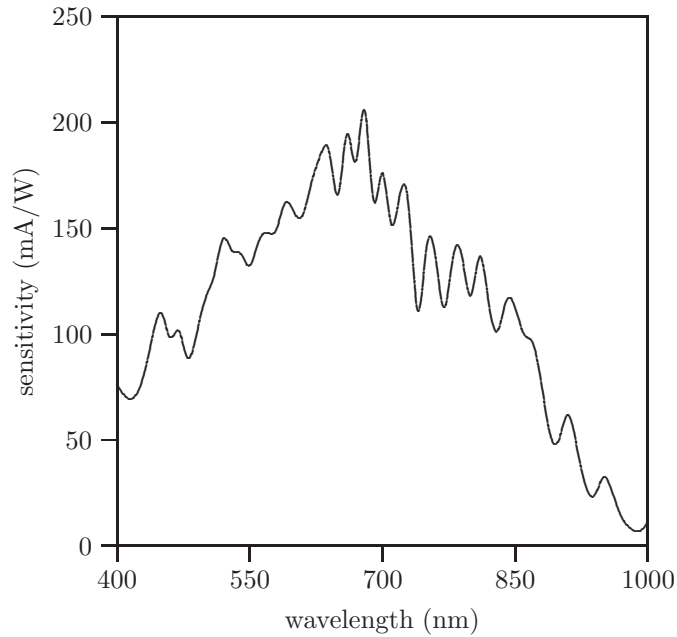


Fig. 3.11: Spectral sensitivity of high-speed camera. Data courtesy of Vision Research Inc.

The horizontal and vertical pixel resolution was set to 384 and 256 respectively. Images were recorded at a rate of 5.7 kHz, with an exposure of 165  $\mu$ s. Though each recording was limited to 1.96 s, the pre-trigger interval could be adjusted. As described in Section 3.4, this feature was utilised to capture the successful ignition event and preceding unsuccessful event at the safe set point.

### 3.3.2 Viewing angle

The position of the PLIF and flame cameras during testing is illustrated in Figure 3.12. Note that throughout this study neither camera could view the laser sheet

plane at right angles due to the limited optical access available. In order to extract geometric information from, and apply PLIF corrections to, the recorded images (see Sections 6.2.3 and 5.2 respectively), a viewing angle correction was required to map vectors in the sheet plane to the camera images and vice versa.

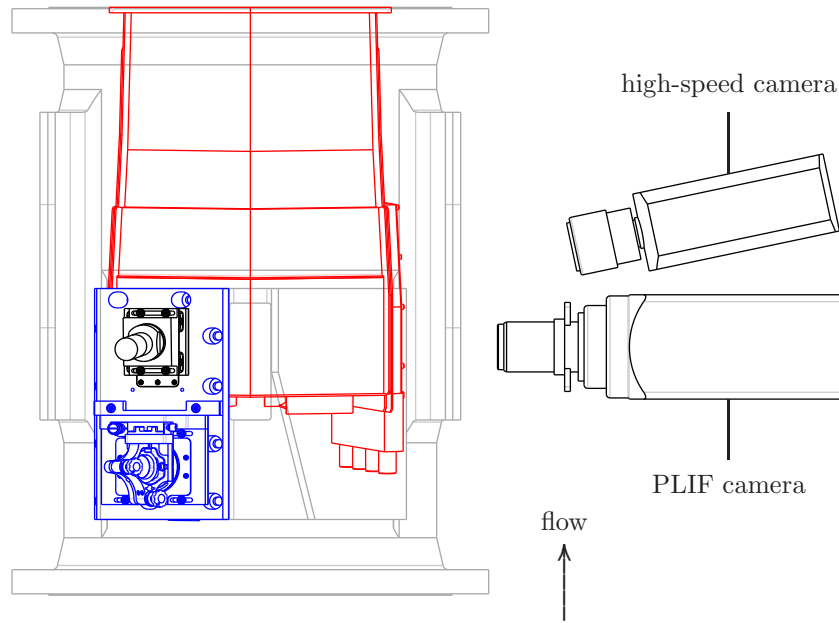


Fig. 3.12: Plan view of test section including cameras. See Figure 3.2 for description of line colours.

The viewing angle correction is derived in Appendix A and is expressed in the form of a single matrix transformation equation for each camera view. The general form of these transformation equations is

$$\begin{bmatrix} u \\ v \end{bmatrix} = \begin{bmatrix} M_{11} & M_{12} \\ M_{21} & M_{22} \end{bmatrix} \begin{bmatrix} u^* \\ v^* \end{bmatrix}, \quad (3.9)$$

where  $u$  and  $v$  are sheet-plane translations parallel to the outside and upstream walls of the combustor respectively, and  $u^*$  and  $v^*$  are horizontal and vertical translations in the image. The elements of the transformation matrix  $M_{ij}$  are calculated from an image of a square calibration target aligned with the laser sheet.

### 3.4 Timing and data acquisition

Data was acquired with the experimental apparatus operating in three different modes. PLIF images of cold fuel were recorded in short sequences without operating the high-speed camera. In order to capture images of fuel distribution and flame activity during ignition at the safe and unsafe set points, two separate methods of triggering were devised. A general description of the apparatus for timing and data acquisition is described below, followed by detailed descriptions of each of the three modes.

Images of fuel and flame together with data describing the performance of the test facility were recorded concurrently to allow investigation of possible interactions between the measured variables. As data from several sources was acquired simultaneously, a timing and data acquisition system was developed to control triggering of the laser, cameras, and spark, while monitoring the igniter current, the flame luminosity, and the performance of the ATF. The design of this system was heavily influenced by timing considerations, specifically those relating to the spark and the laser shot.

The proprietary surface-discharge ignition system used throughout testing provided no control of spark timing. Though rated to deliver sparks at a nominal frequency of 1.3 Hz, the spark-to-spark interval generated by this system was observed to vary between 700 and 850 ms. While this suggested triggering the laser and PLIF camera from the spark, modifying the 10 Hz repeat rate of the laser can adversely affect the shot-to-shot beam energy distribution by causing thermal lensing variations in the Nd:YAG rod (Koechner 1970; Song et al. 2000). For this reason the timing of the spark and laser were decoupled and PLIF images were acquired at a random interval following each spark. While minimising laser energy fluctuations, this timing strategy required a large number of tests to ensure that PLIF images of the flame development phase were captured (see Sections 4.3.1 and 4.3.2).

### 3.4.1 General setup

A schematic of the timing and data acquisition hardware is presented in Figure 3.13. This figure illustrates the apparatus required for fuel and flame imaging at the safe condition (see Section 3.4.4). As described in Sections 3.4.2 and 3.4.3, the control system was simplified for cold fuel imaging and ignition testing at the unsafe set point. The two control boxes labelled ‘PLIF’ and ‘spark and flame’, provided fast control triggers to activate the laser and cameras at appropriate times. The signals fed to and from these boxes during safe ignition testing are illustrated in Figure 3.14.

During all tests, the PLIF control box regulated the timing of the laser shot and the intensifier gate. Pulses to trigger the flashlamp discharge and the Q-switch were sent to the laser at a rate of 10 Hz (see Figures 3.14(e) and 3.14(f)). The separation of these trigger pulses was set to 300  $\mu\text{s}$  to regulate the laser energy (25 mJ per pulse). In response to the input signals, the laser generated a sync out trigger approximately 700 ns before producing the 4 ns laser shot (see Figure 3.14(g)). Though every sync out trigger was returned to the PLIF control box, only a minority of these pulses were fed through to the intensified camera to trigger acquisition of a PLIF image. As discussed in Sections 3.4.2 to 3.4.4, the selected pulse depended on the mode of operation.

In addition to this hardware, the overall conduct of all tests was controlled and monitored by a National Instruments SCXI data acquisition system running purpose-written software in the LabVIEW development environment. This software controlled the progress of a single test as follows. Having generated the desired test condition inside the ATF, the program started, and reported the combustor operating conditions at 1 s intervals (i.e. total air mass flow rate, air temperature, air pressure, fuel mass flow rate, and fuel temperature). Both cameras were then primed to receive their trigger signals. After activating and stabilising the laser output, and adjusting the beam attenuator to maximise transmission, the test conditions were recorded once further before fuel was injected into the combustion chamber. After

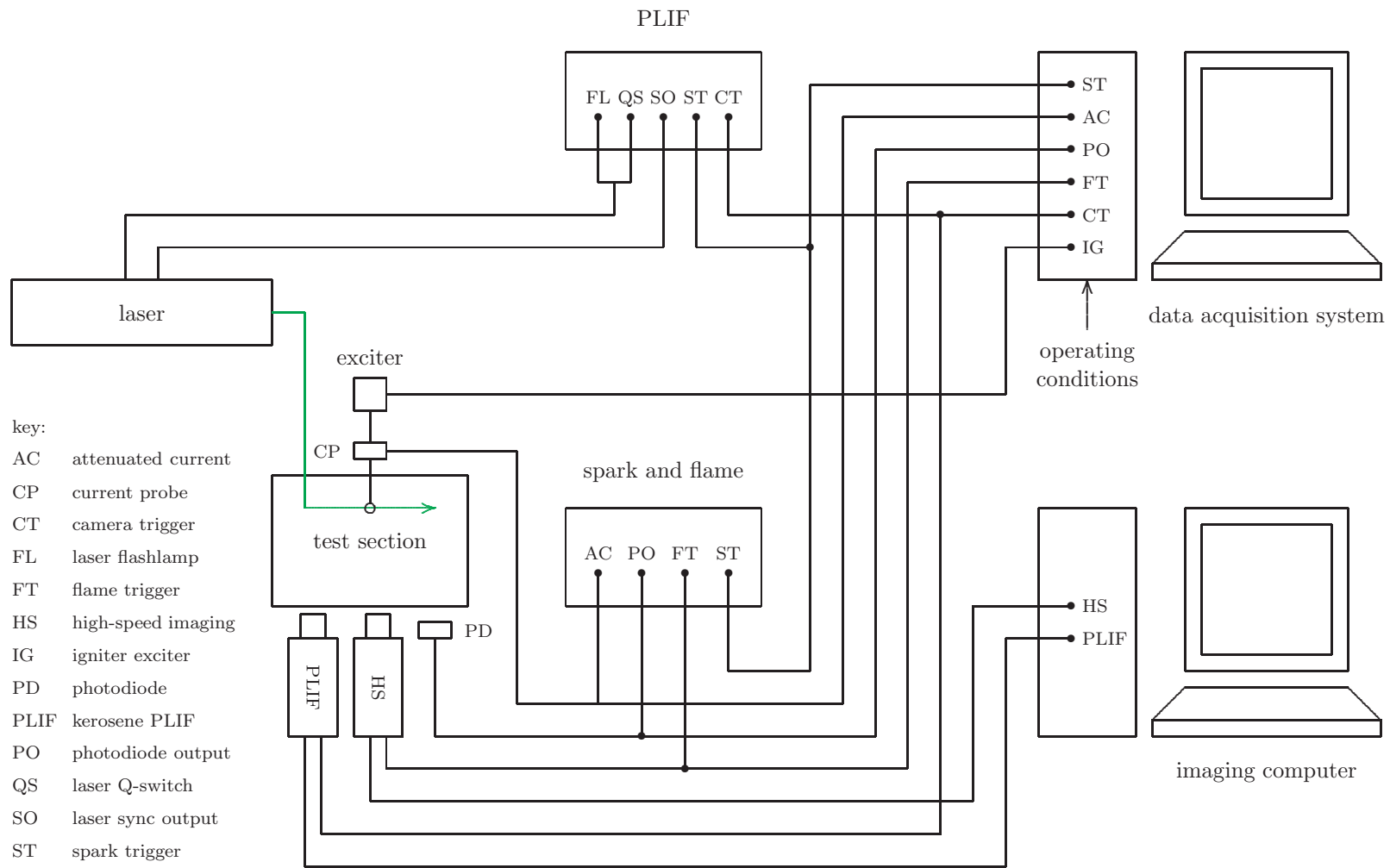


Fig. 3.13: Timing and data acquisition hardware

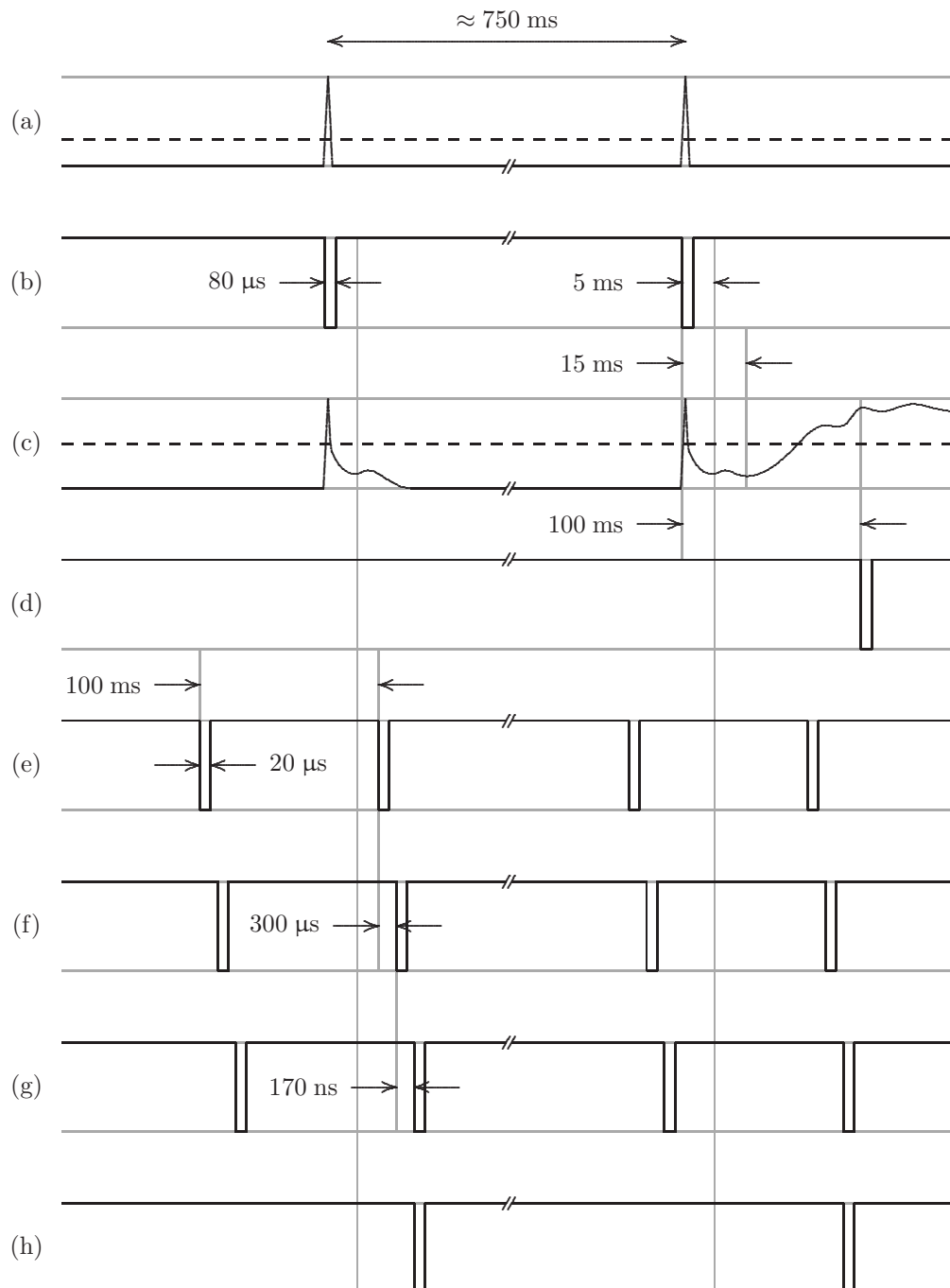


Fig. 3.14: Timing of data acquisition (not to scale): (a) attenuated current; (b) spark trigger; (c) photodiode output; (d) flame trigger; (e) laser flashlamp trigger; (f) laser Q-switch trigger; (g) laser sync out trigger; (h) camera trigger.

a two second delay for fuel flow stabilisation, data was acquired in a manner determined by the mode of operation (see detailed descriptions below). On completion of the test, the fuel was switched off, all data were saved to disk, and the program returned to monitoring the ATF operating conditions. A delay of 60 s was necessary prior to the next test, both to provide sufficient time for data storage, and to allow the dispersion of liquid fuel that had accumulated in the bottom of the combustion chamber.

### **3.4.2 Cold fuel imaging**

The simplest mode of operation was that used for PLIF imaging of fuel without flame. Since no spark was produced, the fuel image could be freely acquired at any instant without danger of damaging the camera. In addition, the high-speed camera was not used, and consequently required no trigger signal. Though the acquisition of a single PLIF image could occur at any time, the full-resolution frame rate of the camera was limited to 4 Hz. For this reason, cold images of fuel distribution were acquired at a rate of 2 Hz.

After the two second fuel flow stabilisation period, a series of 10 PLIF images were recorded at 0.5 s intervals. This was achieved by using the PLIF control box to pass every fifth laser sync out trigger to the intensified camera. A short period after receiving the trigger signal, the camera intensifier was gated for a period of 100 ns, with the gate delay adjusted to coincide with the laser shot.

### **3.4.3 Fuel and flame imaging at unsafe condition**

The following data acquisition procedure was employed during unsafe ignition testing. After fuel flow stabilisation, the spark exciter unit was switched on, and proceeded to generate a spark approximately every 750 ms. By operating the two cameras in tandem, PLIF images were acquired shortly following each spark, and high-speed recordings of flame were captured during the early ignition attempts.

Special care was required to protect the intensified camera from high-intensity emissions generated by the spark. A test consisted of ten consecutive sparks, following which the spark exciter and the fuel supply were turned off.

During ignition testing at the unsafe condition it was necessary to control the timing of the PLIF image acquisition relative to the spark. A Tektronix TCP303 current probe and TCPA300 amplifier detected the spark by measuring the current passing along the lead between the exciter unit and the igniter. The analogue signal from the amplifier (see Figure 3.14(a)) was continuously monitored by the spark and flame control box and compared to a preset threshold of 2.5 V. A negative-going spark pulse was produced when the signal generated by the spark increased to exceed this threshold (see Figure 3.14(b)). This spark trigger was directed to the PLIF control box.

The sync out trigger corresponding to the laser shot following detection of a spark was fed to the intensified camera provided that the shot occurred more than 5 ms following the spark (see Figure 3.14(h)). This buffer period ensured that the initial luminosity of the spark did not cause damage to intensifier. If a laser shot occurred during the 5 ms buffer period, then the camera trigger was postponed until the following shot. Having received the camera trigger signal, the intensifier was gated to coincide with the laser shot. A single kerosene PLIF image was thus acquired at a random point between 5 and 105 ms following every spark.

In addition to fuel images, recordings of flame development were acquired during ignition testing. At the unsafe condition the high-speed camera was triggered by the spark and flame control box on detection of the first spark. The pre-trigger interval of the camera was set to 8.8 ms. This period represented 0.5% of the total recording period available during a single ignition test (1.90 s). As the sparks were separated by roughly 750 ms, this pre-trigger interval was sufficient to ensure that the high-speed imaging at the unsafe set point captured the first three ignition attempts.

Spark and flame luminosity were also monitored by an Agilent HSDL-5420 infrared photodiode mounted outside the ATF, adjacent to the external window. Using the spark trigger produced by the spark and flame control box as a reference signal, the current probe and photodiode outputs were recorded throughout the period from 10 ms before to 110 ms following each spark. In addition to these signals, the spark, flame, and camera trigger pulses were also recorded during this interval.

#### **3.4.4 Fuel and flame imaging at safe condition**

The data acquisition process employed during safe ignition testing was broadly similar to that used when operating at the unsafe set point. Indeed, the PLIF imaging system functioned exactly as described in Section 3.4.3, generating a single fuel distribution image between 5 and 105 ms following every spark. The current probe, photodiode and trigger signals were also recorded from 10 ms before to 110 ms following each spark. However, in contrast to the unsafe operation mode, where the flame imaging began following the first spark, at the safe condition the high-speed camera was triggered following the detection of a successful flame. Additional flame detection hardware was necessary to achieve this, and the full functionality of the system illustrated in Figure 3.13 was required.

The camera trigger was generated by the spark and flame control box, which monitored the photodiode signal throughout each ignition test. If the amplified signal from this photodiode (see Figure 3.14(c)) exceeded a threshold of 2.5 V at any time between 15 and 100 ms following the detection of a spark, then a flame trigger was generated (see Figure 3.14(d)), and directed to the high-speed flame camera. The pre-trigger interval of the flame camera was set to 1.43 s during testing at the safe condition. This period represented 75% of the total recording period available during a single ignition test. This enabled every safe successful ignition event to be recorded on the high-speed camera, together with each preceding unsuccessful attempt. As discussed in Section 3.1.2, successful ignition was consistently achieved

within fourteen sparks at the safe condition. Data acquisition therefore continued until a flame was detected, whereupon the high-speed camera was triggered and the test terminated.

### 3.4.5 Test numbers

Table 3.3 lists the number of successful and unsuccessful high-speed recordings of flame development acquired at the two test conditions. One hundred safe tests were conducted, recording the successful ignition event and any preceding failed development. However, six tests identified as successful by the flame detection hardware, failed to recover and survived for only a short period. These tests were therefore reclassified as unsuccessful. A further five safe tests were successful on the first spark. Thirty one unsafe tests were conducted, recording three unsuccessful ignition events during each test.

Table 3.3: Number of tests recorded with high-speed flame camera.

	safe	unsafe
successful	94	–
unsuccessful	101	93

The PLIF image numbers recorded are listed in Table 3.4. The ignition categories contain only those images that were acquired at the same time as a high-speed flame recording. One and four tests at the safe and unsafe test points respectively were discarded due to poor quality results.

Table 3.4: Number of tests recorded with PLIF camera.

	safe	unsafe
fuel only	200	200
successful ignition	93	–
unsuccessful ignition	100	81

# Chapter 4

## Results I: Preliminary Analysis

The previous chapter discussed the design requirements and development of apparatus to perform specific measurements under a set of well-controlled conditions. The success or failure of ignition is influenced not only by the random nature of the relight process, but also by spark-to-spark variations in the experimental boundary conditions. This chapter describes the measurement of these boundary conditions and compares them to the expected values. For instance, the test facility operating conditions, laser energy, and spark parameters all fluctuate during testing, and these variations must be quantified to assess their impact on the results presented in later chapters. In addition, the detailed analysis of PLIF images in Chapter 5 requires the timescales of flame development to be identified, as also described here.

### 4.1 Operating conditions

The combustor operating conditions were recorded once during every test, prior to the first spark. The measured parameters were air and fuel temperature and mass flow rate, together with air pressure. The test-to-test variations in these conditions are presented in Table 4.1. The mean temperatures and pressure correspond closely to their set point values, and the standard deviation of each variable is comparatively

small. Though not listed, this is also true for the air mass flow rate. These parameters were therefore well controlled throughout testing. However, a malfunctioning flow controller caused significant fluctuations in the fuel mass flow rate, leading to imprecise control of the total AFR. This is demonstrated by the relatively large standard deviation in the total AFR; approximately 4% of the mean at both conditions. Despite this poor fuel metering, the air mass flow rate at the two set points is sufficiently different to ensure that these fluctuations never transform the global test conditions from safe to unsafe or vice versa.

Table 4.1: Experimental operating conditions during ignition testing.

	safe			unsafe		
	set point	mean	std. dev.	set point	mean	std. dev.
$T_{\text{air}}$ (K)	265.0	265.4	0.3	265.0	265.1	0.3
$P_{\text{air}}$ (kPa)	41.4	39.8	0.2	41.4	43.9	0.4
$T_{\text{fuel}}$ (K)	288.0	286.6	1.8	288.0	287.9	0.7
total AFR	33.0	33.8	1.5	60.5	60.5	2.6

Since the air and fuel mass flow rates were recorded only once at the start of each ignition test, the sample rate was inadequate to reveal any possible correlation between AFR variations and ignition outcome. Continuous monitoring of AFR would therefore be desirable in future work.

## 4.2 Properties of laser beam and sheet

The following section describes two preliminary experiments to characterise the laser beam and sheet, conducted as preparatory work prior to PLIF imaging during ignition testing. Imaging of the beam passing through a fluorescent dye quantified laser energy fluctuations, while also providing spatial profile information. A slit-traverse experiment was conducted to corroborate the dye fluorescence results. The

revealed features of the beam energy distribution significantly influence the PLIF image correction discussed in Section 5.2.

### 4.2.1 Dye fluorescence

The method described by Arnold et al. (1997) and Hartung et al. (2008) for measuring the laser profile by projecting the beam through a dye has been followed here. Images of the dye fluorescence provide information about the shot-to-shot fluctuations and the spatial profile of the beam. Due to restricted access in and around the ATF however, it was not possible to image the energy profile during ignition testing. A supplementary laboratory experiment was therefore performed, as described below.

A quartz cell with internal dimensions  $10\text{ mm} \times 10\text{ mm} \times 44\text{ mm}$ , was filled with a fluorescent dye solution, and positioned in front of the laser aperture. The intensified camera used for kerosene PLIF imaging was positioned to view the dye cell from beneath. The laser energy was adjusted to that used during ignition testing and PLIF images of the fluorescing dye were recorded. A sample image is shown in Figure 4.1(a).

While a smooth variation in intensity might be expected, the horizontal striations apparent in Figure 4.1(a) reveal significant irregularities in the beam profile. In addition, air bubbles in the dye solution have caused distinct spots in the image. The signal along the indicated mid-plane of the cuvette has been extracted from 110 individual images, and these profiles are plotted in Figure 4.1(b), together with the mean. The observed irregularities in the mean are partly attributable to these air pockets.

Shot-to-shot variations in laser energy produced significant scatter in the fluorescence profiles. For a sample of 110 images, the standard deviation close to the centre (i.e.  $l \approx 5\text{ mm}$ ) represents approximately 8% of the mean signal. Consequently, as the energy evidently varies from shot to shot, individual PLIF images recorded dur-

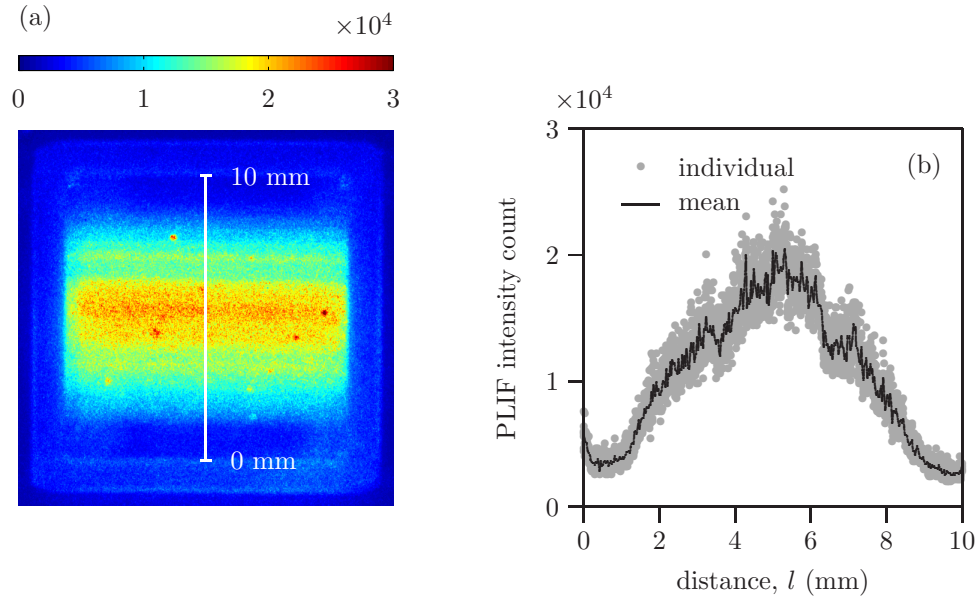


Fig. 4.1: Dye fluorescence measurements of beam energy profile: (a) typical single-shot image; (b) 110 mid-plane profiles and their mean.

ing altitude testing cannot be compared directly. However, comparison of safe and unsafe mean images is justified, as the laser fluctuations are not influenced by the test conditions and the sample size of PLIF images is large.

The spatial energy profile deviates significantly from the expected Gaussian distribution. Though the signal is noisy, two distinct shoulders in the mean profile are apparent at  $l \approx 3.0$  mm and  $l \approx 7.0$  mm. This observation has important consequences for the fuel imaging experiment that are examined thoroughly in Section 5.2. It is clear from Figure 4.1 that a correction for the beam energy distribution must be based on a measured, rather than an assumed, energy profile.

#### 4.2.2 Slit traverse

The spatial energy distribution generated by a laser can also be characterised by measuring the power transmitted through a narrow slit as it scans across the beam (Su and Clemens 1999; Hornak 2002). In the current study, a 0.55 mm vertical slit

was created using two razor blades. These blades were mounted in front of a laser power sensor, and this assembly was traversed across the laser beam and sheet.

During the beam traverse, the slit was positioned 200 mm from the laser aperture. With the laser generating the same energy as used during ignition testing, the slit assembly was scanned across the beam incrementally, noting the transmitted power after each positional adjustment. The slit assembly was similarly traversed across the laser sheet. A laboratory mock-up of the optical arrangement used during rig testing was constructed to recreate the sheet.

Figure 4.2 illustrates the rate of change of power with traverse distance through the beam and sheet. These profiles were constructed as follows. The power sensor readings noted during each traverse were plotted cumulatively as a function of distance. These profiles were then differentiated numerically, applying a least-squares smoothing filter to remove low level fluctuations (Press et al. 2007). Note that it is difficult to identify the centre of the measured energy distributions due to the asymmetry of the profiles. For convenience, the central peaks have been aligned in Figure 4.2.

The plot of beam power gradient confirms that the beam diameter is approximately 8 mm. As observed in the dye fluorescence images, the beam profile departs significantly from a Gaussian distribution, with two shoulders located at  $l \approx -2.5$  mm and  $l \approx 1.5$  mm relative to the central maximum. Since the beam exits the laser head and strikes the slit directly, these shoulders are not caused by contaminated or damaged optics located beyond the harmonic separators. The extent of the sheet could not be identified due to the inadequate thermal sensitivity of the power sensor. The beam and sheet profiles do, however, appear qualitatively similar, confirming that the sheet energy distribution can be represented by linearly scaling the beam profile.

The dye fluorescence and slit traverse profiles are in good agreement and the non-uniformities in the beam profile are well characterised by both. However, air bubbles

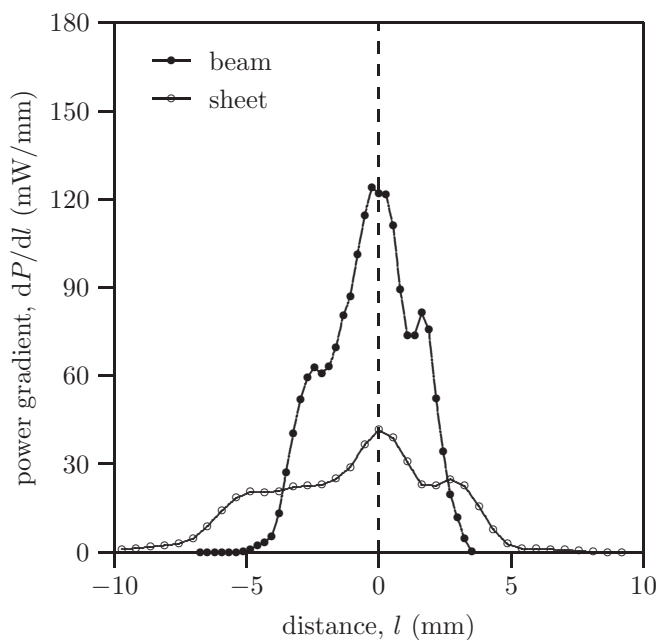


Fig. 4.2: Slit traverse measurements of beam and sheet energy profiles.

in the dye solution adversely affect the dye fluorescence results (see Section 4.2.1), and the slit traverse measurements of the beam are therefore considered to be more accurate. A scaled form of this beam profile is therefore used to correct the kerosene PLIF images for non-uniformities in the laser sheet (see Section 5.2.4).

### 4.3 Characteristic times

Preliminary analysis of the high-speed film was conducted to characterise the timescales of ignition success and failure. These timescales are used to classify every PLIF image according to the development stage of the flame at the instant of acquisition.

#### 4.3.1 Recovery and failure times

The total intensity variation measured in each high-speed recording provides a simple assessment of combustion activity during ignition. This section describes the results of a straightforward total-intensity analysis, and considers the distribution

of characteristic timescales identified from these intensity data. Further information can be extracted from the high-speed images using the more sophisticated analysis described in Chapter 6.

The total intensity traces plotted in Figure 4.3 are typical examples of ignition success and failure. The high-intensity initial signal due to the spark decreases to a low level within approximately 5 ms. This large reduction in flame emission has been observed in previous gas turbine ignition studies (Naegeli and Dodge 1991; Pucher et al. 2001). During the low-intensity delay period before recovery or failure, the successful and unsuccessful plots are indistinguishable, and flames that later grow and develop successfully emit very little light at this point. Indeed, during 6 of the 94 successful recordings, the flame emissions are so weak that the camera registers no signal whatsoever. These ‘false failures’ typically occur for a period of less than 1 ms, and result from either a dramatic reduction in flame volume, or a shift in the emission wavelength to beyond the detection range of the imaging system (see Figure 3.11 for the spectral sensitivity of the high-speed camera).

If the total intensity plots of different successful events are compared, the height of the recovery maximum can be seen to vary significantly from test to test, reflecting differences in the initial mass of fuel in the combustor. After this excess fuel has been consumed, the intensity falls to a much lower value that is broadly the same for all successful tests.

The failure and recovery times used to characterise each test outcome, and frequently referred to below, are also illustrated in Figure 4.3. The failure time is defined as the interval between the spark and the last frame containing any flame activity. The recovery time is the period following the spark when the signal first increases to exceed a selected threshold value of  $1 \times 10^6$  counts (see dashed line in Figure 4.3). The intensity count never exceeds this value during a failure, but always recovers strongly having exceeded it during a successful attempt.

The characteristic times of every ignition event are compiled in Figure 4.4. This

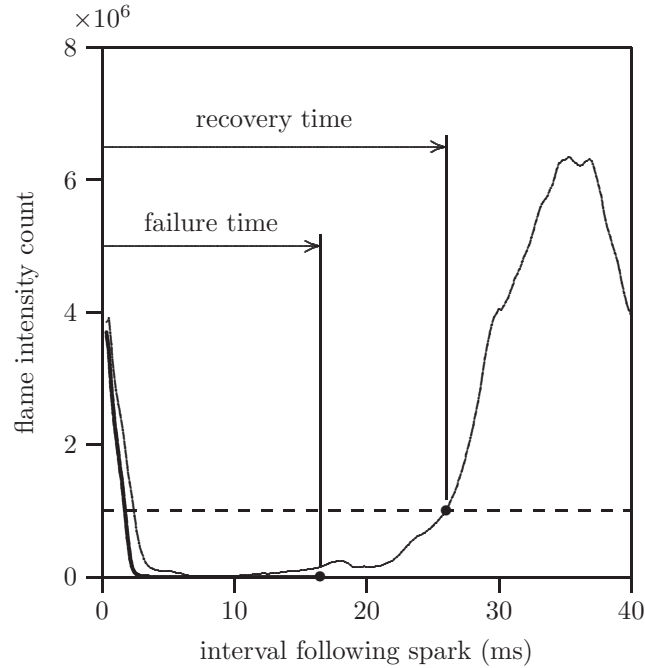


Fig. 4.3: Definition of recovery and failure times.

plot illustrates the proportion of unsuccessful tests that are yet to fail (red and blue lines), and the fraction of successful tests that have already recovered (green line). For a given condition and outcome, the range of recovery and failure times is large compared to the mean. This is particularly true during successful events, when the low-intensity phase before recovery can be as short as 10 ms, or can persist for a period of up to 69 ms. This suggests that recovery is a random event not strictly correlated with the operating conditions at the instant of the spark.

It is clear from Figure 4.4 that failures occur faster at the unsafe condition than at the safe point. Indeed, 67% of unsafe failures occur before the first safe death. Although the cumulative failure curves have similar profiles in Figure 4.4, the flame development process is visually different for safe and unsafe failures. When viewed directly, the sequence of high-speed images indicates that unsafe failures result from disintegration of the flame kernel, whereas safe failures generally occur following significant flame propagation. These two modes of failure have also been

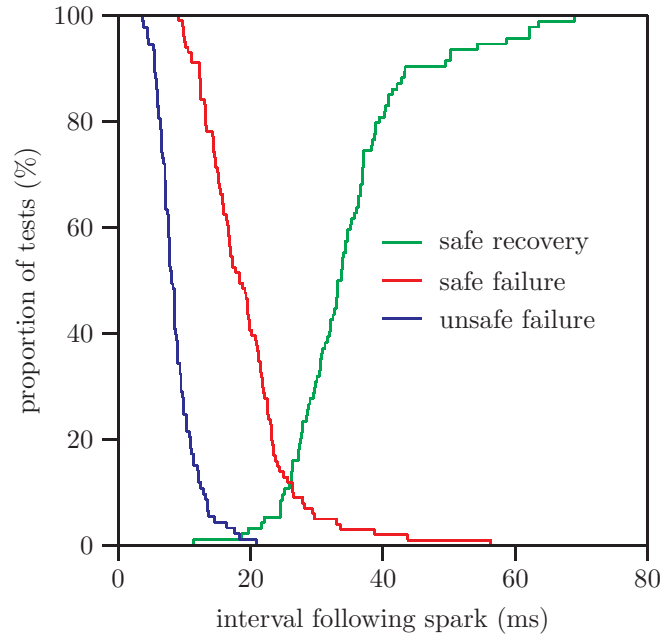


Fig. 4.4: Cumulative frequency plot of recovery and failure times.

observed during ignition studies of laboratory-scale flames (Ahmed et al. 2007a). This important observation is explored further in Section 6.2.

### 4.3.2 Classification of PLIF images

Having extracted recovery and failure times from every high-speed flame recording, the kerosene PLIF images can be categorised according to the state of flame development at the instant of image acquisition. As the timing of the laser pulse relative to the spark could not be controlled, every PLIF image was acquired at a random interval between 5 and 105 ms following the spark (see Section 3.4). By recording this spark-image interval, and comparing it to the corresponding recovery or failure time, it is possible to determine the state of flame development when each PLIF image was acquired, as shown in Table 4.2.

Images recorded before recovery or failure are categorised as ‘developing flame’. These images were acquired when the flame was confined to small regions of the

Table 4.2: Classification of PLIF images.

		safe	unsafe
successful	{ developing flame	24	–
	{ stabilised flame	69	–
unsuccessful	{ developing flame	13	0
	{ post-failure	87	81

combustor, with unburnt fuel often present in the laser sheet. During ignition recovery, flame expands to occupy the majority of the combustor volume, consuming most of the imaged fuel. The PLIF images acquired under these conditions were grouped into a ‘stabilised flame’ category. The influence of flame on the fuel PLIF signal is examined in more detail in Section 5.1.3.

Observe that in Table 4.2 there are relatively few PLIF images of developing flame at the safe condition, and none at the unsafe condition. This is due to the short timescales of success and failure compared to the 100 ms range of spark-image intervals (see Figure 4.4). For future work, the number of developing flame PLIF images could be increased either by providing control of the spark-image interval, or by greatly increasing the total number of tests.

Although the acquisition timing limited the number of images acquired during flame development, a comparatively large number of stabilised flame and post-failure images were generated. By definition the post-failure shots were acquired in the presence of fuel alone, and therefore increase the number of cold, fuel images from 200 (see Table 3.4), to 287 and 281 at the safe and unsafe conditions respectively. These images have been included in the total fuel-only sample analysed in Chapter 5.

## 4.4 Spark effects

The ignition system used for relight testing is rated to deliver 10 J of energy per spark. Minimum ignition energies at least ten times smaller than this have been

recorded during laboratory-scale ignition studies of kerosene-air sprays generated under altitude conditions (see Table 2.3). Despite the comparatively large quantity of energy deposited in the combustion chamber during the present study, only 17% of sparks lead to a fully-stabilised flame. As highlighted in Section 4.3, there is generally an extended period between the spark and the onset of recovery, providing ample time for variations in the flow field and fuel distribution to completely extinguish the flame. This explains the low observed success rate.

A high-speed image of the spark acquired 0.35 ms following the discharge is illustrated in Figure 4.5. The large amount of energy deposited by the spark is demonstrated by the well-defined saturated region around the igniter tip. Furthermore, the light emitted by the spark is sufficiently intense to illuminate the injector face, and to generate a strong reflection in the far-side combustor wall.

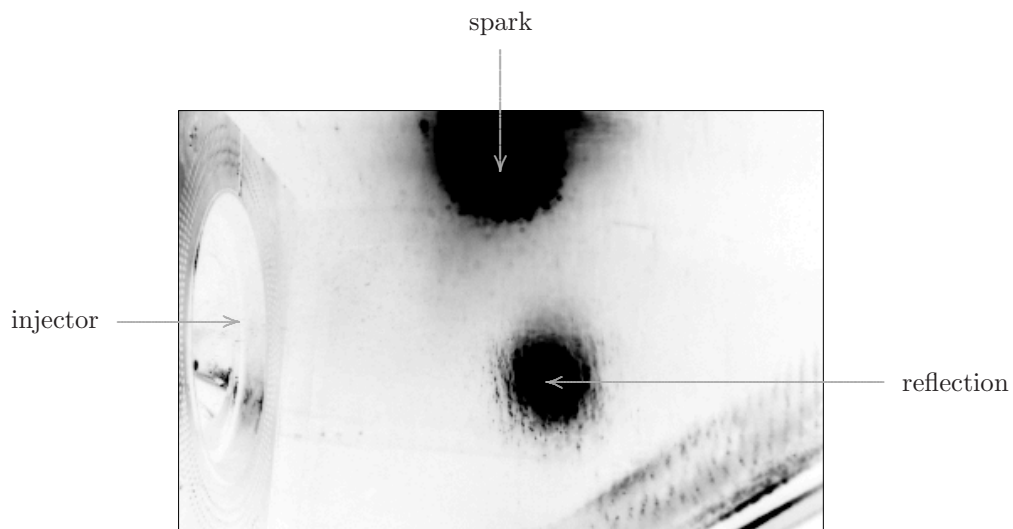


Fig. 4.5: Image of spark discharge. The colour map has been inverted so that black corresponds to the highest intensity.

### 4.4.1 Measured spark parameters

As noted in Section 2.2.2, the extent to which relight outcome is determined by the spark has not been previously investigated. Furthermore, fundamental studies of droplet ignition suggest that in addition to energy, other characteristics of the spark also affect the likelihood of success (see Section 2.4). This section therefore considers the influence of three spark parameters on relight outcome: size, current, and luminosity. The first of these is extracted from the high-speed images, while the second and third are measured directly. The area of saturated signal below the igniter tip in high-speed images of the spark (see Figure 4.5), provides a convenient measure of the spark size.

Assuming that the discharge voltage remains approximately constant, the spark current provides an indication of the energy introduced into the combustion chamber. Throughout testing, the current was recorded by an inductive probe mounted on the igniter lead. Electromagnetic shielding around the cable massively attenuated the measured signal however, generating data that is quantitatively inaccurate. Despite this, the results provide a useful comparative measure of spark current, and in turn, energy.

A further source of spark information was provided by the photodiode. Though introduced for control purposes, the peak voltage generated by the photodiode reveals variations in the spark luminosity. In contrast to the high-speed camera, the photodiode did not saturate when exposed to the intense spark emissions, and thus provides a reliable measure of spark brightness.

Figure 4.6 illustrates the distributions of measured spark size, peak current, and peak luminosity, grouped according to set point and ignition outcome. The measured spark size (see Figure 4.6(a)) has been extracted from every high-speed sequence, yielding an approximately equal number of samples for each histogram, as indicated previously in Table 3.3. In contrast, Figures 4.6(b) and 4.6(c) present measurements recorded during a much larger number of sparks. In these figures,

the relatively small number of safe successes (green line), reflects the low ignition probability.

Accounting for the differences in sample size, the distributions do not differ significantly with set point or ignition outcome. This observation is reinforced by the closely matched mean and standard deviation of each spark parameter, presented in Tables 4.3 and 4.4 respectively. These results therefore imply that the measured variations in spark size, current, and luminosity do not influence ignition outcome, and are not significantly affected by the test conditions.

Table 4.3: Mean measured spark parameters.

	kernel area ( $\times 10^3$ pixels)	peak attenuated current (A)	peak photodiode output (V)
safe success	5.77	21.4	4.51
safe failure	6.19	21.4	4.52
unsafe failure	6.25	21.6	4.50

Table 4.4: Standard deviation of measured spark parameters. The standard deviation as a percentage of the mean is included in parentheses.

	kernel area ( $\times 10^3$ pixels)	peak attenuated current (A)	peak photodiode output (V)
safe success	0.87 (15%)	1.63 (8%)	0.04 (1%)
safe failure	1.16 (19%)	1.74 (8%)	0.05 (1%)
unsafe failure	1.85 (30%)	1.63 (8%)	0.04 (1%)

The spark variability can be assessed from the standard deviation of each data set (see Table 4.4). While the peak attenuated current and photodiode output are both tightly grouped around their mean values, the scatter in the kernel area is relatively large. The spread in this data is partly associated with the limited recording rate of the high-speed camera. The finite exposure period causes the time between the spark discharge and the analysed frame to fluctuate by  $\pm 88 \mu\text{s}$  from spark to spark.

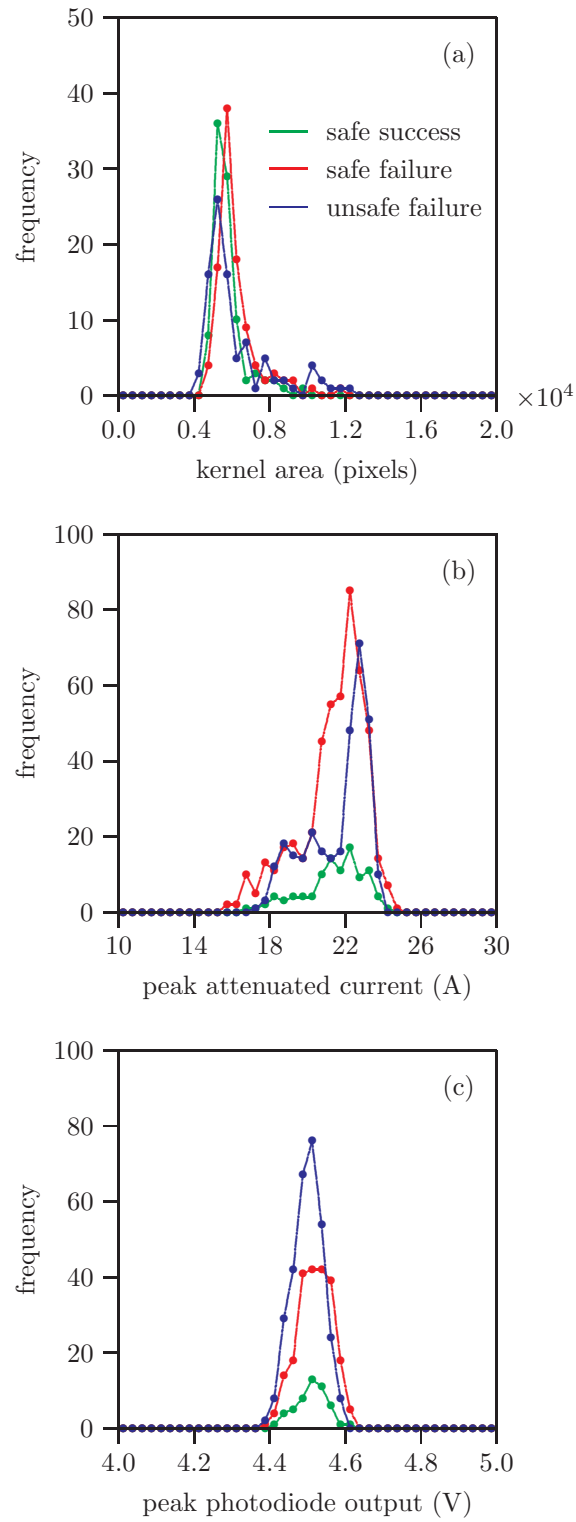


Fig. 4.6: Histograms of measured spark parameters: (a) size; (b) current; (c) luminosity.

This generates scatter in the spark size measurement, as the initial kernel growth is rapid and not temporally resolved by the camera. As the standard deviation in the kernel area is exaggerated by the frame timing, the spark appears to be relatively consistent.

#### 4.4.2 Interaction between successive sparks

A single ignition test at the safe condition consisted of repeated sparking at 750 ms intervals until a successful developing flame was detected by the photodiode. The spark-to-spark interval significantly exceeds both the combustion chamber residence time (24 ms and 13 ms at the safe and unsafe set points respectively), and the longest recorded recovery time (69 ms). The hot gases and chemical radicals produced during an unsuccessful ignition attempt have therefore been evacuated from the combustor well before the next spark. While this might lead us to expect every spark to have a constant probability of success, the distribution of safe, successful spark numbers illustrated in Figure 4.7, provides evidence to the contrary.

If sparks are independent, then the probability of success on the  $k$ -th spark is analogous to the probability of tossing a coin and obtaining  $k - 1$  tails before achieving a head. Therefore, the probability is given by

$$P(k) = (1 - p)^{k-1}p \quad \text{where } k = 1, 2, 3, \dots, \quad (4.1)$$

where  $p$  is the probability of any spark being successful. This is known as a geometric distribution (Papoulis and Pillai 2002). The expected number of successes on the  $k$ -th spark for a sample of  $N_{\text{tot}}$  ignition tests is then  $N_{\text{tot}}P(k)$ . Unlike the coin flipping example, where  $p = 0.5$ , the probability of individual spark success is less than that of failure.

Assuming that the entire sample of ignition tests consists of independent sparks,  $p$  is estimated by the total number of successful sparks divided by the total spark

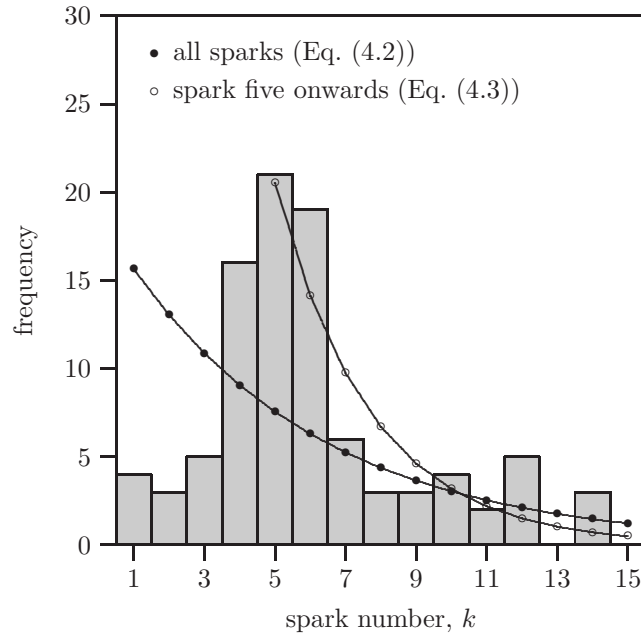


Fig. 4.7: Measured and expected distributions of successful spark number. The expected distribution is calculated using Eq. (4.1).

number

$$p = \frac{N_{\text{suc}}}{N_{\text{tot}}} = \frac{94}{565} = 0.17. \quad (4.2)$$

Substituting this value of  $p$  into Eq. (4.1) generates the distribution represented by filled circles in Figure 4.7. This distribution over-predicts the number of successes for low values of  $k$ . Furthermore, the increase in recorded successes from  $k = 1$  to  $k = 5$  indicates that, contrary to the predicted trend, the ignition probability is growing during these early sparks.

If the sample is instead restricted to tests where success occurs later than spark four, then  $p$  is given by

$$p = \frac{N_{\text{suc}}}{N_{\text{tot}}} = \frac{66}{212} = 0.31. \quad (4.3)$$

As illustrated by the open circles plotted in Figure 4.7, the distribution generated using this ignition probability, corresponds more closely to the measured data. This indicates that the ignition events are independent from spark five onwards, but not

before.

The early spark-number dependence may result from a change in the spark delivery system over time. As noted in Section 4.4.1, none of the measured spark parameters exhibit any correlation with outcome. However, the possibility remains that sparks could change in some way that has not been measured here. For example, discharge duration has previously been shown to affect the ignition outcome independently of spark energy (Ballal and Lefebvre 1975). In addition, variations in the breakdown voltage may cause spark losses to vary, producing fluctuations in the heat supplied.

Alternatively, repeated sparking may produce a change in operating conditions that favours later sparks. Such behaviour has been observed by Marchione et al. (2007, Sep). In their laboratory-scale experiment however, the interval between sparks was considerably shorter than the evacuation time of the combustion chamber. As highlighted above, the spark interval in the present study is more than adequate to ensure that air and fuel flows are unaffected by previous sparks. Nevertheless, a change in the boundary conditions could result from an accumulation of heat in the combustor walls caused by early sparks. While this possibility was further investigated by mounting a thermocouple immediately downstream of the igniter, no evidence of warming was found.

Despite this, the wall temperature measurements provide a key insight into the distribution of liquid fuel inside the combustor, and suggest an alternative explanation for weak early sparks. At the safe condition, the wall temperature was observed to increase when fuel injection commenced, indicating the impingement of fuel on the thermocouple. This suggests that a film of fuel may cover the igniter tip initially, before being dislodged or vapourised by early sparks. The presence of excessive fuel on a surface-discharge igniter tip is known to adversely affect spark performance (see Section 2.2.2).

For a quantitative study of the factors influencing ignition events per se, analysis

should be confined to the later, independent sparks. In the present study, however, a limited number of ignition tests were performed, and discarding data would reduce the sample size significantly. Furthermore, the increase in ignition probability during early sparks may occur in-flight, when attempting high-altitude restart. As a consequence, the modes of success and failure during the opening sparks are of considerable practical interest, and will be considered together with those of later sparks.

# Chapter 5

## Results II: Fuel Imaging

In this chapter individual and mean PLIF images are studied to identify differences in fuel placement at the two set points. Significant corrections must be applied to the raw images to account for the beam energy distribution and sheet geometry. To allow comparison of uncorrected PLIF images, analysis is initially restricted to a small region in the centre of the sheet. Entire images are later corrected and compared in Section 5.2. CFD flow predictions are considered, and the influence of the flow field on the fuel distribution is discussed.

### 5.1 Analysis of uncorrected PLIF images

#### 5.1.1 Individual cold images

Instantaneous images of fuel distribution acquired at the safe and unsafe test conditions are presented in Figures 5.1 and 5.2 respectively. Also shown in these figures is a detail from the centre of the laser sheet, denoted region A. Both images are representative, and have been selected so that the count inside region A is close to the mean at their respective set points.

Distinct droplets of various sizes are apparent in both Figures 5.1 and 5.2, together with lower intensity regions of cloudy, diffuse signal. These areas correspond

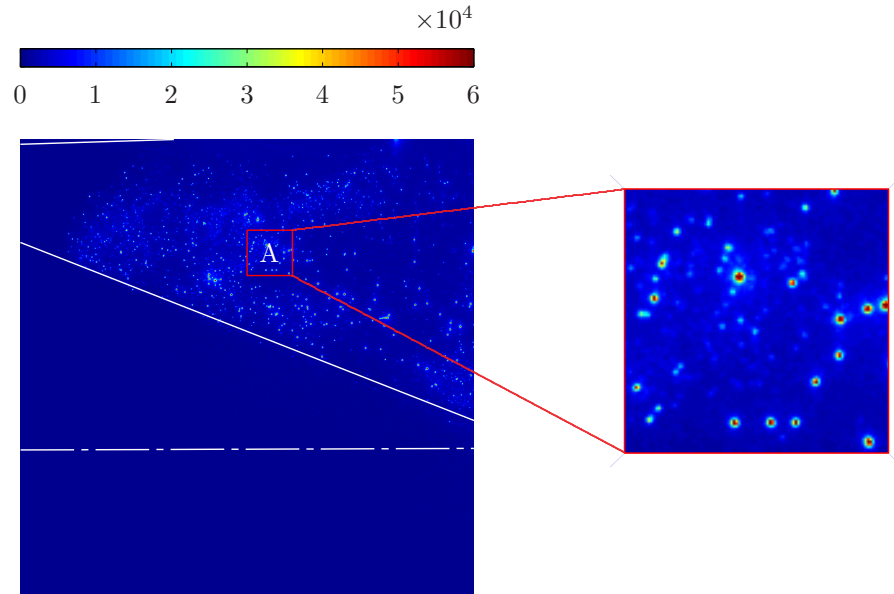


Fig. 5.1: Uncorrected, individual, cold PLIF image acquired at safe condition.

to fuel vapour and small droplets with diameters below the spatial resolution of the camera. The finite sheet thickness also makes it difficult to resolve clusters of sub-pixel mist.

From the detail images of typical ‘safe’ and ‘unsafe’ signal, it can be seen that though there are more droplets at the unsafe condition, the droplet sizes are similar in both cases. These observations are confirmed by Figure 5.3, which shows the five detail images with region A counts closest to the mean at each set point. Figure 5.4 has been produced by applying a logarithmic colour map to the detail images shown in Figure 5.3. The low-level signal revealed in Figure 5.4 suggests that the proportion of fuel contained in very small droplets and vapour is larger at the unsafe condition (particularly pronounced in sub-figures (g) and (h)), but that this signal represents only a small fraction of the total region A count. The range of droplet sizes evident in the detail images has been selected by the CRZ, which is expected to occupy the region below the igniter tip (see Section 2.1). Recirculating flows have the ability to select particle size as the inertia of large liquid droplets often causes them to deviate

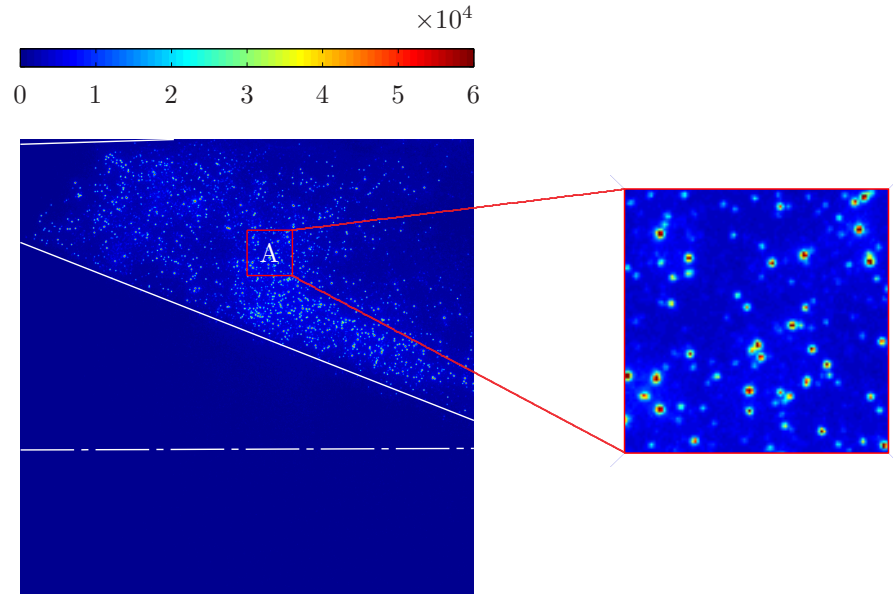


Fig. 5.2: Uncorrected, individual, cold PLIF image acquired at unsafe condition

from the streamline of the surrounding gas (Hardalupas et al. 1994; Becker and Hassa 2003). The observed uniformity of droplet sizes in region A suggests that the centrifugal effect of the recirculation vortices is similar at the two test conditions.

Figure 5.4 also confirms that the number density of droplets is larger at the unsafe condition. This is perhaps unexpected as the fuel flow rate is identical at both set points. However, the global distribution of droplet size is significantly different at the two set points as demonstrated by the back-lit images of cold atomised fuel presented in Figure 5.5. At the safe condition, where the air flow rate is relatively low (Figure 5.5(a)), a cone of large droplets can be seen emerging from the pilot injection point, whereas no large droplets are apparent at the unsafe set point where the air flow rate is relatively high (Figure 5.5(b)). The droplets generated at the unsafe condition are smaller due to the improved performance of air-blast atomisers at higher air flow rates (see Section 2.2.1). As noted above, the PLIF signal in region A is due to small droplets only. The momentum of the larger droplets carries them onto the internal surfaces of the combustor. Consequently, there is a high

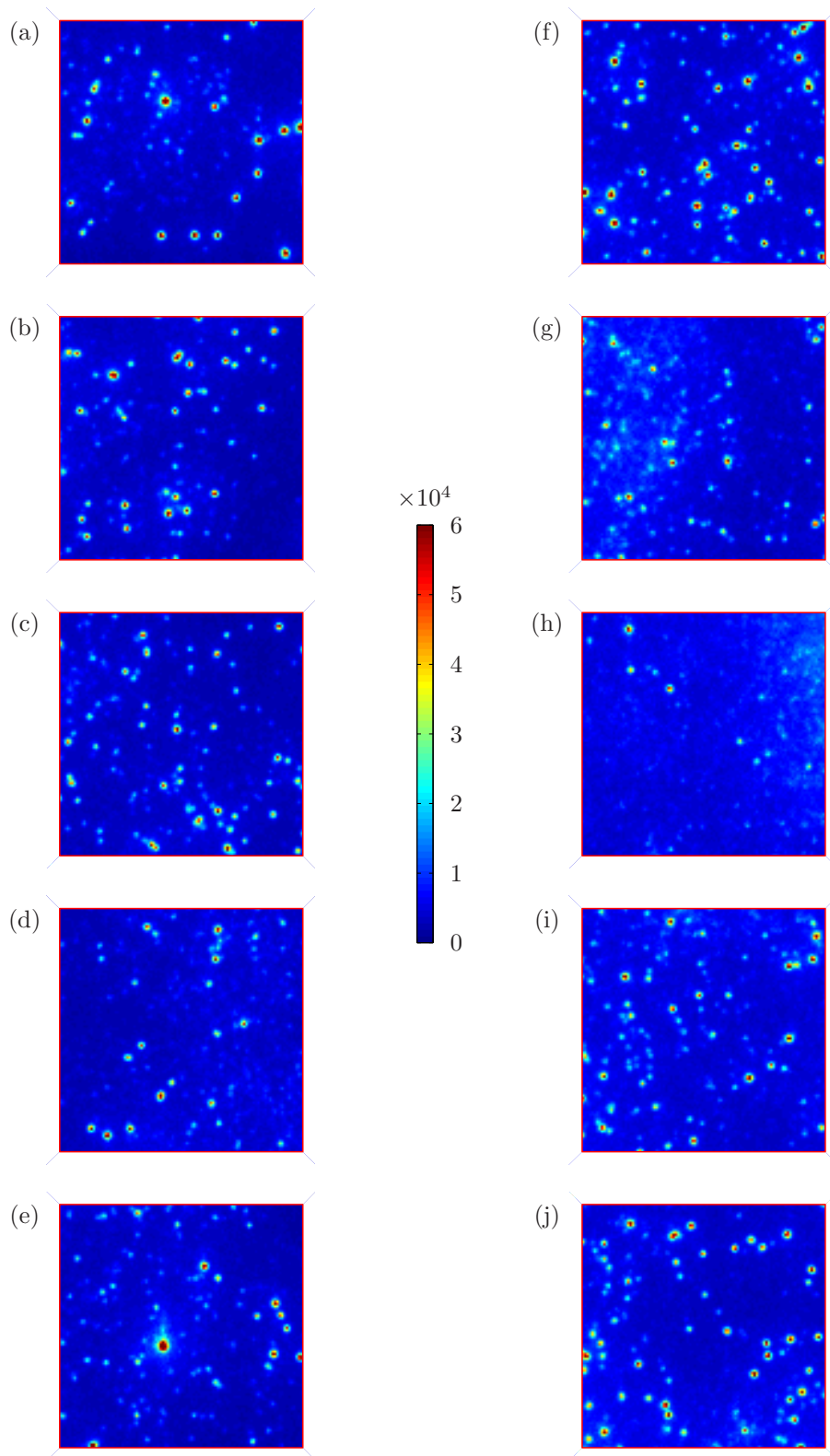


Fig. 5.3: Cold PLIF details: (a)-(e) safe condition; (f)-(j) unsafe condition

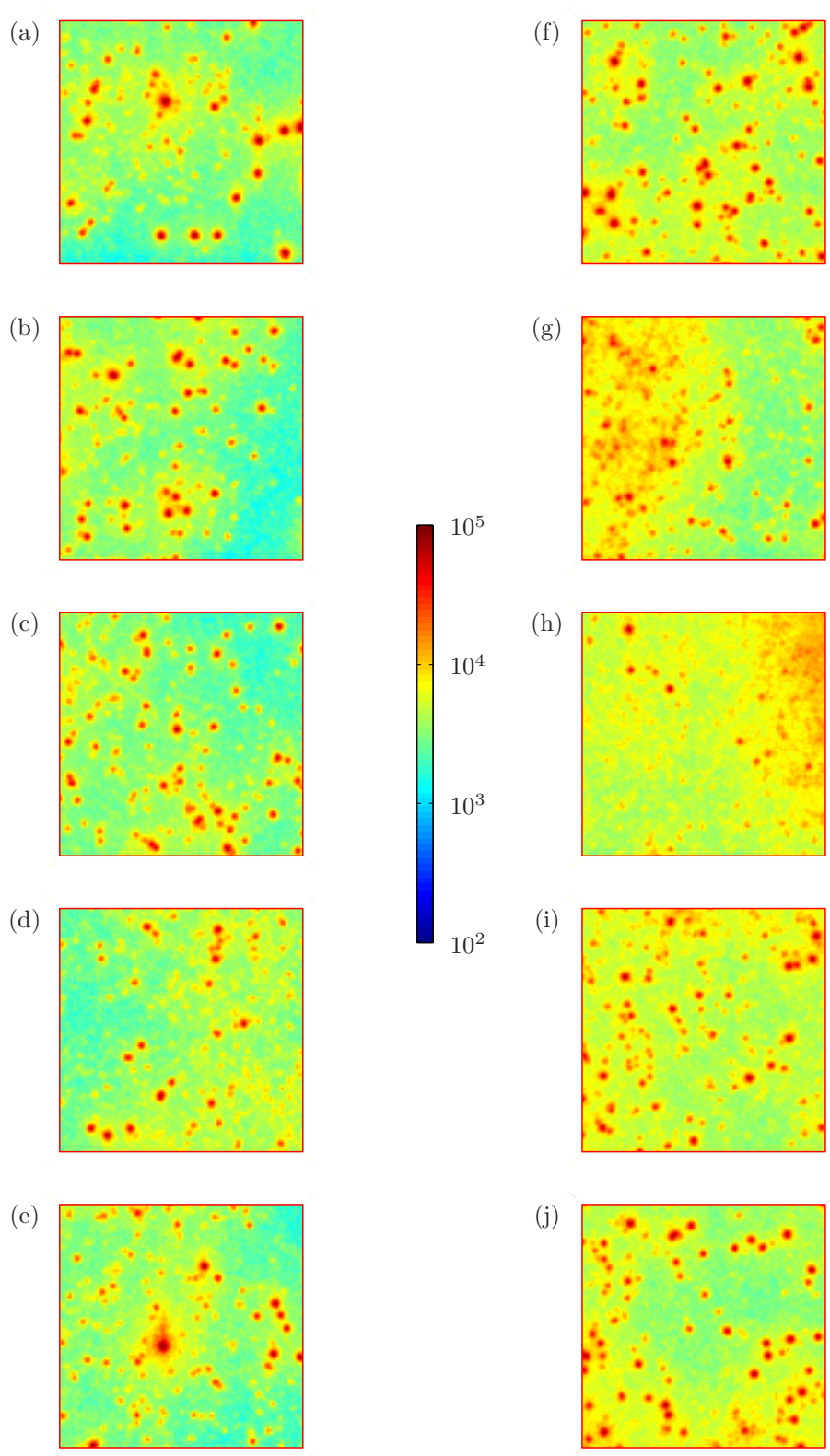


Fig. 5.4: Cold PLIF details with logarithmic scale: (a)-(e) safe condition; (f)-(j) unsafe condition

level of signal on the outside wall at the safe condition (as demonstrated in the next section), and a relatively low level of signal in region A. The opposite is true at the unsafe set point.

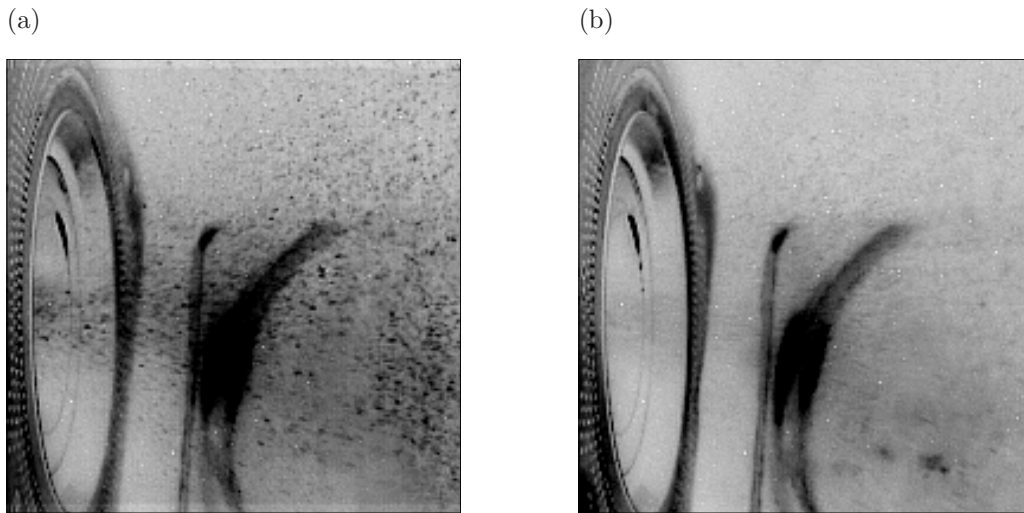


Fig. 5.5: High speed images of cold fuel droplets: (a) safe; (b) unsafe. The colour map has been inverted so that black corresponds to the highest intensity.

As the relative amounts of fuel deposited on the combustor walls and fuel in suspension are unknown, the local equivalence ratio in region A is not well represented by the global equivalence ratio. On the basis of the images presented above, the equivalence ratio below the igniter tip is higher at the unsafe condition than at the safe set point, despite the global equivalence ratio being much leaner at the unsafe condition (unsafe: 0.24, safe: 0.45). Relight is impossible at the unsafe condition, so the relatively high fuel signal can be interpreted in two ways: either the mixture strength is more favourable at the unsafe condition and failure is entirely due to turbulent strain, or the mixture is locally too rich for ignition to occur.

The possibility of a locally rich mixture can be evaluated from the PLIF images in Figure 5.4. These indicate that a rich mixture would be produced if the fuel contained in region A was fully vapourised by the spark. This could occur at both

test conditions, but would be more extreme at the unsafe set point since more fuel is present in the detail images at this condition. The lack of flame growth at the unsafe condition could therefore be caused by an equivalence ratio that is beyond the rich flammability limit. The combined effects of an unfavourably rich mixture in the CRZ and excessive turbulent strain are the most likely causes of ignition failure at the unsafe condition.

### 5.1.2 Mean cold images

Mean, cold images illustrating the average fluorescence signal recorded at the two test conditions are presented in Figure 5.6. With the exception of a CCD background subtraction, these images are uncorrected

$$\langle I_u \rangle = \frac{1}{N} \sum_{j=1}^N (I_j - B), \quad (5.1)$$

where  $I_j$  are the individual uncorrected images and  $B$  is the CCD background.

Figures 5.6(a) and 5.6(b) represent the average signal from 287 and 281 images acquired at the safe and unsafe test points respectively (see Section 4.3.2). The upper and lower extents of the sheet are identified by solid white lines. The fuel injector centre-line is also included. These features were mapped onto the image using information from a CAD model of the apparatus, together with the camera viewing angle correction described in Appendix A. Note that the imaged region extends from the fuel-injector face on the left to immediately downstream of the igniter on the right, as identified previously in Figure 3.6.

Though exaggerated by the colour map, the signal level is higher in Figure 5.6(b) than in Figure 5.6(a). This is consistent with the observations about the detailed images noted in Section 5.1.1 where it was shown that the number density of fuel droplets is higher at the unsafe condition. It is this higher number density of droplets that leads to overall higher signal levels in the mean unsafe image compared to the mean safe image.

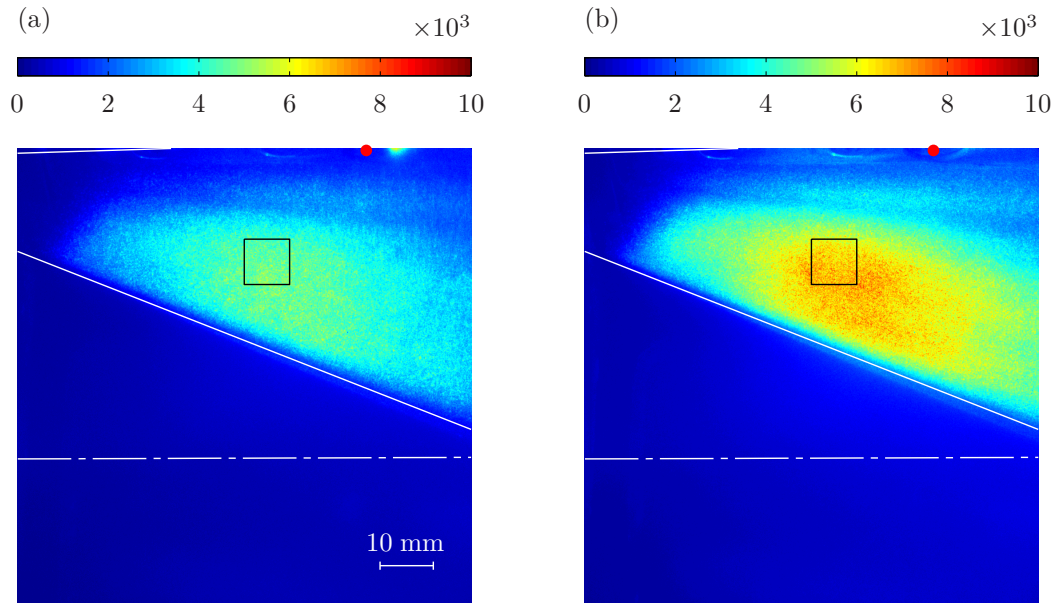


Fig. 5.6: Uncorrected, mean, cold PLIF images: (a) safe; (b) unsafe. The igniter tip is identified by a filled red circle. A black box is shown around region A.

The mean images illustrated in Figure 5.6 are qualitatively similar in several respects. The spatial distribution of fuel is broadly comparable at the two test conditions. In both cases, the recorded fluorescence originates principally from the bottom half of the excitation volume. The signal is relatively weak immediately beneath the combustor outside wall. Indeed, the intensity count is negligible in the upstream, outside corner of the chamber. A region of comparatively high intensity is apparent in both images, centred approximately 50 mm downstream from the fuel injector and 25 mm below the outside wall. The measured signal decreases both upstream and downstream of this region.

Fuel is introduced close to the injector centre-line. It is therefore credible that the comparatively low levels of fluorescence observed upstream accurately reflect an absence of fuel. This is, however, less likely downstream of the high-intensity region. The lower fluorescence intensity recorded at this location may have resulted from either attenuation of the excitation energy or a change in sheet cross-section.

Corrections for these factors are discussed below in Section 5.2.

In addition to these qualitative similarities, a further feature is also apparent in both images. A narrow band of low-intensity signal extends across the top half of the excitation volume. This dark stripe, particularly evident in the unsafe image, coincides with the path of an optical ray originating from the final lens, and was therefore initially attributed to lens contamination. As explained in Section 5.2.5 however, the stripe is an artefact of the non-Gaussian laser energy profile.

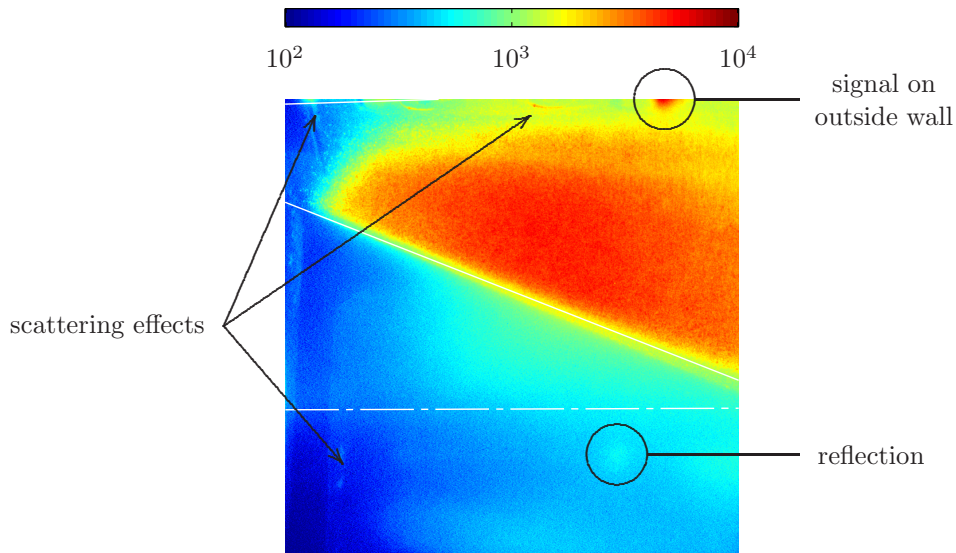


Fig. 5.7: Uncorrected, mean, cold PLIF image acquired at safe condition. Note the logarithmic intensity scale.

At the safe condition (see Figure 5.6(a)), a localised region of strong fluorescence is observed on the outside wall at the downstream edge of the igniter port. To highlight this low-level signal, the mean, safe image is reproduced in Figure 5.7 with the intensity colour map scaled logarithmically. The droplet signal downstream of the igniter is clearly visible. In addition, the reflection of this localised fluorescence can also be seen below the excitation volume. Though the wall signal and its reflection are also present at the unsafe condition, they are considerably weaker (see Figure 5.6(b)), indicating a difference in the quantity of fuel on the outside wall at

the two test conditions.

The mean, safe, cold image illustrated in Figure 5.7 contains clear evidence of scattering, as internal features of the combustion chamber are visible. This effect is largely associated with fuel contamination of the combustor walls. Liquid fuel residing on the internal surfaces not only fluoresces when excited by scattered laser light, but also reflects the fluorescent wavelengths.

The fluorescence count was extracted from a small region of every image to characterise the shot-to-shot distribution of fuel signal. The area of interest, identified as region A in Figure 5.1 and also outlined in Figure 5.6, is situated in the high-intensity region identified previously. As this area is comparatively small, the beam energy profile and sheet geometry corrections can be neglected. Histograms of the total region A intensity are plotted in Figure 5.8, and the sample mean and standard deviation at each test condition are listed in Table 5.1.

Table 5.1: Statistics of cold, total PLIF intensity in region A.

	mean ( $\times 10^8$ )	std. dev. ( $\times 10^8$ )
safe	0.50	0.23
unsafe	0.71	0.40

Significant image-to-image variation in the fuel signal is evident at the two test points. The large data spread ( $s/\bar{x} \approx 50\%$ ), in part results from variations in the bulk AFR ( $s/\bar{x} = 4\%$ ), and shot-to-shot fluctuations in the laser energy ( $s/\bar{x} = 4\%$ ). Since the combination of these factors accounts for only a small proportion of the variation seen in Table 5.1, the flow field is evidently fluctuating strongly.

As noted previously, the mean intensity is higher at the unsafe condition. The sample standard deviation is also larger at the unsafe condition. Since the AFR and laser energy fluctuations are the same in both cases, the difference between the standard deviations is due to higher rms turbulence levels at the unsafe condition.

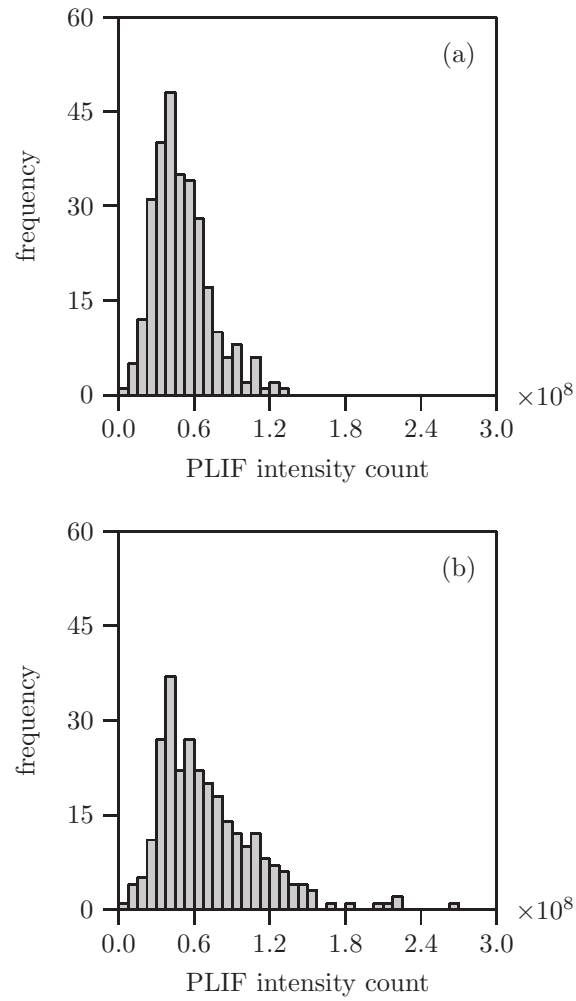


Fig. 5.8: Histograms of cold PLIF signal in region A: (a) safe; (b) unsafe. Note that region A is identified in Figure 5.1.

### 5.1.3 Influence of flame

In addition to the numerous images of cold fuel, 106 kerosene fluorescence images were acquired in the presence of developing and stabilised flame. The flame emission image acquired at the same instant as each fuel fluorescence shot has been extracted from the high-speed flame recordings. The bounds of region A can be transformed from the PLIF image to the corresponding high-speed image using the method described in Appendix A. The effect of flame on the fuel signal is illustrated in Figure 5.9, where the corresponding PLIF and flame intensities contained in region A are plotted.

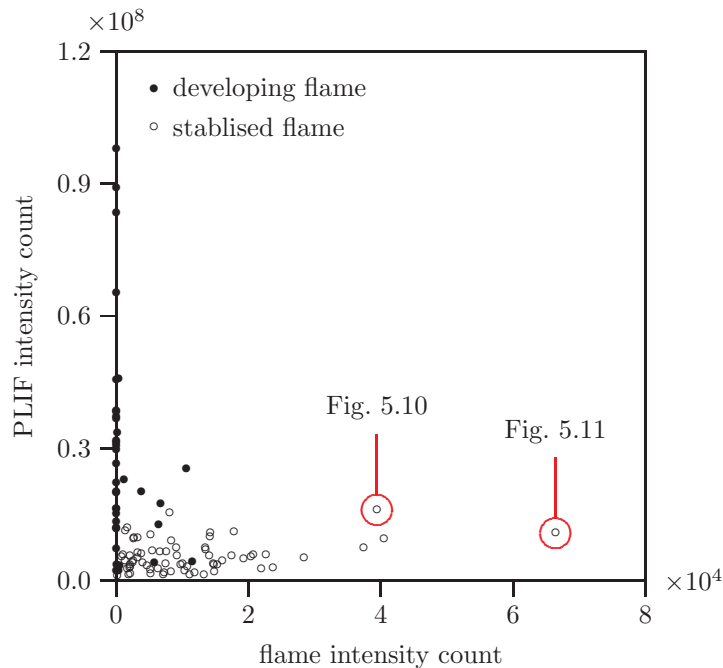


Fig. 5.9: Scatter plot of PLIF intensity versus flame intensity.

When no flame is apparent in region A, the fluorescence intensity count has a distribution broadly corresponding to that observed for the cold images. The mean intensity count is  $0.41 \times 10^8$ , compared to  $0.50 \times 10^8$  for fuel alone. When flame is detected in region A, the fluorescence count is significantly lower, with a mean of  $0.08 \times 10^8$ . Once flame is detected, the fuel signal is also largely independent of the

recorded flame intensity.

For similar levels of detected flame, the fluorescence signal recorded during flame development (filled circles in Figure 5.9), is generally larger than that measured following stabilisation (open circles). The reason for this is that stabilised flame occupies the entire combustor, whereas developing flame apparent in region A may lie outside the plane of the laser sheet. In this case the PLIF signal is elevated due to the presence of unburnt fuel.

Two pairs of simultaneous shots have been selected for closer examination. These are circled in Figure 5.9, and are displayed in Figures 5.10 and 5.11. Note that it was not possible to acquire perfectly simultaneous images due to uncertainties in the spark discharge timing. However, the maximum offset of the camera exposure periods never exceeded 88  $\mu\text{s}$ .

In Figure 5.10, flame has consumed the regions of fuel vapour and small droplets evident in the cold images (cf. Figure 5.1), significantly reducing the global signal. In the enlarged details of region A, significant flame activity is apparent, causing the consumption of all but three large fuel droplets.

Each of these droplets is surrounded by a low-intensity halo which may result from fluorescence of intermediate combustion products, such as polycyclic aromatic hydrocarbons (PAH). Such compounds are known to fluoresce in the near ultraviolet and blue regions of the electromagnetic spectrum (Ciajolo et al. 2001; Ossler et al. 2001). Alternatively, this signal may derive from flame interference. As discussed in Section 3.3.1, excited radicals produce emissions within the sensitivity range of the intensified camera (300 to 480 nm). However, the highly non-premixed nature of the flame suggests that radiative emissions from soot may interfere with the fuel fluorescence signal most strongly, even at these comparatively short wavelengths (Seyfried et al. 2007).

Despite the intense flame signal in Figure 5.10, little interference is apparent in the fuel fluorescence image. This is also true in the example of exceptionally high

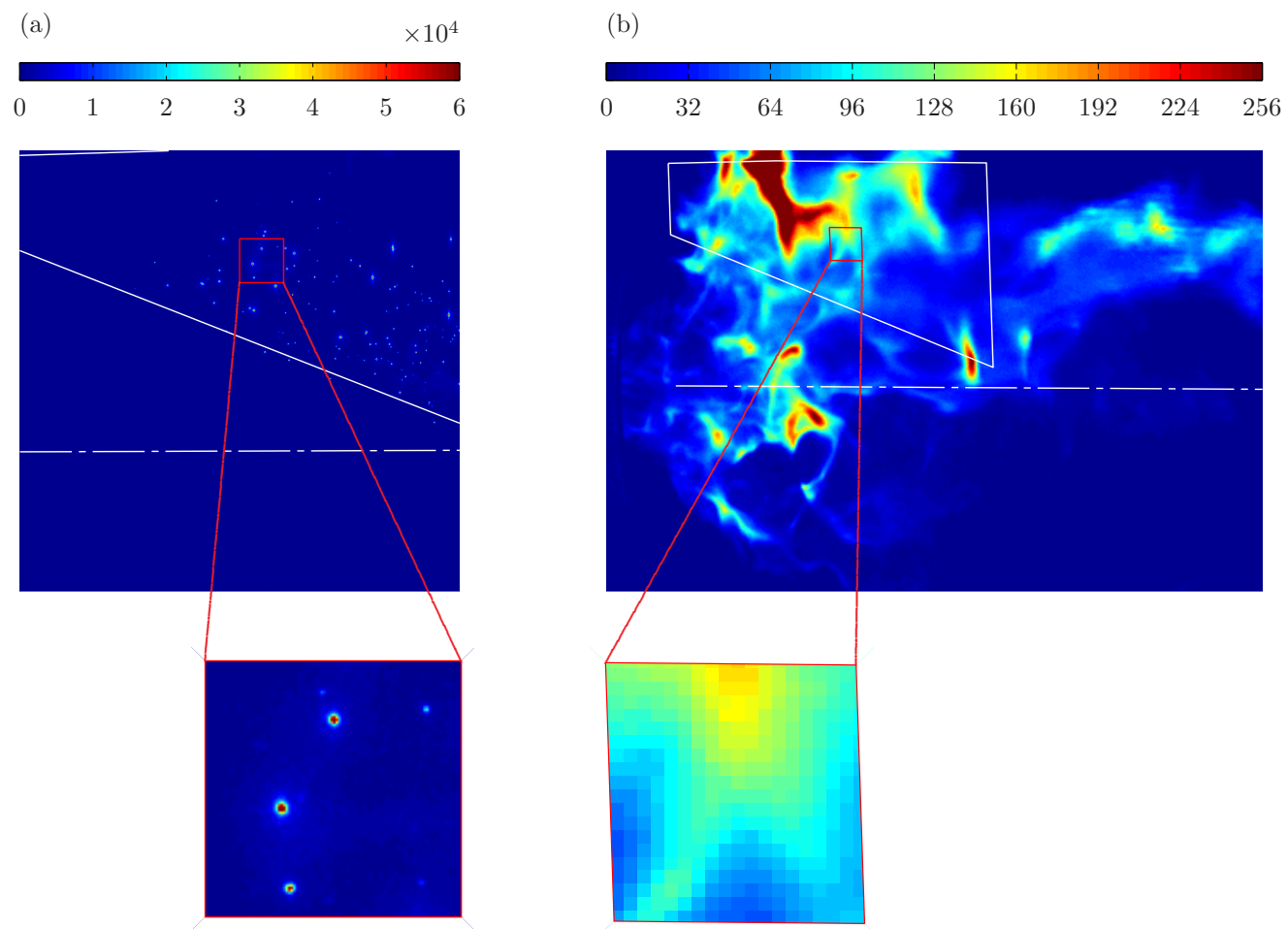


Fig. 5.10: Simultaneous images of fuel and flame: (a) uncorrected hot PLIF image; (b) flame emission image.

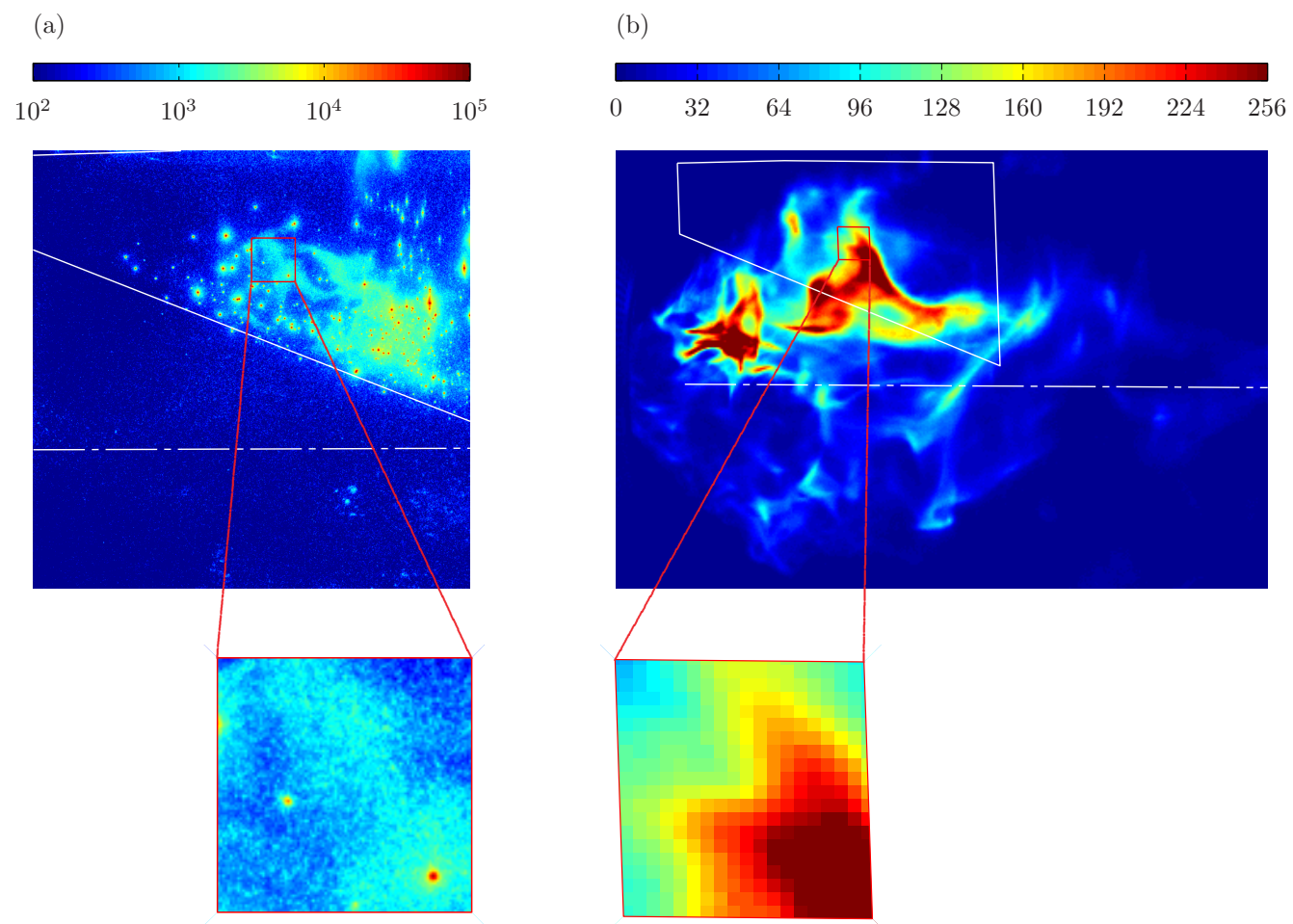


Fig. 5.11: Simultaneous images of fuel and high-intensity flame: (a) uncorrected hot PLIF image. Note the logarithmic intensity scale; (b) flame image containing highest intensity emission in region A.

flame intensity illustrated in Figure 5.11. The flame image illustrated in this figure contains the largest intensity count recorded in region A. Note that the fluorescence image and detail are presented with a logarithmic intensity colour map to highlight the low-level signal. It is clear from a comparison of Figures 5.11(a) and 5.11(b), that the shape of the saturated flame activity broadly corresponds to that of low-level signal in the PLIF image.

Whatever its origin, the flame interference signal is evidently comparatively small. While large droplets can generate pixel counts approaching 100% of the camera's dynamic range, the brightest recorded flame contributes signal representing no more than 3% of this detection range. This kerosene PLIF technique is therefore suitable for the detection of fuel in flames operating under altitude conditions.

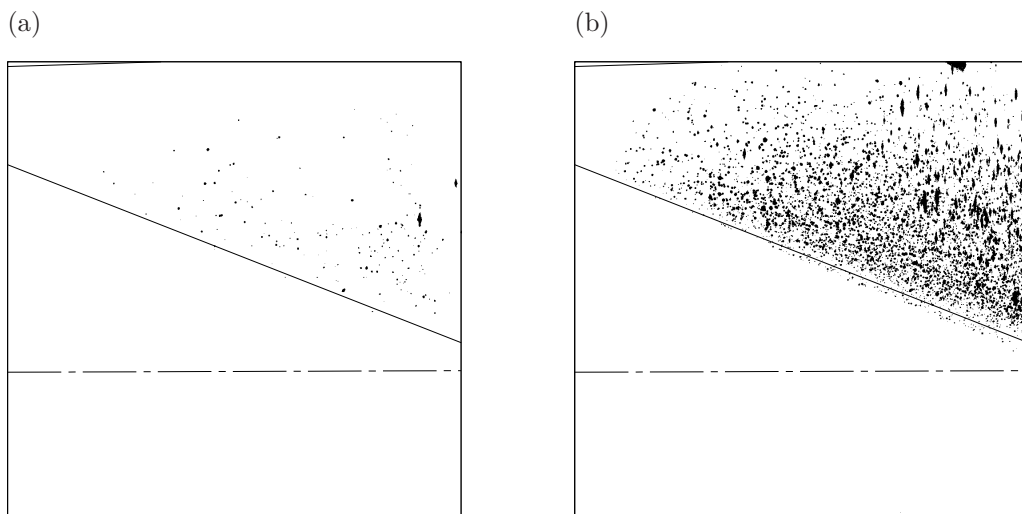


Fig. 5.12: Fuel droplets following flame stabilisation: (a) individual image; (b) composite of all acquired images. A threshold value of  $10^4$  was used to binarise the PLIF images.

The droplets apparent in Figures 5.10 and 5.11 are sufficiently small to remain suspended in the CRZ without impinging on the combustor walls, yet large enough to avoid being totally consumed by flame. Since only a small fraction of the total fuel

mass survives in this form, the individual droplets in each hot PLIF image appear as well-spaced, similarly-sized, regions of high-intensity signal. By applying a fixed threshold to each fluorescence image it is possible to construct a scatter plot of fuel droplet placement that requires no correction. This approach was not possible in Section 5.1.1 due to the continuous signal variation caused by the presence of small droplets and fuel vapour. The regions of the PLIF image presented in Figure 5.11 with a signal count exceeding  $10^4$  were identified and used to construct the binary image illustrated in Figure 5.12(a). A composite image formed by overlaying all of the binary hot PLIF images of stabilised flame is shown in Figure 5.12(b). Droplets most frequently occupy the bottom half of the excitation volume, with relatively little fuel found immediately below the combustor outside wall. Note that compared to the uncorrected mean images, the concentration of signal has moved downstream and inwards towards the centre-line of the combustion chamber.

## 5.2 PLIF image correction

Though the preliminary evaluation described in Section 5.1 provided useful insight, the global fuel distribution is not well represented by the uncorrected images. Point-to-point differences in measured signal arise from absorption and scattering of the excitation wavelength, the varying cross-section of the sheet, and the non-uniform distribution of laser energy. Corrections for these factors are described in Sections 5.2.1 to 5.2.4.

Fluctuations in laser energy are also responsible for shot-to-shot differences in signal level as described previously in Section 4.2.1. No correction has been applied for these variations, and individual images are not therefore directly comparable. However, the influence of the fluctuations is removed by averaging, and the mean safe and unsafe images are compared in Section 5.2.5.

### 5.2.1 Scattering and reflections

When PLIF is used to investigate the fuel distribution in a spray, the magnitude and placement of the fluorescence signal are influenced by optical absorption and scattering. These effects have proved to be significant during previous studies, most notably those investigating the dense, hollow-cone sprays produced by automotive fuel injectors (Sick and Stojkovic 2001; Stojkovic and Sick 2001; Koh et al. 2003).

In the absence of flame, absorption of the excitation wavelength is governed by the mass of fuel contained in the excited region of the spray. The degree of optical scattering is determined by the spray density, usually defined as the liquid surface area per unit volume. These processes modify the apparent fuel concentration in three ways. Firstly, a dense spray can significantly attenuate the laser sheet. Secondly scattered light may induce secondary fluorescence of fuel droplets outside the sheet. Finally, the fuel lying between the sheet and the camera can attenuate the primary fluorescence signal.

The cold PLIF images acquired during this study generally contain a region of diffuse signal below the excitation volume. Liquid droplets in this region fluoresce when excited by scattered laser light and reflect fluorescence radiated from the sheet. The structure of this signal is illustrated in Figure 5.13 (cf. Figure 5.2), where a logarithmic scale has been used to emphasise low-intensity regions. Two portions of the image are shown in detail: region A inside the sheet as previously identified in Section 5.1, and region B at a point outside the sheet where scattering was suspected to be significant. The intensity legend indicates that the maximum signal in region B (light blue) is approximately two orders of magnitude less than that recorded in region A (red). Scattering effects are nonetheless evident and should be accounted for.

The shot-to-shot distribution of scattered signal was characterised by calculating the total intensity contained in region B for each individual cold image. Histograms of the region B intensity are plotted in Figure 5.14, and the sample mean and

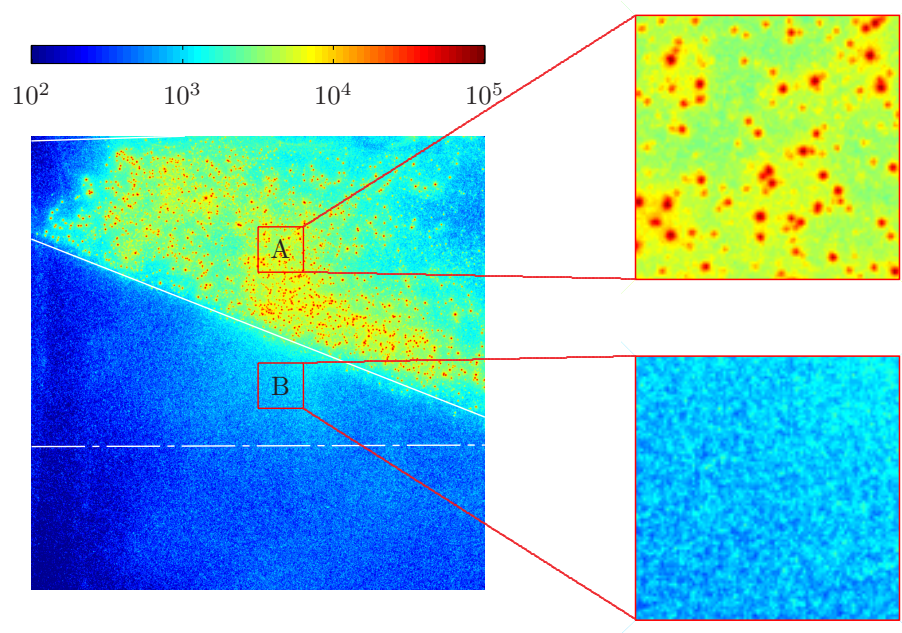


Fig. 5.13: Uncorrected, individual, cold PLIF image acquired at unsafe condition. Note the logarithmic intensity scale.

standard deviation at each test condition are listed in Table 5.2. The fluorescence intensity distributions extracted from region B, reflect trends observed in region A. Significant image-to-image variation in the fuel signal is evident, and the mean and standard deviation are both larger at the unsafe condition than at the safe set point.

Table 5.2: Statistics of cold, total PLIF intensity in region B.

	mean per pixel	mean ( $\times 10^7$ )	std. dev. ( $\times 10^7$ )
safe	746	0.78	0.25
unsafe	1186	1.24	0.63

To minimise the sheet signal resulting from these effects, scattering constants were subtracted from both uncorrected mean images. The safe scattering constant, extracted from the safe mean image, corresponded to the mean count per pixel recorded in region B. This value of 746 counts was subtracted from every element

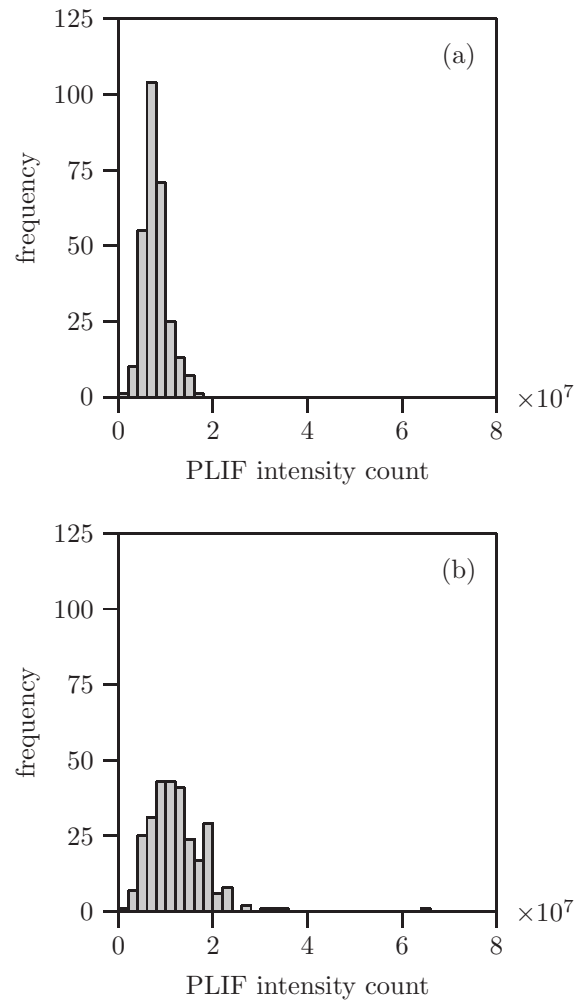


Fig. 5.14: Histograms of cold PLIF signal in region B: (a) safe; (b) unsafe. Note that region B is identified in Figure 5.13

of the safe mean image. The unsafe scattering constant, equal to 1186 counts, was calculated in an identical manner, and similarly subtracted from every pixel of the unsafe mean image. These scattering corrections were applied prior to further processing.

The assumption justifying this approach is that scattering raises the fluorescence signal radiating from every point in the laser sheet by an equal amount. Though the situation is clearly more complex than this, assessing the exact spatial variation in these effects is challenging without droplet size information, and perhaps unnecessary under these conditions, where the effects are not particularly significant.

Having subtracted the scattering constants, the resulting mean images were multiplied by the sheet thickness, frontal area and beam energy distribution correction matrices. The operations performed during corrective processing can therefore be represented as follows

$$\langle I_c \rangle = (\langle I_u \rangle - S) \prod_{k=1}^3 \psi_k , \quad (5.2)$$

where  $\langle I_c \rangle$  and  $\langle I_u \rangle$  are the mean corrected and mean uncorrected images (see Eq. (5.1)),  $S$  is the scattering constant, and  $\psi_k$  ( $k = 1, 2, 3$ ) are the three correction factors. The derivation of these correction matrices is discussed in Sections 5.2.2 to 5.2.4.

### 5.2.2 Sheet thickness

The thickness of the laser sheet varies considerably within the imaged area. Convergence of the beam caused by the third sheet-formation lens causes a reduction in the centre-line thickness from 1.7 mm at the left edge of the PLIF image to 1.2 mm at the right edge. More significant changes in sheet thickness throughout the imaged area result from the elliptical cross-section of the sheet. Since the edges of the sheet are particularly thin (minimum thickness = 0.6 mm), a correction factor based on the sheet thickness is required to correct the mean images.

The correction factor at a point is inversely proportional to the sheet thickness.

This correction factor therefore varies with both the radial distance from the focal point, and the angle to the sheet centre-line. The sheet thickness correction factor,  $\psi_1$ , is therefore given by

$$\psi_1 = \frac{t_{\text{ref}}}{t}, \quad (5.3)$$

where  $t_{\text{ref}}$  and  $t$  are the sheet thicknesses at a fixed reference point and the point requiring correction respectively. The three correction factors are, by definition, equal to 1 at the fixed reference point. This is located 100 mm from the focal point of the final lens, on an optical ray bisecting the lower half of the sheet (white, filled circle in Figure 5.18(a)). The sheet thickness at any point can be calculated by substituting its radial and angular position into Eq. (B.14). Note that the correction factor was not calculated beyond the clipped boundaries of the sheet, and singularities at the unclipped edges were thus avoided.

Discrete droplets are resolved in individual PLIF images, generating localised regions of high intensity count. Corrective amplification or attenuation of an individual image therefore requires the addition or removal of signal representing discrete droplets. Since the location of these droplets is unknown, it is not possible to apply the sheet thickness correction to individual PLIF images. However, element-wise averaging eliminates the localised high-intensity regions, allowing the correction to be applied to mean images.

### 5.2.3 Frontal area

The PLIF excitation volume is illustrated in Figure 3.7. During propagation through the combustion chamber, the inside and outside edges of the sheet diverge, and the sheet thickness decreases. A single correction factor has been derived to account for the point-to-point irradiance variations resulting from these changes in the sheet cross-section.

On entering the combustion chamber, the propagating front of the laser sheet forms a series of curved surfaces centred at the focal point of the final lens. The

correction factor required at a point is proportional to the area of the curved surface containing the point, and thus varies solely with the radial distance from the focal point (see Appendix B). The frontal area correction factor,  $\psi_2$ , is therefore given by

$$\psi_2 = \frac{A}{A_{\text{ref}}}, \quad (5.4)$$

where  $A$  and  $A_{\text{ref}}$  are the areas of the surfaces containing the point requiring correction, and the fixed reference point respectively. As described in Appendix B, a general expression was derived for the area of the surface passing through every imaged point. Each area was evaluated numerically, and the corresponding correction factor calculated.

Both the sheet thickness and frontal area correction factors vary with the radial distance from the focal point of the final lens. These correction factors are plotted as a function of radius in Figure 5.15(a). A black, filled circle identifies the correction factor reference point. Both factors increase monotonically with distance from the focal point. The combined effect of the two radial corrections varies between a factor of 0.5 and 1.5. This is relatively small compared to the angular corrections described in the next section.

The effect of the combined radial corrections is also illustrated in Figure 5.15(b). The uncorrected fluorescence profile was extracted from the mean, safe image along the optical ray passing through the fixed reference point (radial, white dashed line in Figure 5.18(a)). At larger radial distances, the combined correction factor flattens the fluorescence profile. This indicates that the downstream region of low-intensity signal observed in the uncorrected, mean images, is predominantly due to sheet geometry effects. Excitation wavelength attenuation is therefore less significant than might be suspected based on the uncorrected images alone.

#### 5.2.4 Beam energy distribution

The principal cause of spatial irradiance variations is the non-uniform energy profile of the laser beam. The slit traverse results described in Section 4.2.2 were used to

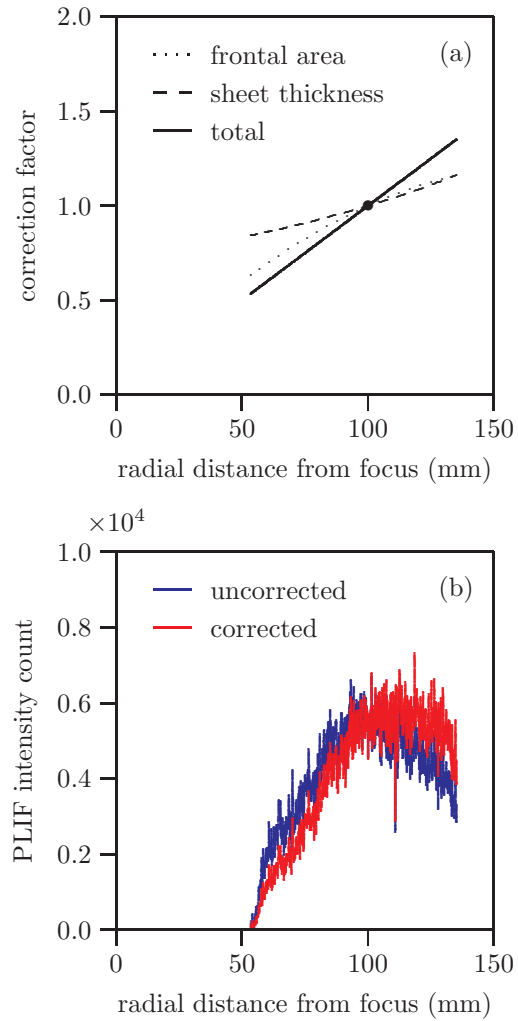


Fig. 5.15: Radial correction effects: (a) variation in radial correction factors with distance from focal point; (b) effect of combined corrections on mean, safe cold profiles along radial line (see Figure 5.18(a)).

correct for these non-uniformities in the incoming beam.

The beam energy profile was characterised as the measured change in power gradient with distance through the beam. On leaving the final lens, the propagating front of laser light forms a series of concentric arced surfaces. The irradiance variations in the sheet can therefore be quantified by mapping the measured beam profile along the frontal arcs so that the edges of the beam lie on the inside and outside boundaries of the unclipped sheet. The correction factor required at a point is then inversely proportional to the measured power gradient mapped onto the point. The beam energy distribution correction factor,  $\psi_3$ , is therefore given by

$$\psi_3 = \frac{(dP/dl)_{\text{ref}}}{(dP/dl)}, \quad (5.5)$$

where  $(dP/dl)_{\text{ref}}$  and  $(dP/dl)$  are the power gradients mapped onto the correction factor reference point and the point requiring correction respectively.

The measured beam power gradient is plotted in Figure 5.16 as a function of normalised angle to the optical axis. The fluorescence profile along a frontal arc was extracted from the mean, unsafe image, and is also presented in Figure 5.16. Normalised angles of -1, 0 and 1 correspond to the unclipped inside edge, centre-line and unclipped outside edge of the sheet respectively. The clipped sheet boundaries are represented by dashed lines. The non-Gaussian energy shoulders first noted in Section 4.2, clearly influence the fluorescence profile. Indeed, the upper feature (normalised angle  $\approx 0.5$ ), has been used to locate the beam energy profile relative to the sheet. This was necessary due to difficulties in identifying the centre of the measured energy distribution (see Section 4.2.2).

These observations confirmed the importance of calculating the beam energy correction based on a measured profile. The assumption of a Gaussian distribution would not have removed image features associated with the laser output.

The beam energy distribution correction factor varies solely with the angle to the optical axis. In addition to the radial dependence discussed in Section 5.2.3, the sheet thickness factor also changes with angle. These correction factors are plotted

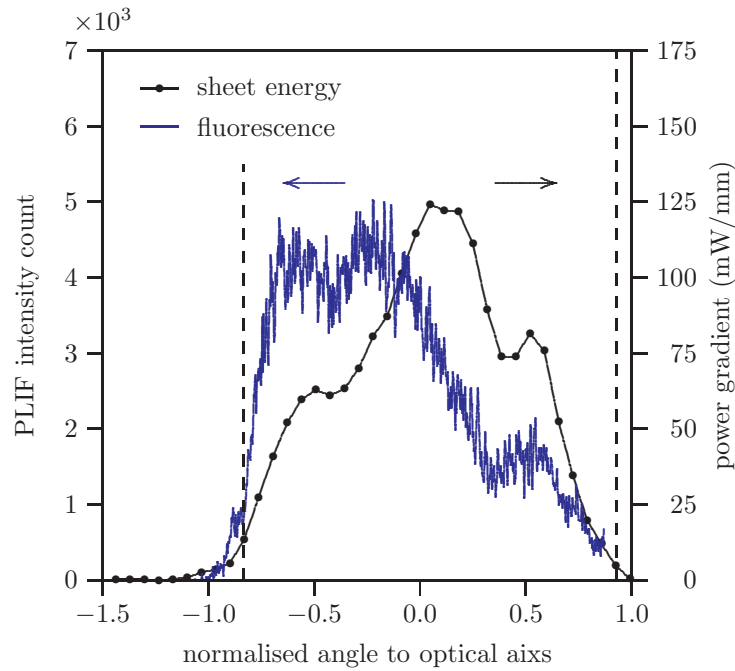


Fig. 5.16: Comparison of beam energy profile and fluorescence signal.

as a function of normalised angle in Figure 5.17(a). Note that the plots extend between the clipped boundaries of the sheet. The correction factor reference point is again identified by a black, filled circle.

The beam energy distribution correction factor is similar in magnitude to the radial correction factors in the central two quadrants of the sheet (i.e. normalised angle between -0.5 and 0.5). However, at the outside edges of the sheet, the beam energy correction is dominant and large. This effect is particularly pronounced at the outside wall, where a correction factor of 8.8 is required. At both boundaries, the magnitude of the correction factor is extremely sensitive to the position of the beam energy profile relative to the sheet. As the shoulder feature used to locate the energy profile is rather broad, and the extracted fluorescence plot is relatively noisy (see Figure 5.16), the exact placement of the energy profile is uncertain. This error is less important towards the centre of the sheet, where the correction factor is much less sensitive to misalignment of the energy profile.

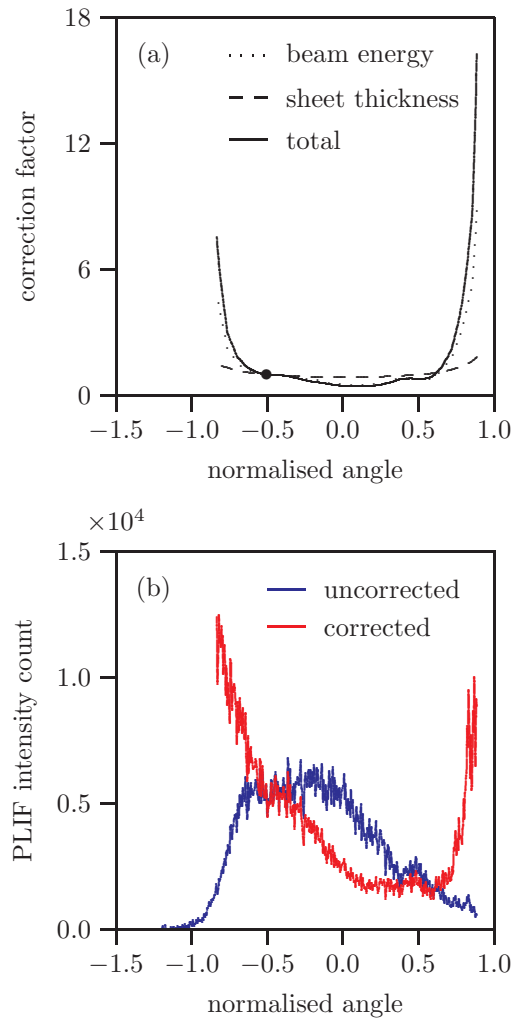


Fig. 5.17: Angular correction effects: (a) variation in angular correction factors with normalised angle to optical axis; (b) effect of combined corrections on mean, safe cold profiles along frontal arc (see Figure 5.18(a)).

The sheet thickness correction factor also increases towards the edges of the sheet to account for thinning due to its elliptical cross-section. Though the sheet thickness correction varies by a factor of only 2.1, it combines with the beam energy factor to generate comparatively large corrections at the sheet edges. The largest total angular correction factor is applied at the outside boundary and is equal to 16.3.

The effects of the combined angular corrections on the mean, safe fluorescence signal are illustrated in Figure 5.17(b). The uncorrected fluorescence profile was extracted from the mean, safe image along the arc passing through the correction factor reference point. This curve is identified as a white dashed line in Figure 5.18(a). The uncorrected profile is radically modified at the edges by applying the angular corrections. A correction factor greater than about 3 is regarded as questionable since the noise associated with low-level signal is amplified along with the signal itself. Therefore subsequent analysis of the mean images in the following section considers only those regions where a total correction factor of less than 3 is applied.

### 5.2.5 Interpretation of corrected images

The mean, corrected, cold PLIF images are presented in Figure 5.18. Comparison of the corrected and uncorrected images (Figure 5.6), reveals important differences. Firstly, the size of the downstream, low-intensity region has been reduced by the radial corrections. This indicates that attenuation of the laser energy is not as severe as the uncorrected images would suggest. Secondly, the dark stripe extending across the top half of the images in Figure 5.6 has been virtually eliminated by the beam energy distribution correction. This confirms that the stripe was not caused by lens contamination as originally suspected, but resulted from non-uniformities in the beam profile, as measured in Section 4.2.

A further key difference between the corrected and uncorrected images is that the high-intensity signal close to region A in Figure 5.6 has moved downwards towards the fuel injector centre-line in Figure 5.18. This results in a wider, low-intensity

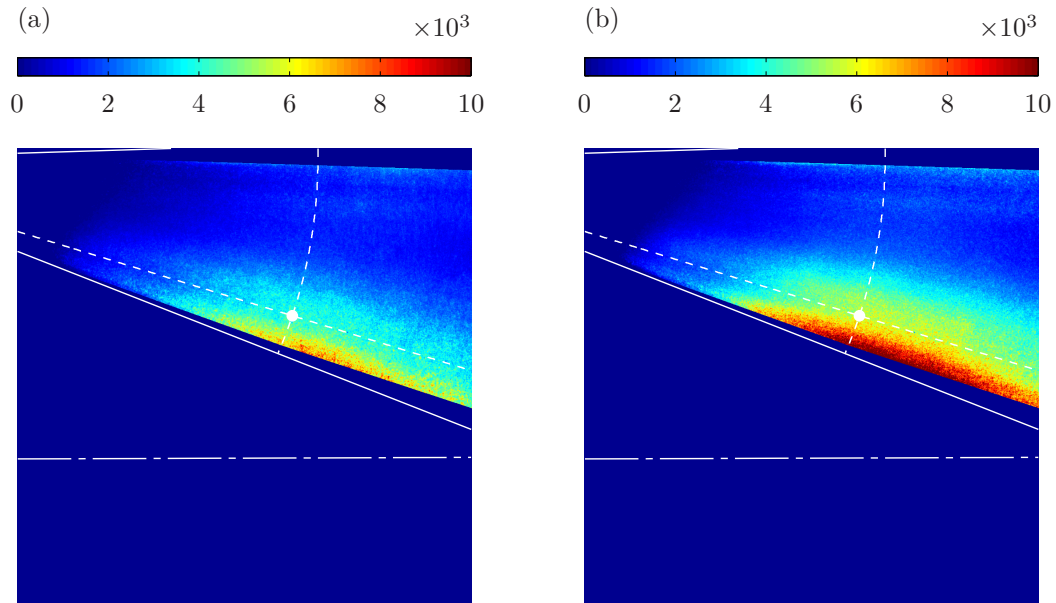


Fig. 5.18: Corrected, mean, cold PLIF images: (a) safe; (b) unsafe. Note that areas with a correction factor greater than 3 have been set to zero.

corridor close to the outside wall of the combustor.

The signal on the outside wall itself was amplified to such an extent by the corrections that it was considered unreliable and has therefore been removed from the images. Nonetheless, the uncorrected images analysed previously in Section 5.1 showed that more fuel is deposited on the outside wall at the safe condition than at the unsafe condition.

With the exception of the scattering constant, identical corrections have been applied to images acquired at the two test conditions. Though the scattering constant subtracted from the images is smaller at the safe condition, the mean fluorescence intensity remains higher at the unsafe set point, reproducing the trend identified in the uncorrected images (see Section 5.1.2). The elevated signal at the unsafe condition therefore indicates the presence of more fuel in suspension below the igniter.

The distribution of fuel apparent in the safe corrected image corresponds closely to that observed in the hot PLIF scatter plot of mid-sized droplets presented in

Figure 5.12. The placement of each fuel droplet in this plot is unaffected by the PLIF signal strength, and no correction is therefore required. Figures 5.12 and 5.18 thus provide evidence that fuel is present in greater concentrations towards the inside, downstream boundary of the excitation region. This suggests that flow recirculation is trapping fuel in this region whether or not a flame is present.

### 5.3 CFD comparison

Computational modelling of the combustor air-flow has been performed by Rolls-Royce plc to develop an understanding of the cold flow fields at the safe and unsafe set points (Goddard and Zedda 2007). A non-reacting large-eddy simulation was conducted using the Rolls-Royce corporate combustion program, PRECISE. The modelling implemented in this software is described by James et al. (2006). The geometry and boundary conditions defined in the model were not identical to those of the test facility, but instead corresponded to a single sector with periodic boundary conditions (i.e. representing a full combustor annulus). The results of the simulation nonetheless provide a useful qualitative comparison with the experiment. The CFD results presented below are the time-averaged components of the velocity field extracted from the injector mid-plane.

The LES method provides a more accurate and complete description of the flow field than alternative Reynolds-averaged Navier-Stokes (RANS) techniques (Pope 2000; Boudier et al. 2007). There is, however, a relatively high computational cost associated with LES, particularly for high Reynolds number, wall-bounded flows. Furthermore, incorporating finite-rate chemistry into an LES method to model turbulent reacting flows is prohibitively expensive, ruling out combustion LES as a design tool at present (Cant and Mastorakos 2008).

Time-averaged velocity vector maps generated by LES were extracted from the plane of the laser sheet and transformed into the PLIF imaging plane according to the process described in Appendix A. In this way the flow field in Figure 5.19 appears

as if viewed from the PLIF camera. Thus the corrected PLIF images (Figure 5.18) can be directly compared with the transformed CFD velocity fields.

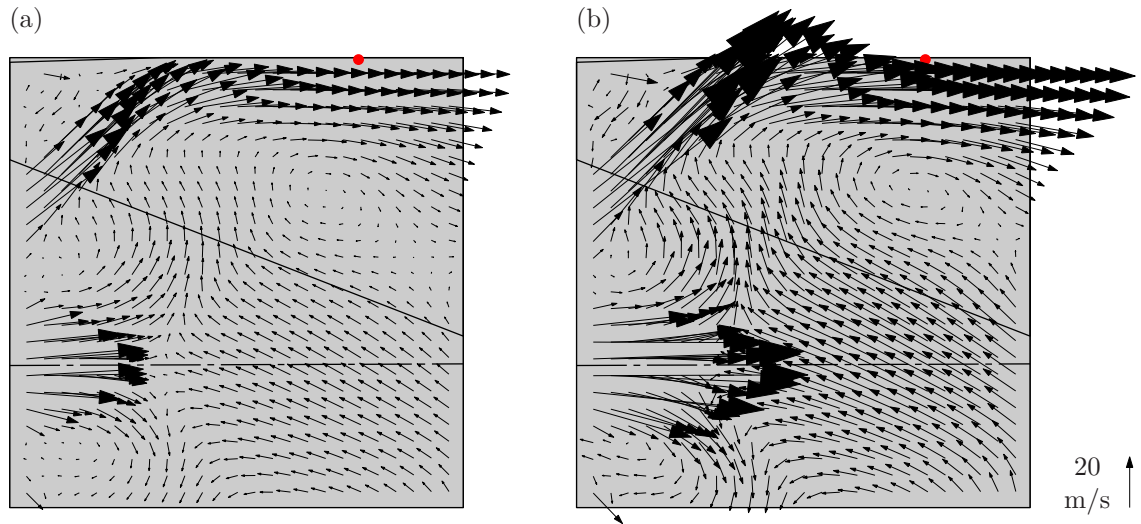


Fig. 5.19: Time-averaged velocity in sheet plane predicted by CFD: (a) safe; (b) unsafe. The igniter tip is identified by a filled red circle.

The following features are common to both the safe and unsafe flow fields (Figures 5.19(a) and 5.19(b) respectively). A high-velocity stream of air enters the combustion chamber towards the edge of the fuel injector at an angle of approximately  $45^\circ$  to the injector centre-line. The flow is deflected by the combustor outside wall, creating a corridor of high-velocity air along the underside of the wall. A local recirculation region is evident roughly 25 mm below the igniter tip. As noted in Section 5.1.1, the flow patterns are broadly similar at the safe and unsafe set points, reflecting the extremely high Reynolds number in both cases. At any given point, the ratio of the vector length in Figure 5.19(b) to that in Figure 5.19(a) is approximately equal to the ratio of air mass flow rates (cf. Table 3.1).

The flow velocities and patterns at the two test conditions support the fuel placement observations reported earlier in this chapter. The high-velocity air stream entering at  $45^\circ$  behaves as an air curtain preventing fuel injected close to the centre-

line from reaching the outer boundary. As argued in Section 5.1.1, large fuel droplets can penetrate this curtain by virtue of their momentum, resulting in the deposition of fuel on the outside combustor wall and the associated PLIF signal observed in Figure 5.7. As indicated in Figure 5.19(a), the air curtain is also weaker at the safe condition, enabling further droplets to impinge on the wall.

The comparatively high fuel concentration in the lower half of the sheet observed in Figure 5.18 coincides with an area of low-velocity, recirculated flow. Smaller droplets tend to accumulate in this recirculation region as evidenced by the PLIF details in Figures 5.3 and 5.4. As discussed in Section 5.1.1, the recirculating flows generated under altitude conditions therefore control the point-to-point drop size distribution inside the combustor. It is this feature that explains the disparity in the magnitude and distribution of the PLIF fuel signals at the two test conditions. Thus the CFD results are consistent with the PLIF findings, namely that there is more fuel on the wall and less in the flow at the safe condition, and less fuel on the wall and more in the flow at the unsafe condition.

# Chapter 6

## Results III: Flame Imaging

While the PLIF imaging described in Chapter 5 provides useful insight into fuel placement prior to the spark event, it is the high-speed recordings of flame radiation that provide the key information concerning relight ignition and flame development. The analysis and interpretation of these results is described in this chapter.

### 6.1 Flame tracking software

Given the large distance separating the igniter from the fuel injector, the spatial development of the flame is critical in determining the success or failure of a relight attempt. Image processing software has therefore been developed to monitor the motion and breakup of flame in each high-speed ignition sequence (Read et al. 2008). The design and implementation of an algorithm to generate a flame centroid trajectory map corresponding to each ignition event is described in detail below. As explained later in Sections 6.2 and 6.3, the output from this program was analysed extensively to investigate the differences between successful and unsuccessful relight attempts.

### 6.1.1 Search principle

A schematic illustration of flame development and breakup is presented in Figure 6.1. The intense light emitted by each spark produces a spatially well-defined saturated region immediately below the igniter tip (see Figure 4.5). The flame tracking process is initialised by searching a small square contained in this region (dashed line in Figure 6.1(a)) for pixels exceeding a high-level threshold. The extent of the spark kernel is determined by searching outwards from this square, thus excluding the reflections of the spark apparent in Figure 4.5.

The following frame, represented by Figure 6.1(b), is then searched to identify ‘child’ flame kernels in the area formerly occupied by the ‘parent’ spark. Consecutive frames are processed in the same manner, on each occasion noting the parents of any detected flame kernel. By recording the centroid location of every kernel, it is possible to construct a unique trajectory map illustrating the motion of visible flame during each ignition event.

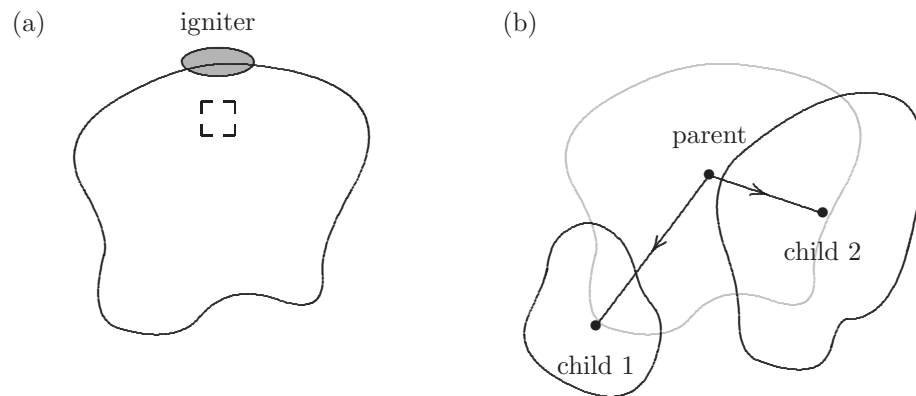


Fig. 6.1: The flame tracking process: (a) first frame; (b) second frame.

The program records the location of the intensity centroid associated with every flame kernel captured in the high-speed recordings. The kernels are constructed by searching the pixels that contain flame in the preceding image. Figure 6.2 shows two illustrative examples of flame kernel construction. The pixels constituting a single

flame kernel are assigned a unique number. The grey pixels without a number in Figure 6.2 register a count that is above the threshold, but have not yet been assigned to a specific kernel.

Let us consider kernel number ‘2’ shown in Figure 6.2(a). Here, the black square represents the first discovered member of the group. The full extent of this flame body is identified by searching the area around the black pixel for other high-intensity pixels. The path of this search follows a series of expanding, concentric circuits. The 8 elements bordering the black square are searched first, followed by the 16 pixels surrounding this square, and so on. To join kernel 2, a pixel must have a count that exceeds the threshold, and must border a pixel that already belongs to the group. The expanding search continues until a circuit is completed without assigning a new pixel to the group. For the case illustrated in Figure 6.2(a), the search continues to the edge of the image, revealing an existing kernel (number 1), and several unassigned pixels that are not connected to kernel 2.

Though a single expanding search is often sufficient to reveal the entire flame kernel, this is not always the case. The grey pixels at the top of Figure 6.2(b) exceed the threshold but remain unassigned to a kernel as the ‘linking’ pixel lies outside the circuit during the first search. If unassigned cells are encountered during the first expansion, then a further search is required, this time proceeding from the perimeter to the centre of the search area. The search oscillates inwards and outwards in this manner until no new cells are allocated, whereupon kernel 2 may be regarded as complete.

### 6.1.2 Algorithm features

Though simple in principle, the implementation of the search algorithm described in Section 6.1.1 is complicated by several factors. Firstly, the measured flame intensity varies significantly during each ignition event. As noted in Section 4.4, and illustrated in Figure 4.5, the spark itself is extremely bright and the initial high

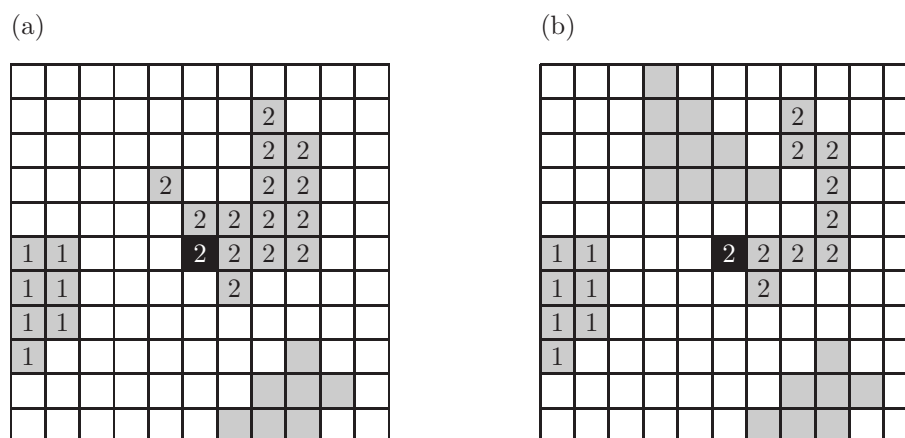


Fig. 6.2: The kernel search process: (a) single expansion required; (b) multiple expansions required.

speed images contain strong reflections on the combustor walls. In contrast, during later development, small, faint, kernels are observed separating from larger volumes of flame. These low-intensity fragments often grow to occupy large areas, and it is therefore important for the tracking program to retain them in addition to the bright kernels. An adaptive threshold is therefore required to ensure that bright spark reflections are not classified as flame, while faint flame fragments are successfully identified. This is given by

$$I_{\text{thr}} = pI_{\text{max}} \quad \text{where } p = 0.5. \quad (6.1)$$

$I_{\text{max}}$  is the maximum intensity in the parent kernel. Any pixel with a count exceeding this value is assigned to a new child kernel that is expanded to its full extent according to the procedure described in Section 6.1.1.

However, the small regions of flame described above produce an additional difficulty. Fragments of flame are often ejected from a parent kernel at comparatively high velocity. The child kernels depicted in Figure 6.1(b) can therefore lie outside the boundary of the parent. To ensure detection of these child kernels, a second low-threshold search is conducted of the parent flame area and an expanded region

around it (corresponding to  $\approx 5\%$  of the image height).

The construction of a child kernel during this expanded search is illustrated in Figure 6.3. A relatively bright flame body lying within the bounds of its parent is identified as kernel  $C_1$ . A faint flame body lying outside the boundary of the original search must also be identified. An expanded region is searched for pixels exceeding a low threshold given by  $I_{\text{thr}} = 1$ . The filled circle in Figure 6.3(a) represents the first identified point where  $I(x_i) > I_{\text{thr}}$ . On discovering this pixel at  $x_i$ , the threshold is immediately reset

$$I_{\text{thr}} = \max \{I_{\text{thr}}, pI(x_i)\}, \quad (6.2)$$

and a new child is constructed as described in Section 6.1.1. If the existing child  $C_1$  is encountered while building the new kernel, the threshold is again reset to remove the pixels in the current child with the lowest count

$$I_{\text{thr}} = I_{\text{min}}. \quad (6.3)$$

The dashed line in Figure 6.3(a) indicates the threshold intensity that will separate the new child from  $C_1$ . This is achieved by repeatedly resetting the threshold according to Eq. (6.3). The separated kernel is then examined to determine whether  $I_{\text{min}} > pI_{\text{max}}$ , where  $I_{\text{max}}$  is the maximum pixel count contained in the new child. If this condition is satisfied, then the child build is complete; otherwise the threshold is again reset

$$I_{\text{thr}} = pI_{\text{max}}, \quad (6.4)$$

and the final build commences at the pixel registering the maximum intensity. This process generates the new kernel  $C_2$ , illustrated in Figure 6.3(b).

The adaptive threshold and expanded search features improve the program's ability to retain faint flame, and produce satisfactory tracks of flame activity. However, these features can also lead to misrepresentation of the flame break-up that must be addressed. For example, the expanded search tends to create child kernels with a large number of parents. While this is valid in the case where several flame

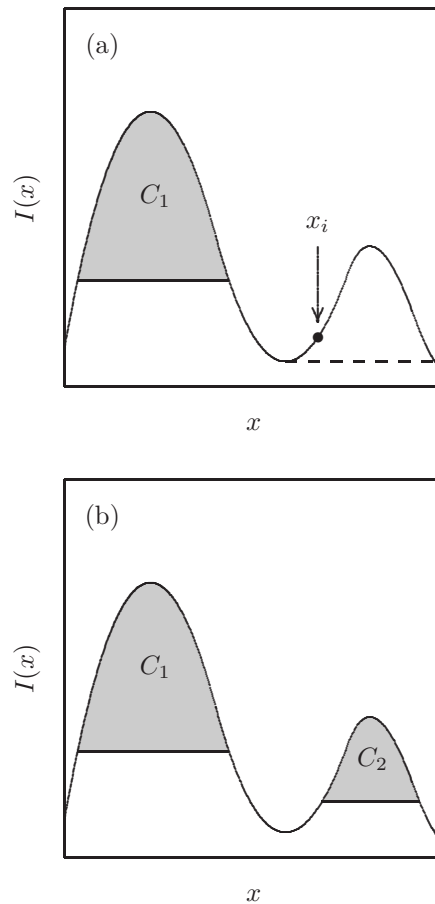


Fig. 6.3: The expanded search process: (a) kernel isolation; (b) final build.

kernels have recombined, the program should also permit independent flame bodies to pass close to each other without being identified as a single entity. To address this, the relative intensity of the parents and their proximity to the child is examined. An apparent parent is regarded as valid if the distance between the parent and the child is no more than twice that from the closest parent to that child. In addition, the parent of a given child must not be less than half the size of the largest parent.

As noted in Section 4.3.1, complete loss of signal occurs during 6 of the 94 successful events recorded at the safe set point. However, a much higher number of the recordings, 56 in total, include images containing no pixels with a count

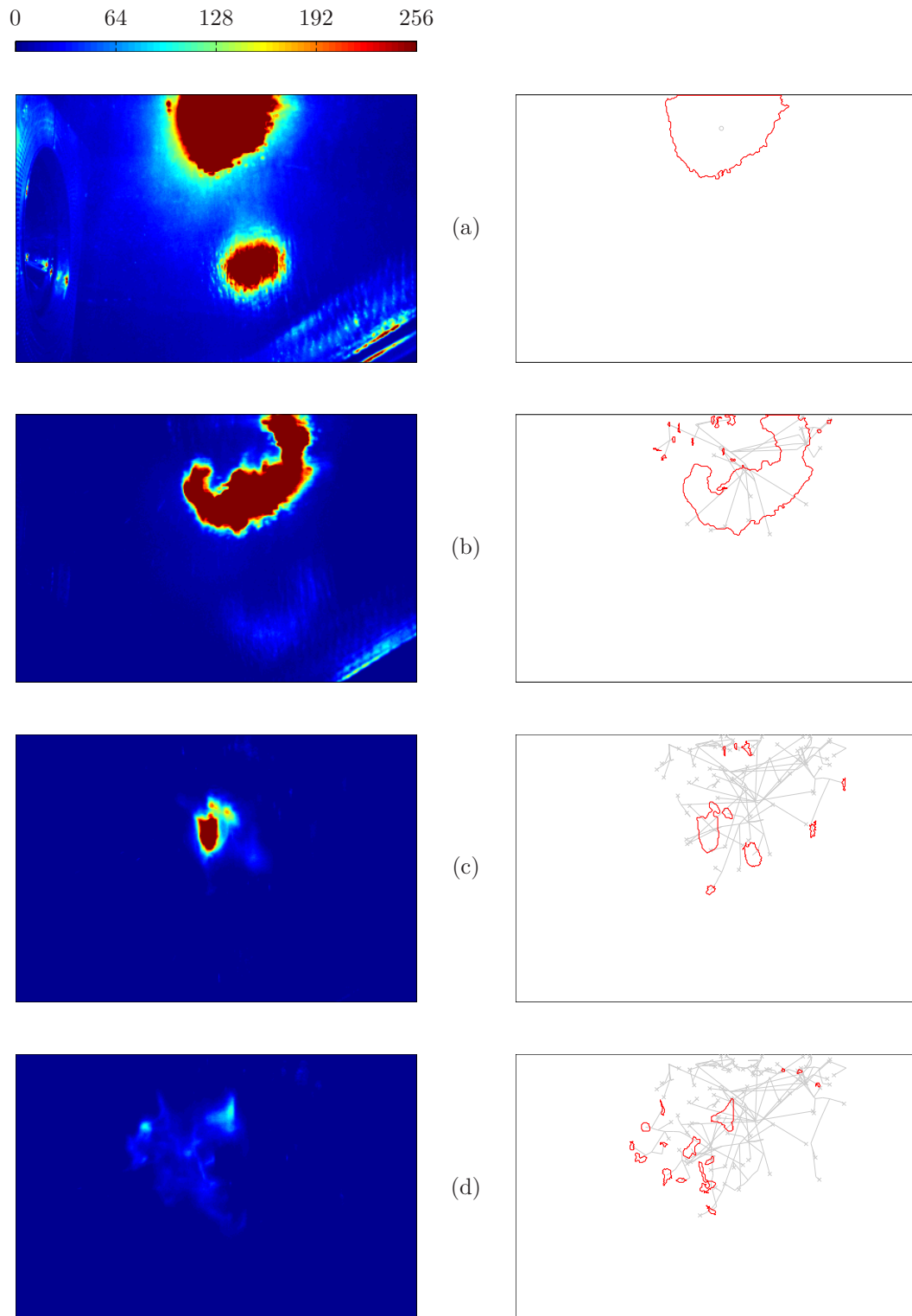


Fig. 6.4: Early high-speed images (left) and corresponding kernel outlines (right). The timing of frames (a) to (d) is indicated in Figure 6.5.

exceeding the low threshold. These low-intensity episodes typically occur for a period of less than 1 ms, between 10 and 20 ms following the spark discharge. The program can continue to track the flame following each of these episodes as follows. Having discovered an image registering no flame activity, a fixed-threshold search of the subsequent frames is performed until a new kernel is identified, whereupon the tracking process continues as described above. Consequently, though breaks in the trajectory plot occasionally occur, the program is able to track successful events through to recovery.

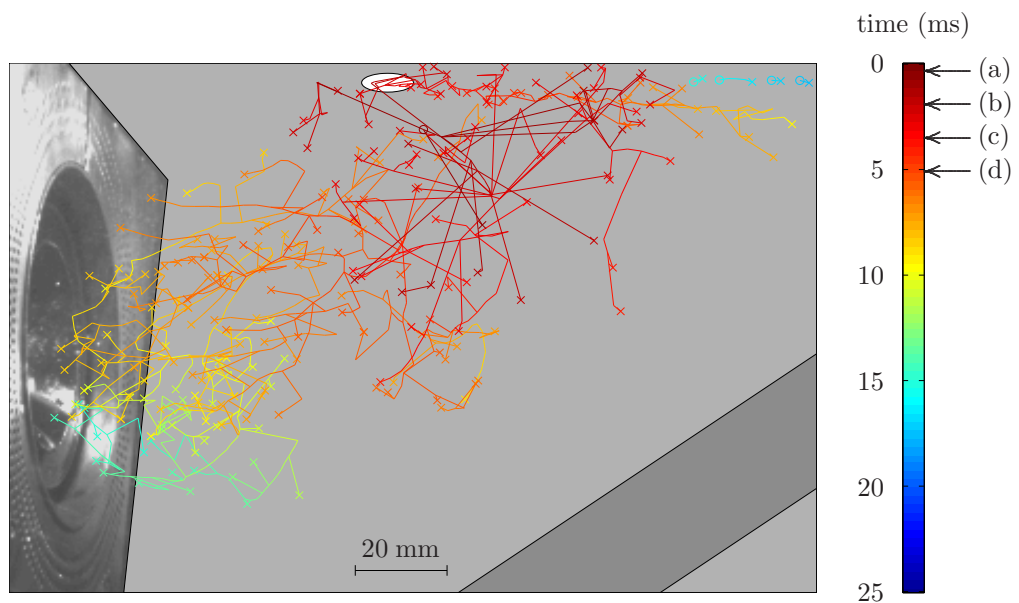


Fig. 6.5: Example of a trajectory map. The end of the igniter is represented by the white filled oval. The labels to the right of the map indicate the timing of each frame in Figure 6.4.

The primary results obtained from the flame tracking software are a series of trajectory plots, illustrating the motion and breakup of flame during a single ignition attempt (see Figure 6.4). Figure 6.5 shows an example of a complete trajectory plot for an unsuccessful ignition attempt at the safe condition. Flame centroid trajectories are colour-coded with respect to time, progressing from dark red immediately

following the spark to dark blue 25 ms later. The centre of the spark kernel is identified by an unfilled red circle. Each line represents the path of an individual flame kernel. Fragmentation and recombination of these kernels is represented by branching and merging of the lines respectively. The disappearance of a flame kernel following extinction is indicated by a cross.

The broken blue trajectories in the top right hand corner of Figure 6.5 indicate very faint flame exiting the combustion chamber around 20 to 25 ms following the spark. The periodic loss and recovery of this weak signal illustrates the program's ability to continue the flame track following low-intensity episodes.

## 6.2 Developing flame

Trajectory plots of flame motion have been examined qualitatively to identify categories of ignition development. The variations in flame size and spark velocity provide valuable quantitative information concerning the process, and permit investigation of the systematic differences between successful and unsuccessful ignition events.

### 6.2.1 Flame trajectories

The flame tracking software was used to generate a flame trajectory plot for every high-speed recording of an ignition attempt. A trajectory plot corresponding to a safe, successful relight event is presented in Figure 6.6(a). As in Figure 6.5, the plot is colour-coded with respect to time, progressively changing from dark red to dark blue during a period of 25 ms.

Figure 6.6(a) resembles the flame development maps associated with many successful ignition events. Following initial activity below the igniter tip, flame kernels move upstream, before developing strongly in the lower, upstream quadrant of the combustion chamber. When recovery occurs, 24.6 ms following the spark discharge,

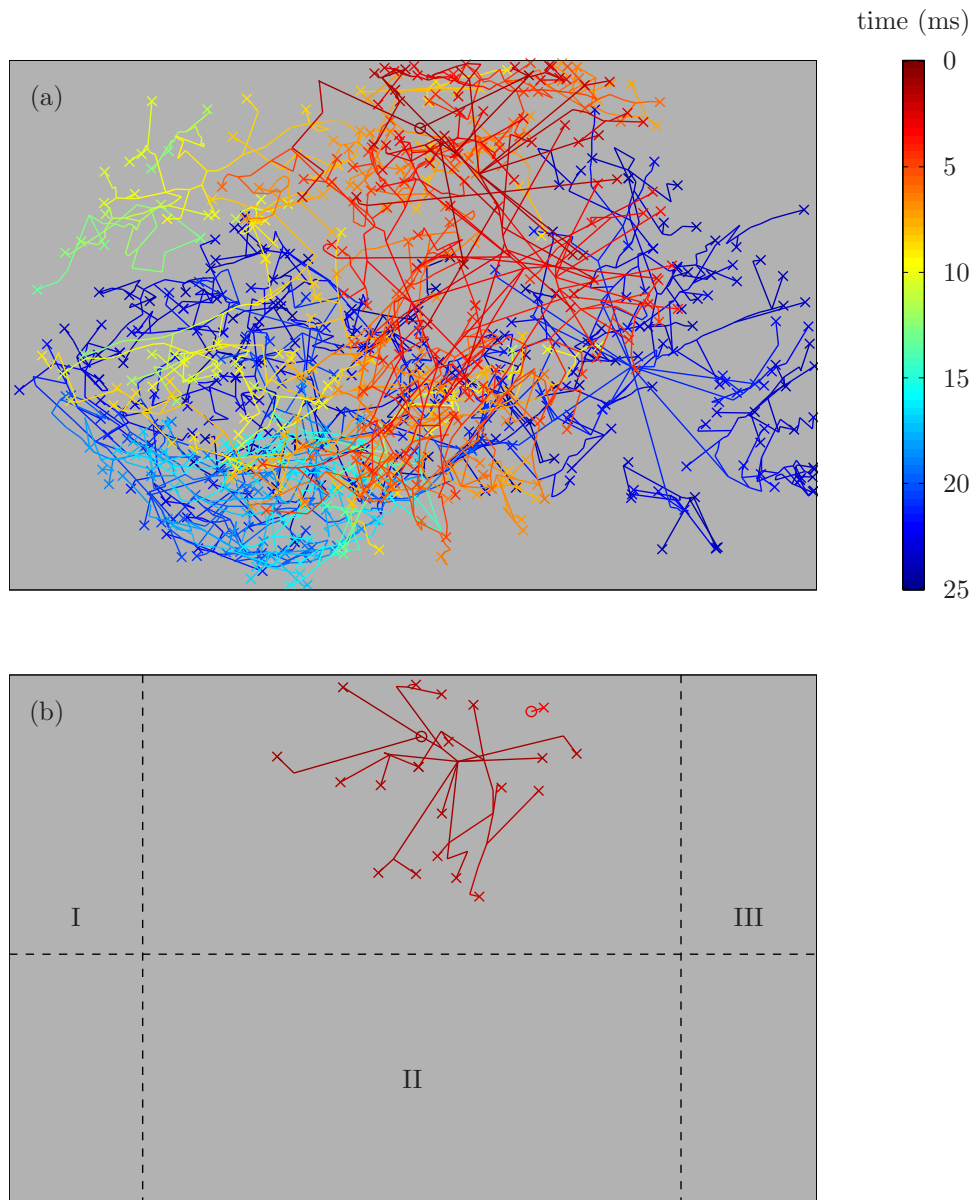


Fig. 6.6: Trajectory plots during 25 ms following spark: (a) safe success, recovery time = 24.6 ms; (b) unsafe failure, failure time = 5.4 ms.

flame has spread to occupy a significant proportion of the imaged area.

This result is in stark contrast to the typical unsafe trajectory plot displayed in Figure 6.6(b). Disintegration of the spark kernel occurs rapidly with little opportunity for the flame to spread upstream. This fast breakup results from the increased flow velocities and turbulence intensities generated at the unsafe test condition, and is reflected in the comparatively short unsafe failure times highlighted in Section 4.3.1.

Whereas all unsafe ignition failures occur in a similar manner, safe unsuccessful events fail in a variety of ways. Figure 6.7 consists of four trajectory plots each representing a different mode of safe failure. Although upstream flame motion is clearly required for successful relight, flame is also observed leaving the combustion chamber downstream. This convective loss of flame occurred during many safe tests, and was sometimes directly responsible for a failure. The four safe failure modes are in contrast to the unsafe failure in Figure 6.6(b) which involves disintegration and minimal propagation. The flame tracking program thus confirms the visual observations of failure categories reported earlier in Section 4.3.1.

The experiments of Ahmed et al. (2007a) identified three types of failures. Firstly, a spark followed by no indication of kernel initiation, which most resembles an unsafe failure in the current study, but could also broadly describe the safe failure mode in Figure 6.7(a). Secondly, flame initiation followed by downstream blow-off that is analogous to Figure 6.7(b). Thirdly, flame propagation and momentary stabilisation before extinction exemplified by Figure 6.7(d). The safe failure in Figure 6.7(c) represents a failure mode that has not been previously reported, namely a split in the initial kernel followed by downstream blow-off with simultaneous upstream propagation.

The relationship between flame placement and ignition success has been investigated by calculating the proportion of tests registering flame activity in three overlapping regions, labelled I, II, and III in Figure 6.6(b). Region I is an upstream

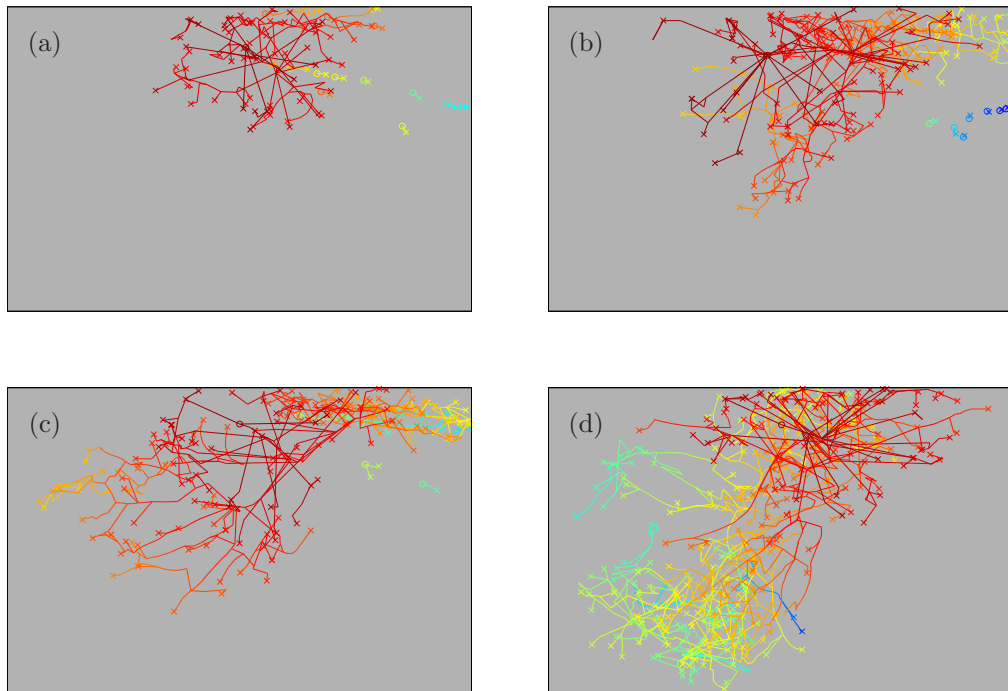


Fig. 6.7: Trajectory plots of safe failures: (a) rapid disintegration; (b) flame exit; (c) flame split; (d) no stabilisation at fuel injector.

portion of the image close to the fuel injector, region II contains all points below the injector centre-line, and region III is a downstream area close to the combustor exit. The statistics obtained from the tracking program are listed in Table 6.1.

The vast majority of safe, successful ignition events register flame in all three regions of the combustion chamber during the 25 ms following the spark. Most safe failures also exhibit activity below the centre-line and at the combustor exit. However, approximately half of these failed attempts display no evidence of flame at the fuel injector during the first 25 ms. This result indicates that although flame movement onto the injector face is a prerequisite for successful ignition, it does not guarantee success – at least 55% of failures occur having achieved this. Furthermore, as illustrated in Figure 6.8, the distribution of times required for flame to enter the fuel-injector region is similar for successful and unsuccessful ignition events. This

Table 6.1: Ignition activity in three regions of the combustor (see Figure 6.6(b)) during the 25 ms following the spark.

%	safe successes	safe failures	unsafe failures
I: fuel injector	100	55	3
II: below centre-line	99	89	44
III: combustor exit	86	85	74

implies that those unsuccessful flames that enter the injector region, are transported or propagate at a similar rate to flame kernels that are ultimately successful. Note the extremely broad range of these detection times, again indicating the highly stochastic nature of ignition.

At the unsafe condition, flame is observed below the fuel injector centre-line in less than half of the ignition attempts, and signal is recorded at the injector face in virtually no cases. Disintegration of the initial flame kernel occurs so rapidly at the unsafe set point that failure occurs before flame can be transported into regions I and II. However, the downstream convection of the early flame is sufficiently fast to generate signal at the exit during the majority of unsafe failures.

Insight into flame propagation is also provided by identifying the positions of last recorded flame activity during unsuccessful ignition events at the safe and unsafe conditions, as shown in Figure 6.9. This figure broadly reflects the results observed in the region analysis. In general, the safe failure occurs at a considerable distance from the igniter tip, indicating significant migration of the flame prior to extinction. At the unsafe condition, the failure points are closer to the igniter tip, and concentrated downstream of this point. At both conditions, a significant number of failures result from convective loss of flame out of the combustor exit, in the manner evident in Figure 6.7(b).

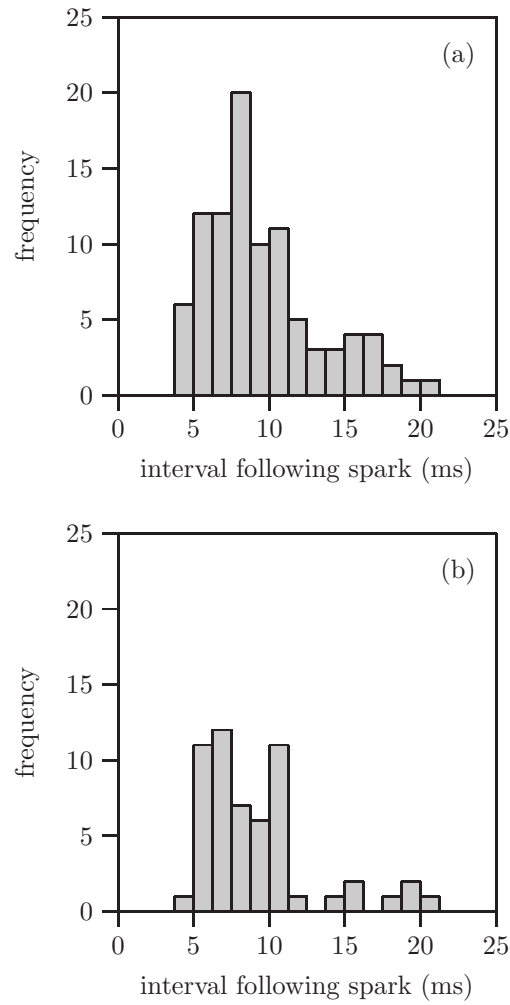


Fig. 6.8: Flame detection times in fuel-injector region at safe condition: (a) success; (b) failure.

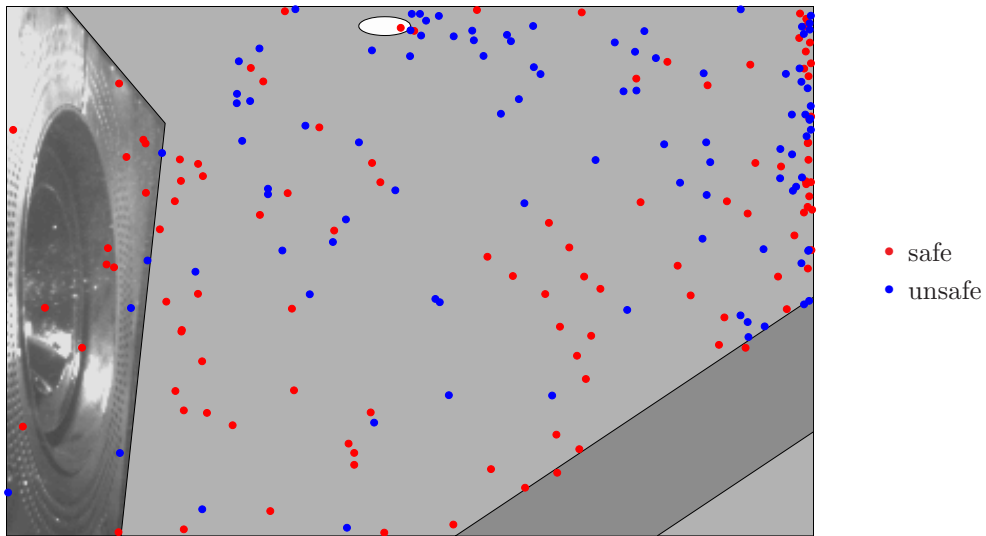


Fig. 6.9: Points of last activity during failed ignition events.

### 6.2.2 Flame size distributions

The flame tracking program records the size of all identified flame kernels. By summing the size of every kernel contained in a single image, the variation in recorded flame area during each ignition event can be identified. Note that the flame area extracted from each image does not correspond to the flame surface area, and also differs from the number of active pixels in the frame as the tracking program excludes all reflections. Scatter plots of flame area versus time are presented in Figure 6.10. The mean areas corresponding to safe successful, safe unsuccessful, and unsafe unsuccessful ignition trials, are plotted as green, red, and blue lines respectively. Note that the horizontal axis is logarithmic.

A large degree of scatter is apparent in the data, again highlighting significant variability in the ignition process. Despite this data spread, the mean plots illustrate several important features of relight flame development. Firstly, the pixel counts in the earliest recorded frames indicate that the three spark size distributions are indistinguishable. As discussed in Section 4.4, this implies that the spark kernel size

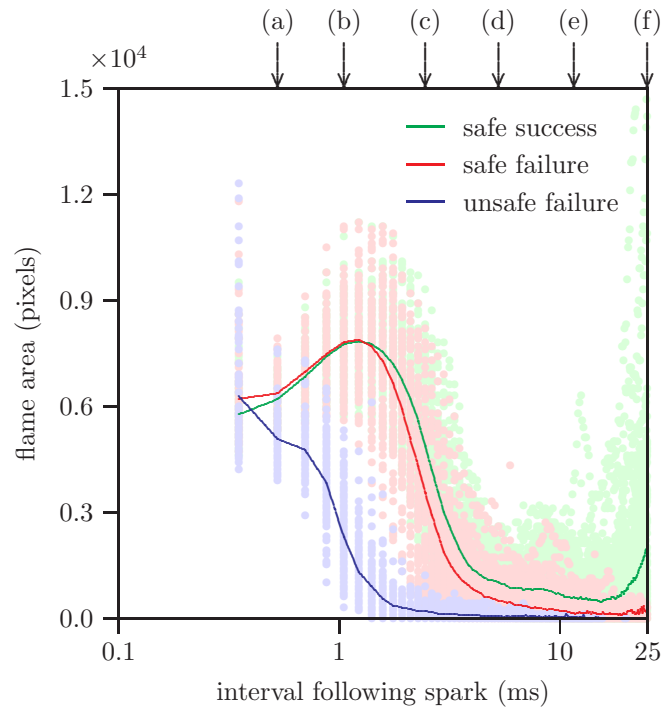


Fig. 6.10: Variation in imaged flame area with time. The labels above the plot indicate the timing of each sub-plot in Figure 6.11.

plays no role in determining ignition outcome, and is uninfluenced by the change in test conditions.

Immediately following the spark, the area occupied by flame increases at the safe condition. This is due to the hot kernel expanding and breaking apart. Rapid quenching of the spark at the unsafe set point causes the pixel count to decrease monotonically with time. After approximately 2 ms, the flame area at the safe condition begins to decrease rapidly, suggesting that the kernels fail to liberate sufficient heat to survive. At every point during this phase, flames that develop successfully demonstrate a larger mean flame area than their unsuccessful counterparts. This difference, however, is small compared to the sample standard deviation. The increase in mean, successful, flame area after approximately 20 ms indicates the onset of flame recovery. However, only 9% of recoveries occur during the 25 ms following the spark. The rapid flame growth generating these early recoveries therefore skews

the mean between 20 and 25 ms.

These observations are confirmed in Figure 6.11, where the distributions of individual kernel area are plotted at six intervals following the spark. These times were selected to ensure that the sub-figures are separated regularly in logarithmic time, as shown in Figure 6.10. At all intervals following the spark, very small kernels are present in significantly greater numbers than large kernels, requiring the use of a logarithmic vertical axis in Figure 6.11.

Figure 6.11(a) shows plots of the kernel size distributions extracted from the second frame following the spark. At both the safe and unsafe conditions, the histogram of kernel sizes created shortly following the spark features a Gaussian distribution of large kernels and a collection of small flame fragments. The evident disparity between the initial kernel size at the two set points can be attributed to early flame growth at the safe condition. This initial growth is also apparent in Figure 6.11(b) where the safe success and failure histograms are again indistinguishable. Breakup of the initial kernel into smaller flame bodies is clearly evident in the unsafe histogram. In Figure 6.11(c), the number of unsafe tests is starting to decrease due to ignition failures. At this point safe kernels are also exhibiting the breakup behaviour first observed at the unsafe condition (cf. Figure 6.11(b)). Figures 6.11(d) and 6.11(e) indicate that during the low intensity period before recovery (see Section 4.3.1), flame at the safe condition separates into a collection of small fragments. The kernel growth apparent in Figure 6.11(f) is associated with the early stages of recovery.

The fact that safe successes and failures are indistinguishable during the first 25 ms following the spark (corresponding to Figure 6.11(f)), suggests that ignition outcome is not determined by kernel size, but by another factor such as the flame path. This possibility is addressed below in Section 6.3.2.

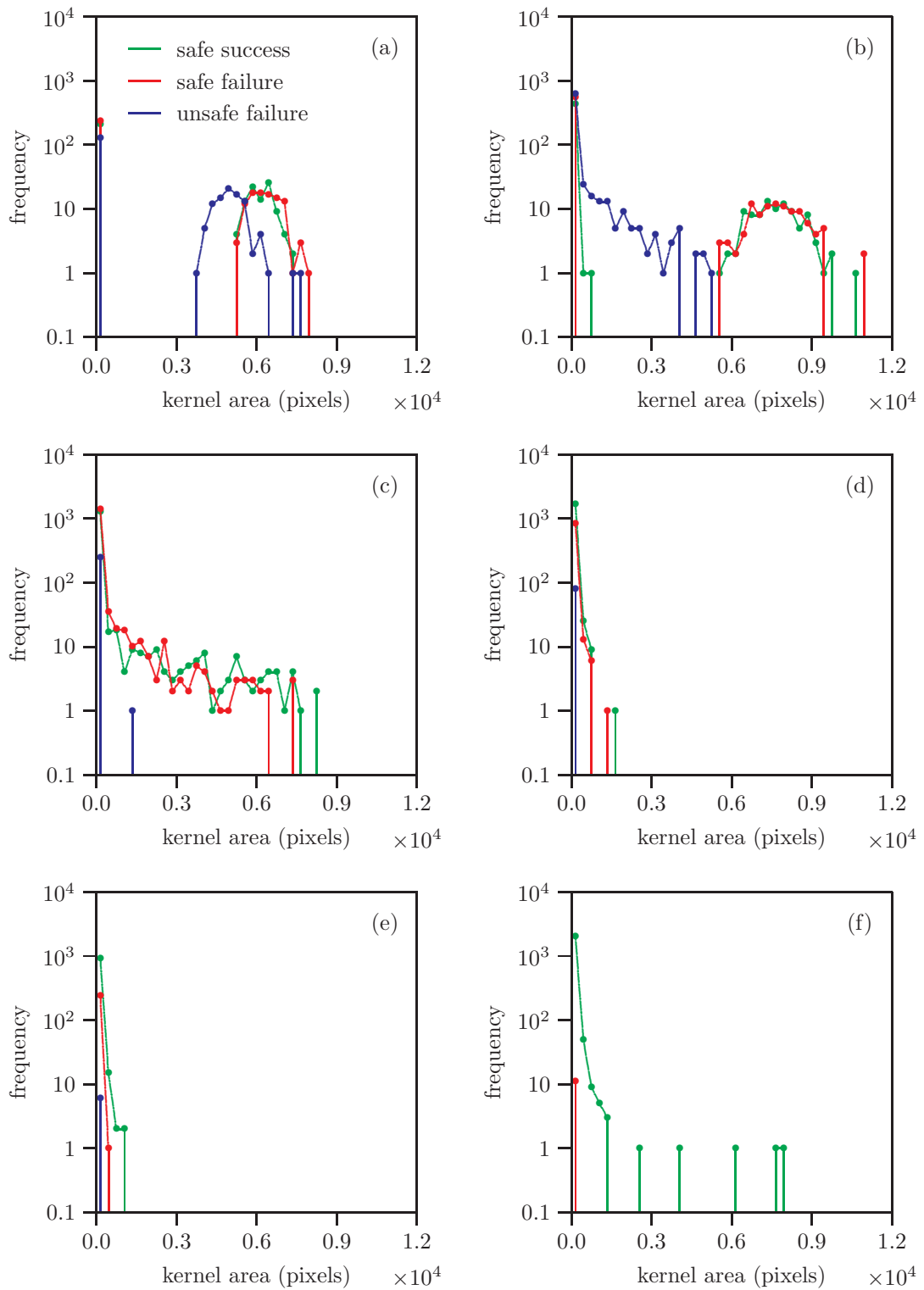


Fig. 6.11: Distributions of imaged kernel area. The timing of each sub-plot is indicated in Figure 6.10.

### 6.2.3 Spark kernel velocities

As noted earlier, the tracking software records the centroid locations of every flame body. It is therefore possible to estimate the spark kernel velocity by dividing the apparent displacement of the spark between the first and second frames by the time between them. Tables 6.2 and 6.3 present a comparison of the measured spark velocity and the CFD-predicted gas-phase velocity at the average spark-centroid location.

The spark velocity calculation accounts for the oblique viewing angle of the high-speed camera using the correction described in Appendix A. The measured axial velocities therefore describe spark motion in the central plane of the combustor sector (i.e. in the plane of the laser sheet). Though the camera cannot detect lateral motion of the flame, the CFD predictions of circumferential velocity have been included. These values demonstrate that while there is significant swirl, the axial component of velocity is dominant.

Table 6.2: Flame-centroid and CFD velocities at safe condition.

m/s	$u$	$v$	$w$
flame	21.1	-8.7	–
CFD	17.5	-2.8	-7.6

Table 6.3: Flame-centroid and CFD velocities at unsafe condition.

m/s	$u$	$v$	$w$
flame	32.8	-2.8	–
CFD	33.2	-4.3	-11.8

Notwithstanding the differences in geometry and boundary conditions (see Section 5.3), the stream-wise components of velocity show good agreement at both test conditions. However, the radial components of the flame centroid and CFD velocities are significantly different, with spark kernels at the safe condition descending

significantly faster than predicted by the CFD ( $-8.7$  m/s compared to  $-2.8$  m/s for the CFD). This disparity is caused by a difference in the mode of failure at the two set points. As previously observed, unsafe failure is caused by rapid disintegration of the spark body, with no evidence of kernel growth (see Section 6.2.2). At the unsafe set point the initial kernel therefore follows the flow, resulting in broad agreement with the CFD (see Table 6.3). In contrast, significant flame growth occurs at the safe condition. While upward growth of the kernel is prevented by the combustor outside wall, the flame is unconstrained from below. The centroid of flame activity therefore descends significantly faster than the flow field, as demonstrated in Table 6.2.

Ahmed and Mastorakos (2006) have demonstrated a correlation between the ignition probability of a turbulent non-premixed methane jet and the gas-phase velocity at the instant of the spark. Histograms of instantaneous axial velocity measured using LDA revealed that successful events generally occur at lower velocities than ignition failures. This result raises the question of whether ignition outcome in the altitude test facility depends on the local air velocity at the igniter tip.

From the results quoted above in Tables 6.2 and 6.3, it is reasonable to assume that the axial velocity of a spark kernel is equal to that of the local air-flow. Spark velocity information was extracted from recordings of successful and unsuccessful ignition events at the safe condition. Histograms of the axial component of velocity are shown in Figures 6.12(a) and 6.12(b). The mean axial velocity immediately following an unsuccessful spark is approximately 2 m/s greater than that measured during a successful ignition event. Furthermore, the distribution of failures is skewed towards higher velocities. This is illustrated in Figure 6.12(c), where the difference between the number of successes and failures associated with each velocity bin has been calculated, normalised to 100 samples, and plotted as a histogram. However, the difference between the mean velocities is less than both sample standard deviations, implying that the dependence of ignition outcome on axial velocity sug-

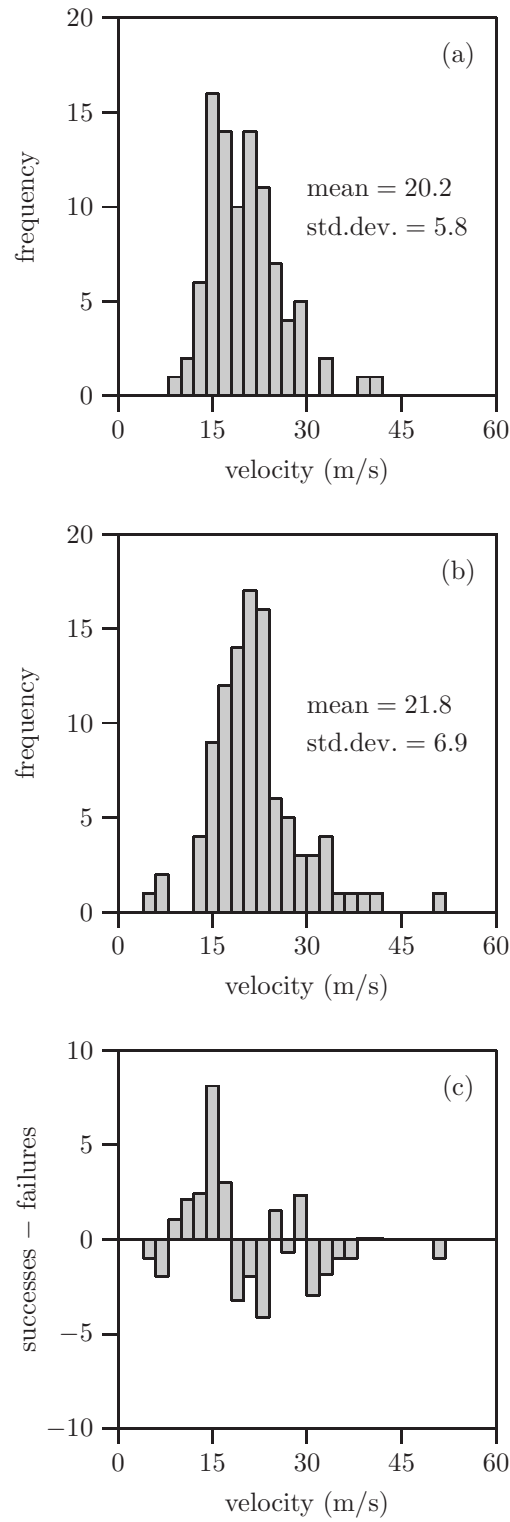


Fig. 6.12: Spark stream-wise velocity at safe condition: (a) success; (b) failure; (c) normalised difference between number of successes and failures.

gested by Figure 6.12(c) is relatively weak compared to that observed by Ahmed and Mastorakos (2006) for a methane jet flame. A more significant difference between successful and unsuccessful spark velocities may emerge for a sample size greater than the 100 or so tests analysed here.

## 6.3 Successful ignition

Employing the same method used to determine the spark kernel velocity, the velocities of flame kernels that emerge during the later stages of successful high-speed recordings have also been calculated. A key question to address is whether flame recovery occurs from a single location in the combustion chamber. The stabilised flame that is generated following successful ignition also fluctuates in a regular manner, and this frequency content is analysed in some detail. Measures to enhance ignition probability based on these observations are considered.

### 6.3.1 Flame velocities

Velocity data derived from the flame tracking program were spatially and temporally averaged, and constructed into a series of vector maps illustrating the general motion of the flame. Vector maps constructed from recordings of safe, successful ignition events, are presented in Figure 6.13. It is important to note that these vectors represent the three-dimensional motion of flame that may occupy any point across the width of the combustor. Ascribing a magnitude to these velocity vectors therefore requires the assumption that all flame motion is two-dimensional and occurs in the central plane of the combustor sector. Each vector represents the average velocity of all flame kernels in an imaged area  $3.8 \text{ mm} \times 3.8 \text{ mm}$ , during an interval of 0.88 ms. A velocity vector is displayed at locations where at least 10 flame kernels are contained in the averaging square. These vectors are colour-coded according to direction (see legend in Figure 6.14). The flame motion illustrated in these figures

is due to both convection of each kernel, and flame propagation relative to the cold gas phase.

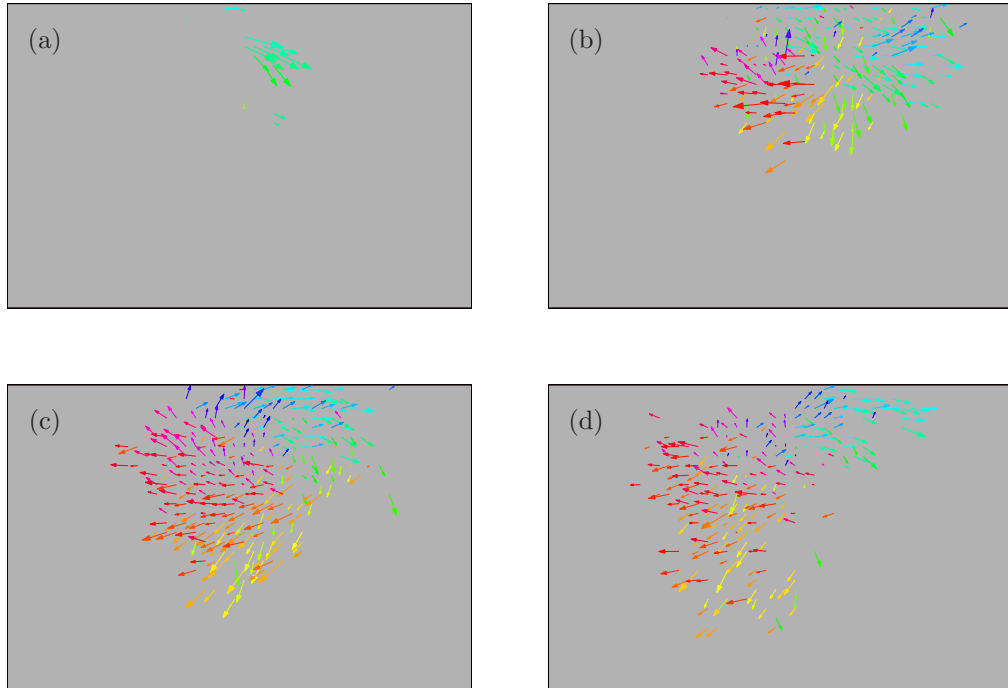


Fig. 6.13: Safe, successful, flame centroid velocity averaged over  $t \pm 0.4$  ms: (a)  $t = 0.8$ ; (b)  $t = 2.5$ ; (c)  $t = 4.3$ ; (d)  $t = 6.1$ . Vectors are coloured according to the direction legend illustrated in Figure 6.14.

Figure 6.13(a) illustrates the initial flame centroid velocities of all safe successes, averaged over the interval from 0.4 to 1.2 ms following the spark. The pocket of hot gas generated by the spark discharge moves downstream and towards the fuel-injector centre-line, at relatively high velocities. Shortly following the spark, successful ignition is characterised by upstream flame motion back towards the fuel-injector face, as shown in Figs. 6.13(b) to 6.13(d). Separate regions of upstream and downstream flame movement are clearly evident.

Figure 6.14 illustrates the flame centroid velocities extracted from all safe successful tests and averaged over the 25 ms following the spark. The plot is broadly

representative of flame motion in the combustion chamber as distinct regions of the chamber tend to register flame activity at different times (see Figure 6.13). The red vectors in Figure 6.14 demonstrate that flame moves predominantly upstream in the region to the left of the igniter, confirming the presence of a recirculation zone. Flame kernels situated downstream of the igniter move towards the combustor exit, as indicated by the light blue arrows.

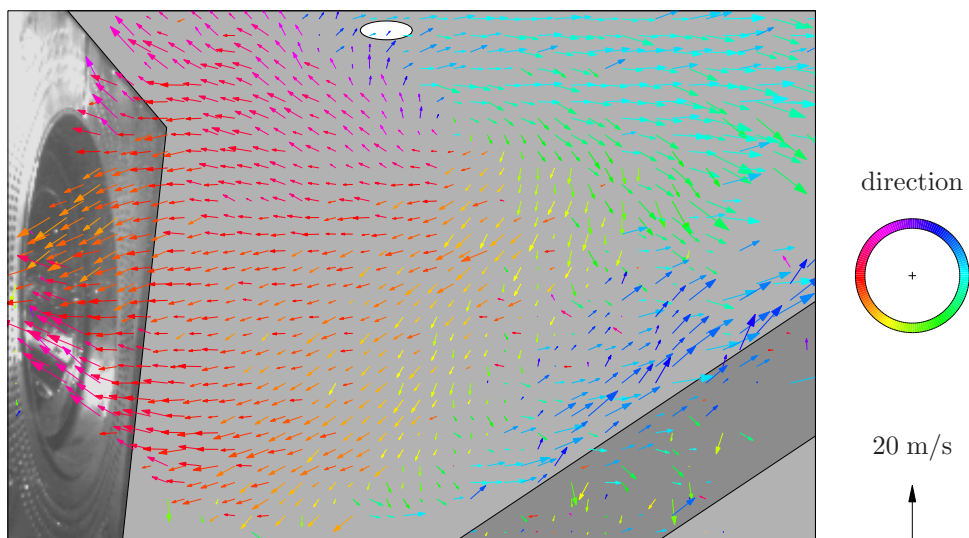


Fig. 6.14: Safe, successful, flame-centroid velocity averaged over 25 ms following spark.

A significant feature of the velocity vector map is the clockwise recirculation region that is observed below and downstream of the igniter tip. Recall from Section 5.3 that the cold LES predicts a similar recirculation zone, in this case located slightly upstream of the igniter. The fact that the same structure is observed in both the flame centroid velocity map (Figure 6.14) and the CFD flow field (Figure 5.19), suggests that flame motion is dominated by convection rather than propagation.

### 6.3.2 Recovery origin

The possibility that all safe successful ignition events share a common development path has been investigated by examining the spatial distribution of flame kernels during the lead up to recovery. In Figure 6.15, the total image intensity recorded during each successful ignition event is plotted versus time, with every data set shifted so that the recovery time coincides with  $t = 0$ . The mean intensity is plotted as a solid line, and increases as expected during recovery.

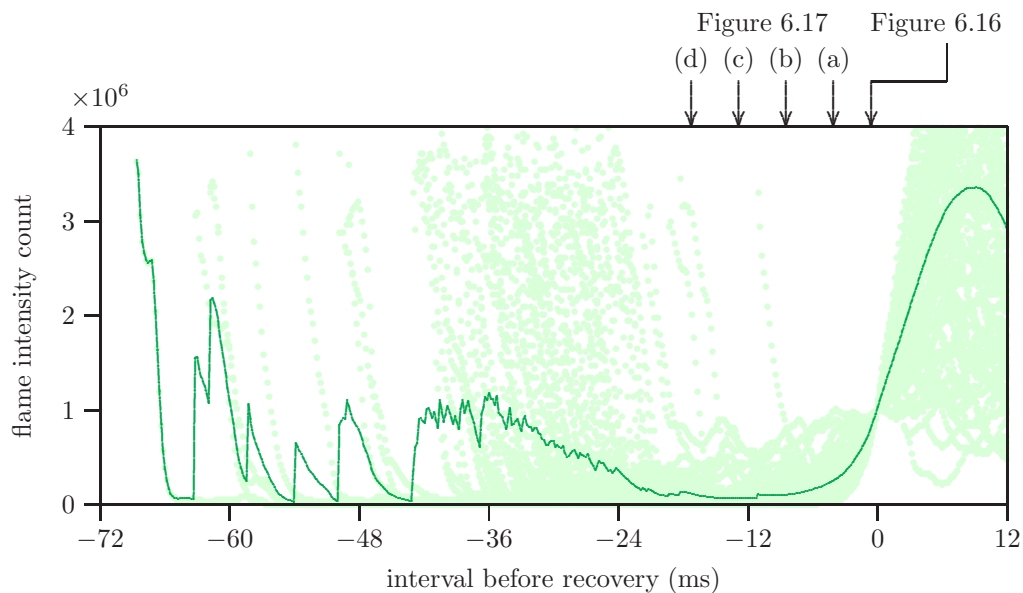


Fig. 6.15: Flame intensity variations during successful ignition referenced to recovery time. The labels above the plot indicate the timing of Figures 6.16 and 6.17.

As discussed in Chapter 4, the range of safe recovery times is large, extending from 11 to 69 ms. Consequently, when the interval before recovery is 69 ms, only one intensity trace contributes to the mean signal. Conversely, when the interval before recovery is 11 ms or less, intensity data from all of the safe successful recordings is used to calculate the mean. Between these times, an additional ignition event contributes to the mean intensity count whenever a spark occurs. Every new spark contaminates observations of the flame recovery process, and the analysis is therefore

limited to the first 20 ms before recovery, during which few sparks influence the mean intensity trace and kernel distribution.

The kernel number density map at the moment of recovery appears as shown in Figure 6.16. This contour map of average kernel number per unit area represents the probability of discovering flame activity at any point inside the combustor. Flame activity extends across virtually the entire chamber, with a concentration of kernels upstream of the igniter. From this density map it is not possible to determine whether the upstream concentration of flame bodies represents the source of recovery, or simply results from steady-state flame anchoring to the injector face following recovery. This uncertainty is due to the fact that a proportion of the recovery process occurs before the attributed recovery time (see Section 4.3.1).

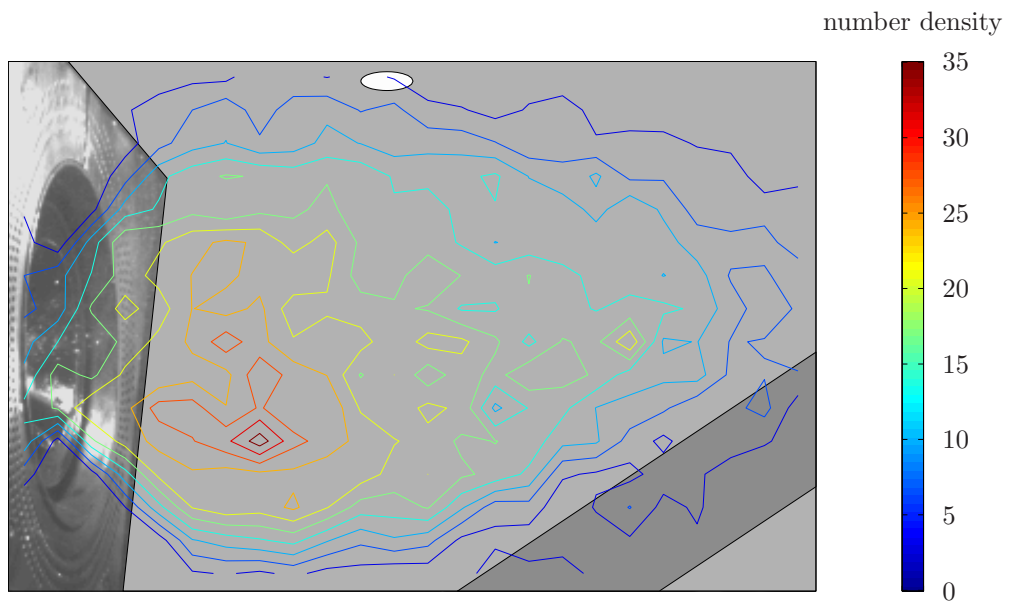


Fig. 6.16: Example of a kernel number density map averaged over  $t \pm 0.4$  ms, where  $t = -0.6$  ms (relative to recovery time).

It is therefore necessary to examine the kernel number density maps at earlier intervals as shown in Figure 6.17. Progressing backwards in time and presenting the density maps corresponding to the intervals indicated in Figure 6.15, it is apparent

that flame disappears from the majority of the combustor, but remains active in the region close to the injector face (see Figure 6.17(d)). This region can now be confidently identified as the origin of recovery.

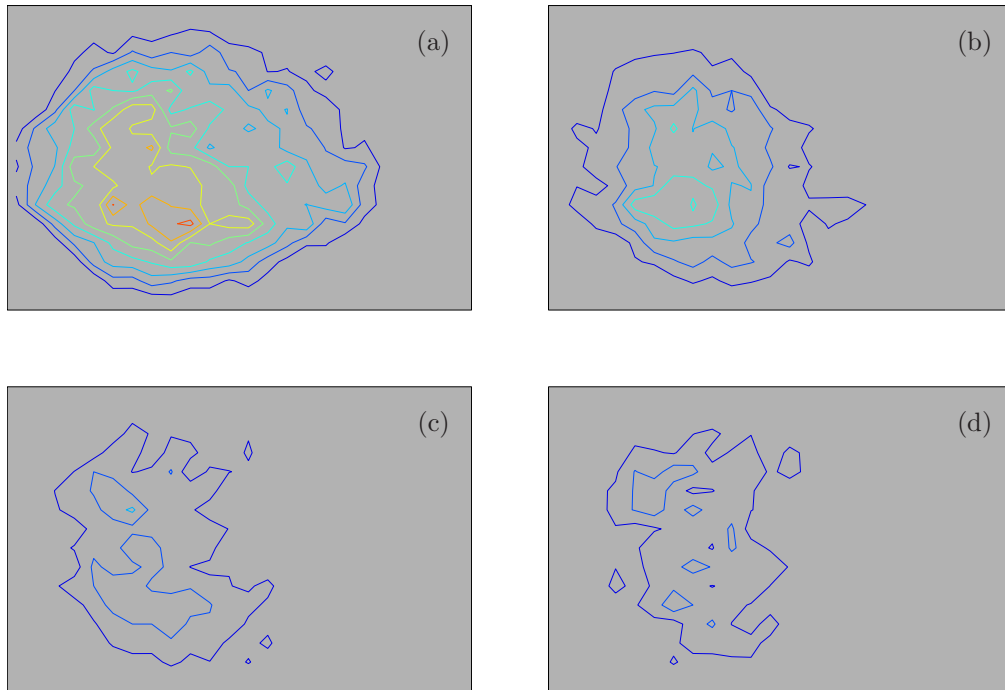


Fig. 6.17: Safe, successful kernel number density averaged over  $t \pm 0.4$  ms: (a)  $t = -4.1$ ; (b)  $t = -8.5$ ; (c)  $t = -12.9$ ; (d)  $t = -17.3$ . Contours are coloured according to the legend illustrated in Figure 6.16.

Having located a region that is favourable to recovery, it would be desirable to deliver developing kernels to this area of the combustor. At present this requires the migration of flame upstream from the igniter. Relocating the igniter tip slightly upstream of its current position may improve the likelihood of ignition success by reducing the distance that developing flame must move. As described in Section 2.4.4, this is supported by the work of Marchione et al. (2007, Sep), who observed that the likelihood of ignition was a strong function of the igniter's axial location.

### 6.3.3 Frequency content

Visual examination of the high-speed images acquired following flame recovery suggests that the stabilised flame fluctuates in a highly regular manner. This observation is confirmed in Figure 6.18, where the variation in total flame intensity during a single ignition event is plotted in blue. Following the recovery peak approximately 30 ms after the spark, the flame intensity count decreases, and begins to oscillate at approximately 50 Hz. These fluctuations are predominantly associated with cyclic changes in the total kernel area (red line in Figure 6.18), rather than variations in kernel luminosity. Note that the flame-tracking software was not used to perform this analysis, and the flame area is simply defined as the number of pixels in each frame with a count exceeding 10.

Fourier analysis of the total flame intensity signal indicates a strong peak in power at a frequency of 50.5 Hz, as shown in Figure 6.19. To minimise spectral leakage, a single Hamming window was applied to the time series before performing a discrete Fourier transform (DFT) (Press et al. 2007). The length of the DFT was set to 11400 points, thereby providing a spectral resolution of 0.5 Hz ( $f_s = 5.7$  kHz). Virtually all of the power is contained in frequencies less than 100 Hz. This is also true for many of the stabilised flame signals recorded following recovery. The Fourier analysis was repeated for the 88 successful ignition events that generate a continuous signal between 150 and 540 ms. All of these signals demonstrate maximum power spectral densities at frequencies less than or equal to 60 Hz. Indeed, half have their maximum at between 50 and 55 Hz. This fluctuation of steady-state flame may either be combustion-induced, or could result from a 50 Hz instability generated in the cold flow prior to the spark.

Thermoacoustic oscillations result from the positive feedback between pressure and heat release that can occur inside a gas turbine combustion chamber. Aircraft engine spray flames are susceptible to low-frequency ‘rumble’ instabilities at idle and sub-idle conditions (Zhu et al. 2001). Previous work by Eckstein et al. (2006) has

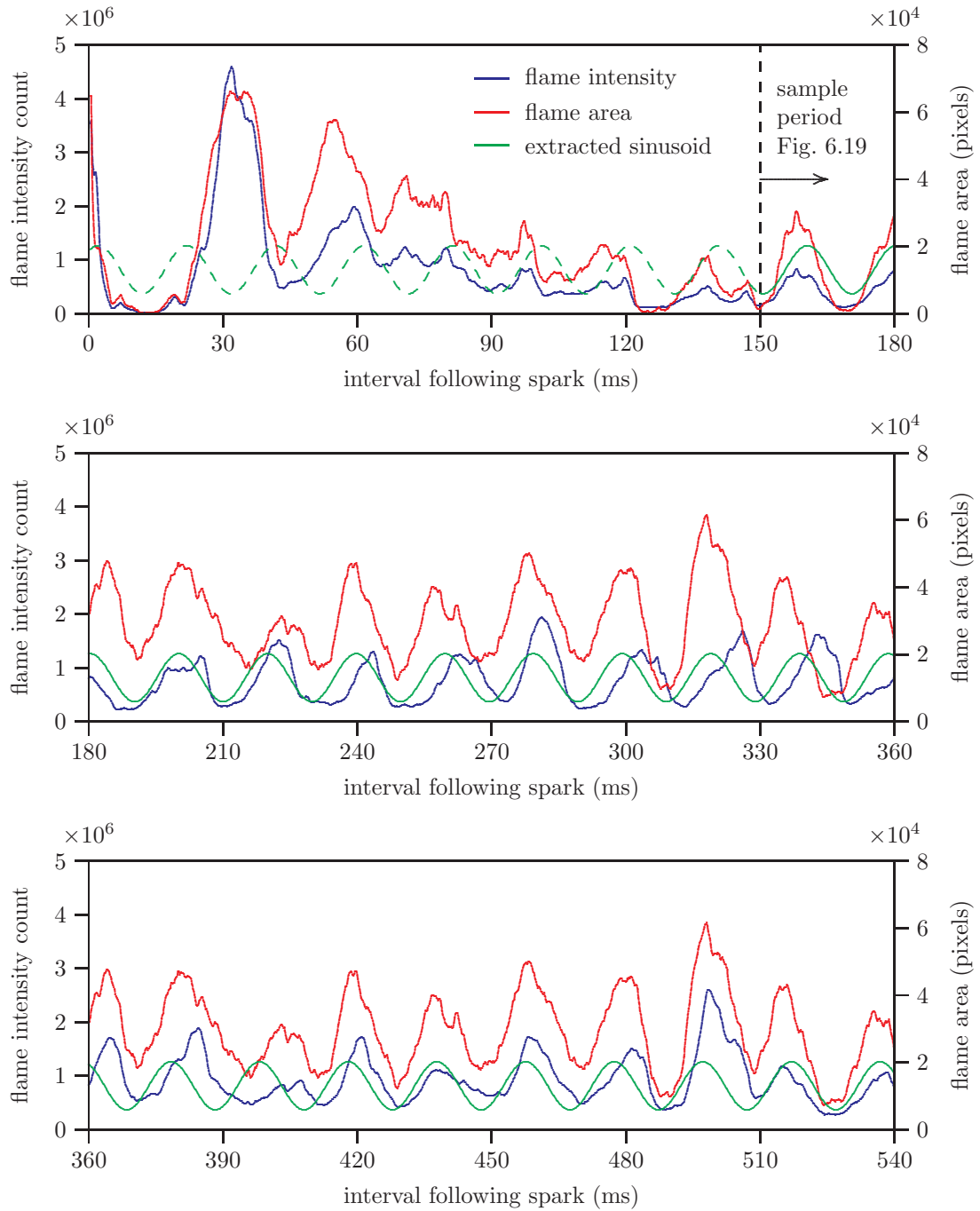


Fig. 6.18: Stabilised flame oscillations.

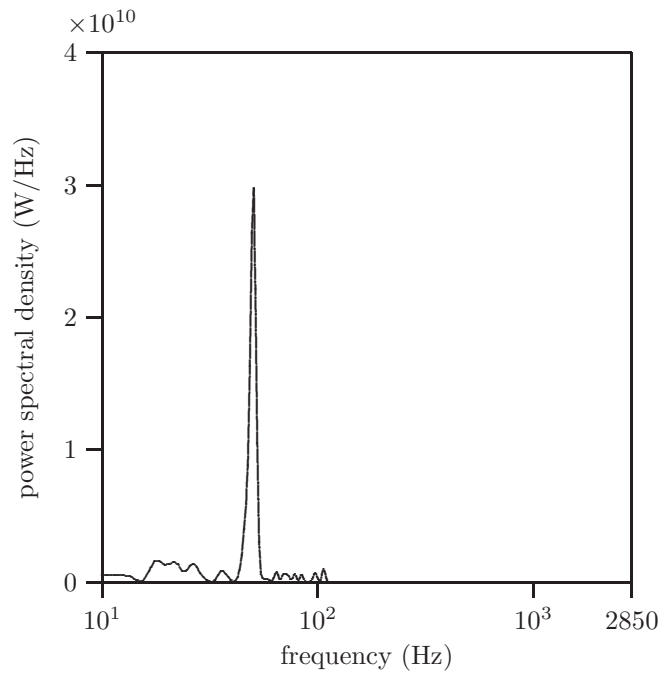


Fig. 6.19: Spectral analysis of measured flame intensity signal.

shown that these frequencies typically extend from 50 to 120 Hz, encompassing a large proportion of the frequencies observed in the present study.

The observed fluctuations may alternatively be caused by a cold flow instability. A previous study of isothermal flow through a fuel injector has demonstrated that induced swirl can generate instabilities at low frequencies (Carrotte and Batchelor-Wylam 2003). If such a cold instability is causing the flame oscillations in the present study then the spark timing assumes great importance, as earlier results suggest that the local axial velocity below the igniter tip is skewed towards lower values for successful ignition (see Section 6.2.3).

The existence of a cold flow instability has been investigated by extracting the most powerful frequency component contained in the flame intensity signal, and extrapolating back to find its phase relative to the spark (at  $t = 0$ ). This process is illustrated in Figure 6.18, and the resulting phase information extracted from all test data is collated in Figure 6.20. There appears to be no consistent relationship

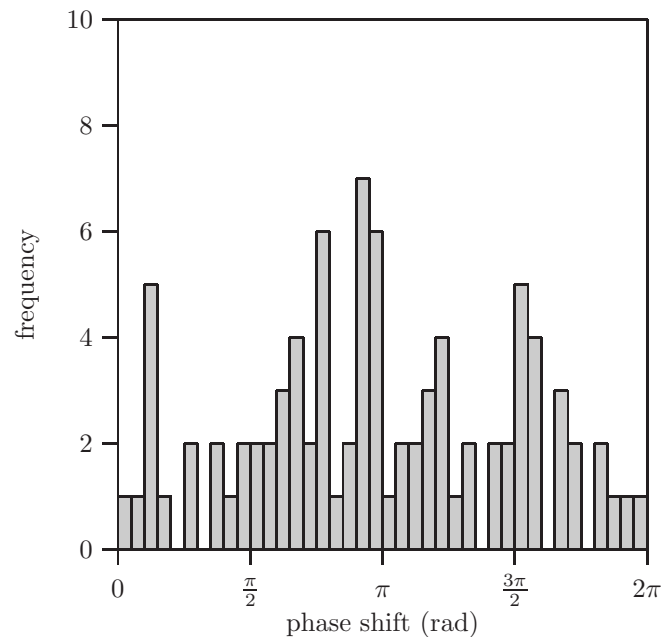


Fig. 6.20: Phase shift of stabilised flame oscillations relative to spark.

between the phase of the spark relative to the most powerful intensity sinusoid, and the number of successful events. However, many more samples would be required to draw a definitive conclusion.

## 6.4 CFD comparison

Several features of the CFD simulation can be compared with the results produced by the flame tracking program. As already noted in Section 6.2.3, the CFD predictions of axial velocity below the igniter tip are in good agreement with the observed kernel motion. Three streamlines generated by the cold LES and passing through this region are illustrated in Figure 6.21. The mean spark centroid is indicated by an open white circle. These streamlines terminate on the side of the computational domain, indicating that the circumferential component of velocity is significant compared to the axial velocity. Swirl produced by the fuel injector may therefore heavily influence the relight process, possibly generating the yellow and green downward

vectors evident in Figure 6.14. Though not measured during this study, the out-of-plane velocity could be identified using a stereoscopic imaging approach such as that described by Cheung and Zhang (2006).

A well-developed recirculation zone is apparent in the upstream portion of the combustion chamber, bounded by the red line in Figure 6.21. This provides an explanation for the observed upstream motion of flame kernels at the safe set point. Furthermore, the recovery origin identified in Section 6.3.2 is fully contained inside this recirculation zone. It is reasonable to conclude that the combustor flow patterns tend to promote stabilisation of flame at the injector face provided that the air mass flow rate does not prohibit kernel survival.

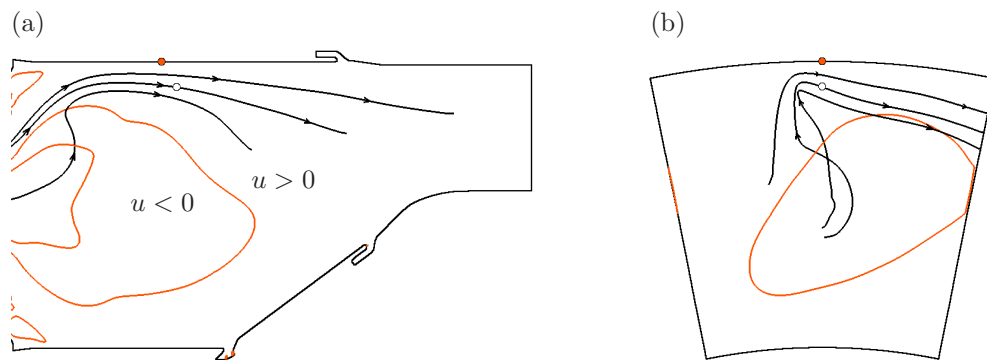


Fig. 6.21: CFD streamlines passing below the igniter tip at the safe test condition: (a) side view; (b) rear view. The igniter tip and mean spark centroids are represented by red and white filled circles respectively. The zero contours of axial velocity are also shown in red.

# Chapter 7

## Conclusion

In this study experiments have been performed in a high-altitude test facility to increase understanding of ignition and flame development during relight of a LDI combustor. The distribution of kerosene fuel inside the combustion chamber was measured using PLIF, and high-speed images of flame emission were recorded during numerous ignition tests. The analysis of the experimental results has provided important insights into the relight process, and these are summarised below.

### 7.1 Operation of test facility

Testing was conducted at two conditions, designated ‘safe’ and ‘unsafe’ to indicate the relative probability of ignition. The sole difference between these conditions was the larger air mass flow rate at the unsafe set point (see Table 3.1). Roughly one in five sparks produced successful relight at the safe condition whereas ignition was never achieved at the unsafe condition. During an ignition test, sparks were generated at 1.3 Hz and were halted following successful relight at the safe condition, and after 10 sparks at the unsafe condition. Several hundred PLIF images of cold fuel distribution were recorded, and around 100 ignition tests were conducted at each set point, during which PLIF and flame images were recorded simultaneously.

### 7.1.1 Apparatus modifications

Fuel and flame imaging at altitude restart conditions are made extremely difficult by the large quantities of fuel deposited on the internal surfaces of the combustion chamber. Contamination of the laser sheet optics would cause significant attenuation of the excitation wavelength, while fuel on the combustor side windows would reduce the resolution of both PLIF and flame images. In addition, simultaneous fuel and flame imaging requires careful timing control, that must also handle large variations in the spark-to-spark interval. The following modifications were implemented to overcome these difficulties:

- Design and installation of a beam delivery apparatus. Laser light was directed from an optical table onto a laser periscope and sheet expansion assembly mounted on the ATF, which projected the sheet into the combustion chamber from behind the fuel injector.
- Addition of several protective air purges. These purges were introduced at the bottom periscope mirror, sheet expansion lens, and combustor window, to prevent contamination of the optical surfaces by dust, condensation, and liquid fuel.
- Development of a timing and data acquisition system. Signals from the laser, igniter current probe, and a photodiode registering successful ignition events, were used to control the acquisition of images with the PLIF and high-speed cameras.

### 7.1.2 Apparatus characterisation

The success or failure of ignition is influenced not only by the random nature of the relight process, but also by bulk variations in the experimental boundary conditions. Fluctuations in the ATF operating conditions, laser energy, and spark parameters were quantified in Chapter 4, together with the timescales of flame development. These preliminary investigations into the performance of the apparatus led to the following findings:

- The spatial energy profile of the laser sheet did not have the expected Gaussian distribution. Asymmetric features of the profile were identified that later influenced correction of the PLIF images.
- Flame activity during an ignition test was characterised by a low-intensity delay period prior to recovery. The length of this delay period varied significantly, as did the failure time of unsuccessful sparks, indicating that recovery is a random event not governed by the conditions at the instant of the spark discharge.
- The spark was relatively consistent. Measured values of spark size, current, and luminosity showed no correlation with ignition outcome and were not significantly affected by the test conditions.
- At the safe condition, ignition probability increased until the fifth spark and remained constant thereafter, indicating that the early sparks were not independent events. It is likely that the observed variation in spark performance is associated with large amounts of fuel deposited on the igniter tip, that may be displaced by the action of early sparks.

## 7.2 Main findings of fuel and flame imaging

It was shown in Chapter 5 that the laser sheet was not significantly attenuated by the kerosene droplets, and the PLIF signal remained strong even along the downstream edge of the image. Nevertheless, the PLIF images required significant corrections, the largest of which accounted for the non-uniform laser energy profile. Initial analysis avoided the need for correction by considering a small area close to the middle of the sheet. The full mean images were later corrected and analysed.

- In the small area of interest, the mean PLIF signal was higher at the unsafe condition than at the safe set point. This is due to improved atomisation at the unsafe condition leading to high concentrations of fuel in suspension. The larger droplets produced at the safe condition tend to be deposited on the combustor walls rather than remaining in the CRZ.
- The local AFR was rich at the safe condition and richer still at the unsafe condition. This may contribute to consistent ignition failure at the unsafe condition, though excessive turbulent strain is also important.
- PLIF images were successfully acquired in the presence of flame and showed negligible interference from PAH fluorescence and flame emission. The effect of flame was to significantly reduce the overall PLIF signal, but a base level of signal remained due to the presence of large burning droplets.
- Corrected mean images of cold fuel distribution were compared to CFD simulations of the gas-phase flow, confirming that small kerosene droplets are trapped in the CRZ. Virtually no fuel is found in a channel of fast-moving air between the CRZ and the igniter tip.

The analysis of the high-speed flame recordings was discussed in Chapter 6. An image processing algorithm was developed to analyse the motion and breakup of flame during relight, allowing the construction of a single flame trajectory plot

representing each ignition attempt. This program recorded the size and centroid velocity of every flame kernel, and led to the following conclusions:

- Trajectory plots revealed several modes of relight failure including the rapid disintegration, blow-off, and unsuccessful stabilisation modes identified by Ahmed et al. (2007a) for a laboratory scale burner. An additional failure mode was also identified that consisted of a split in the initial kernel followed by simultaneous downstream blow-off and upstream propagation towards the fuel injector.
- Initial kernel velocities were found to be in broad agreement with CFD predictions of the cold flow. Flow patterns apparent from measurements of average flame velocity were also observed in the CFD results, demonstrating that flame motion is dominated by convection rather than propagation.
- A recovery origin was identified close to the fuel injector face. Since the size of flame kernels decreased continuously from shortly following the spark until recovery, successful ignition may be characterised by the ability of flame kernels to survive long enough to reach the fuel injector face.
- Stabilised flame fluctuated sinusoidally at a rate of approximately 50 Hz. This may be a combustion-induced instability, or the fluctuation may already be present in the cold flow.

## 7.3 Recommendations for future work

A major finding of this study is that kerosene PLIF can be used to map the fuel distribution inside a LDI combustor operating under altitude relight conditions. As described above, several insights into the relight process have been provided by the combined imaging of fuel and flame. Further useful information would be obtained by simply repeating the experiment to increase the sample size of data available. For example, supplementary measurements would confirm whether there is indeed a correlation between low air velocity at the igniter tip and successful ignition outcome, as suggested in Section 6.2.3. In addition, the possibility of a periodic cold flow instability has important consequences for relight performance, and this could again be confirmed by analysing a larger data set.

### 7.3.1 Measures to improve LDI relight performance

The results of the current work suggest the following methods of enhancing relight performance:

- Increase the spark energy. The flame tracking results suggest that increasing the initial kernel size may improve the probability of successful flame propagation.
- Move the igniter upstream. Ignition probability may be increased by reducing the distance that a developing flame kernel must travel to reach the recovery origin.
- Improve atomisation at the safe condition. This would assist survival of the flame kernels as finer droplets evaporate more easily and feed the flame.
- Adjust the spark timing to take advantage of periodic velocity fluctuations that may exist in the cold flow.

### 7.3.2 Further investigations

The apparatus developed during this study can be used to apply other laser diagnostic techniques to examine relight processes inside the ATF. In addition, the experiment techniques employed could be improved in several respects. The following are promising avenues for future research:

- Use the double-pulse functionality of the laser to perform droplet or gas-phase particle image velocimetry (PIV).
- Mie-scattering measurements of liquid fuel distribution could be made using the second laser harmonic at 532 nm.
- Improve the beam energy distribution correction by diverting a small fraction of the laser light to a reference dye cell during testing. This would also allow each PLIF image to be corrected for shot-to-shot energy fluctuations.
- Provide improved timing control of the spark to increase the probability of obtaining fuel distribution images during flame development.
- Conduct high-speed measurements of emissions from a specific radical produced in the flame reaction zone e.g. OH, CH, or C<sub>2</sub>. This would be achieved by placing an appropriate optical filter in front of an intensified CCD camera, and may also eliminate the loss of signal experienced during some successful ignition events.

# Appendices

# Appendix A

## Viewing Angle Corrections

The imaging of a calibration square is illustrated schematically in Figure A.1. The blue square,  $PQRS$ , represents a calibration target and lies in the plane of the laser sheet. The centre of this square is at the origin. The red parallelogram is the projection of square  $PQRS$  onto the  $x$ - $y$  plane, and the camera observes this plane at right angles.

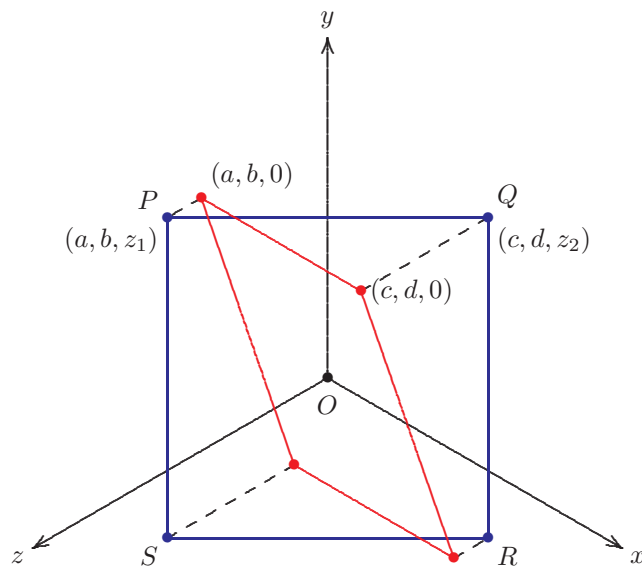


Fig. A.1: Rotated square.

The coordinates  $(a,b)$  and  $(c,d)$  are measured from the image of the calibration target. The unknowns are  $z_1$  and  $z_2$ . As the square is centred at the origin, points  $P$  and  $Q$  are equidistant from  $O$  and thus

$$a^2 + b^2 + z_1^2 = c^2 + d^2 + z_2^2 . \quad (\text{A.1})$$

Also, the vectors  $\overrightarrow{OP}$  and  $\overrightarrow{OQ}$  are perpendicular, so

$$z_1 z_2 = -(ac + bd) . \quad (\text{A.2})$$

Substituting (A.2) into (A.1) gives

$$z_1^4 + (a^2 + b^2 - c^2 - d^2)z_1^2 - (ac + bd)^2 = 0. \quad (\text{A.3})$$

Eq. (A.3) is a quadratic in  $z_1^2$  that is easily solved. The positive root is chosen, since  $z_1^2 \geq 0$  is required. The choice of sign for  $z_1$  is arbitrary as the viewing correction is the same for the two orientations of the square that generate the same image. Suppose, without loss of generality, that point  $P$  is projected forward in the positive  $z$ -direction, as depicted in Figure A.1. Then,

$$z_1 = \frac{1}{\sqrt{2}} \left[ - (a^2 + b^2 - c^2 - d^2) + \sqrt{(a^2 + b^2 - c^2 - d^2)^2 + 4(ac + bd)^2} \right]^{1/2}, \quad (\text{A.4})$$

and the value of  $z_2$  follows from Eq. (A.2).

Having identified the coordinates of  $P$ ,  $Q$ ,  $R$ , and  $S$  as described above, let us define a normal vector to the square

$$\mathbf{n} = \overrightarrow{OP} \times \overrightarrow{OQ} . \quad (\text{A.5})$$

Note that the plane of the square contains all points  $\mathbf{r}$  such that  $\mathbf{n} \cdot \mathbf{r} = 0$ .

Suppose that a vector  $(u^*, v^*)$  is measured in an image captured by either camera. Then from Eq. (A.5) the  $z$ -component,  $w^*$ , of this vector is given by

$$w^* = \frac{u^*(dz_1 - bz_2) + v^*(az_2 - cz_1)}{(ad - bc)} . \quad (\text{A.6})$$

It remains to find the components of  $(u^*, v^*, w^*)$  in the plane of the square. Let us call this vector  $(u, v)$ . A suitable coordinate system for the square is obtained from the midpoints of QR and PQ respectively

$$\mathbf{i}_s = \frac{\overrightarrow{OQ} + \overrightarrow{OR}}{|\overrightarrow{OQ} + \overrightarrow{OR}|}, \quad \mathbf{j}_s = \frac{\overrightarrow{OP} + \overrightarrow{OQ}}{|\overrightarrow{OP} + \overrightarrow{OQ}|}. \quad (\text{A.7})$$

Taking the dot product of  $(u^*, v^*, w^*)$  with each of the unit vectors  $\mathbf{i}_s$  and  $\mathbf{j}_s$  gives the following result

$$\begin{bmatrix} u \\ v \end{bmatrix} = \mathbf{M} \begin{bmatrix} u^* \\ v^* \end{bmatrix} = \begin{bmatrix} M_{11} & M_{12} \\ M_{21} & M_{22} \end{bmatrix} \begin{bmatrix} u^* \\ v^* \end{bmatrix}, \quad (\text{A.8})$$

where the elements of the transformation matrix are

$$M_{11} = \frac{\left[ c - a + \frac{(dz_1 - bz_2)(z_2 - z_1)}{(ad - bc)} \right]}{\left[ (c - a)^2 + (d - b)^2 + (z_2 - z_1)^2 \right]^{1/2}}, \quad (\text{A.9})$$

$$M_{12} = \frac{\left[ d - b + \frac{(az_2 - cz_1)(z_2 - z_1)}{(ad - bc)} \right]}{\left[ (c - a)^2 + (d - b)^2 + (z_2 - z_1)^2 \right]^{1/2}}, \quad (\text{A.10})$$

$$M_{21} = \frac{\left[ a + c + \frac{(dz_1 - bz_2)(z_1 + z_2)}{(ad - bc)} \right]}{\left[ (a + c)^2 + (b + d)^2 + (z_1 + z_2)^2 \right]^{1/2}}, \quad (\text{A.11})$$

$$M_{22} = \frac{\left[ b + d + \frac{(az_2 - cz_1)(z_1 + z_2)}{(ad - bc)} \right]}{\left[ (a + c)^2 + (b + d)^2 + (z_1 + z_2)^2 \right]^{1/2}}. \quad (\text{A.12})$$

The coordinates required to evaluate Eqs. (A.9) to (A.12) were extracted from an image of the calibration target recorded by each camera. The image of this square was not a true parallelogram due to perspective effects, optical distortion by the lens, and uncertainties in the coordinates caused by resolution limits. These effects

were removed by averaging the distance between the origin and opposite vertices. The coordinates corresponding to the viewing positions of the two cameras are listed in Table A.1. The matrix elements calculated from these coordinates are presented in Table A.2. Having identified these elements, Eq. (A.8) can be used to map vectors in the sheet plane to the camera images, and vice versa.

Table A.1: Calibration target vertex coordinates (see Figure A.1)

	$a$	$b$	$c$	$d$
PLIF camera	-427.5	409.0	427.0	412.0
high-speed camera	-86.0	83.0	80.5	82.0

Table A.2: Viewing angle transformation matrices and scaling factors.

	$M_{11}$	$M_{12}$	$M_{21}$	$M_{22}$	mm/pixel
PLIF camera	1.000	0.001	-0.004	1.041	0.08
high-speed camera	1.016	0.034	0.006	1.025	0.45

Table A.2 indicates that the required corrections are comparatively small for both camera viewing angles i.e.  $M_{ij}$  is approximately equal to the identity matrix. A scaling factor was required to convert between units of pixels and millimetres. This was obtained by applying Eq. (A.8) to a vector in the reference image joining the centre of the calibration square to one of its vertices. As the true length of this line is known, the scale factor (mm/pixel) follows. The scaling factors corresponding to the two viewing angles are also listed in Table A.2.

# Appendix B

## Geometry of Laser Sheet

### B.1 Lens calculations

The 8 mm diameter beam produced by the laser is formed into a sheet by four planar lenses, arranged as illustrated in Figure B.1. If the dimensions and refractive index of each lens are known, then the dimensions of the resulting elliptical beam cross-section can be evaluated at every point along the optical axis using a first-order analysis (Hecht 2002).

If it is assumed that the convergence and divergence angles are small ( $\leq 10^\circ$ ), then the paraxial approximation is valid. In this case, the refraction of incoming light rays can be considered to occur in one of two principal planes, the choice of which depends on the direction of beam propagation through the optic. For a general singlet lens, the distance from these principal planes to their respective focal points is known as the effective focal length

$$f = \left[ (n - 1) \left( \frac{1}{R_1} - \frac{1}{R_2} + \frac{d(n - 1)}{nR_1R_2} \right) \right]^{-1}, \quad (\text{B.1})$$

where  $n$  is the refractive index of the lens material,  $R_1$  and  $R_2$  are the radii of curvature of the first and second lens surfaces respectively, and  $d$  is the lens thickness at the optical axis. It is generally more useful to state the position of the focal point relative to a lens vertex. The front focal distance (FFD) is defined as the distance

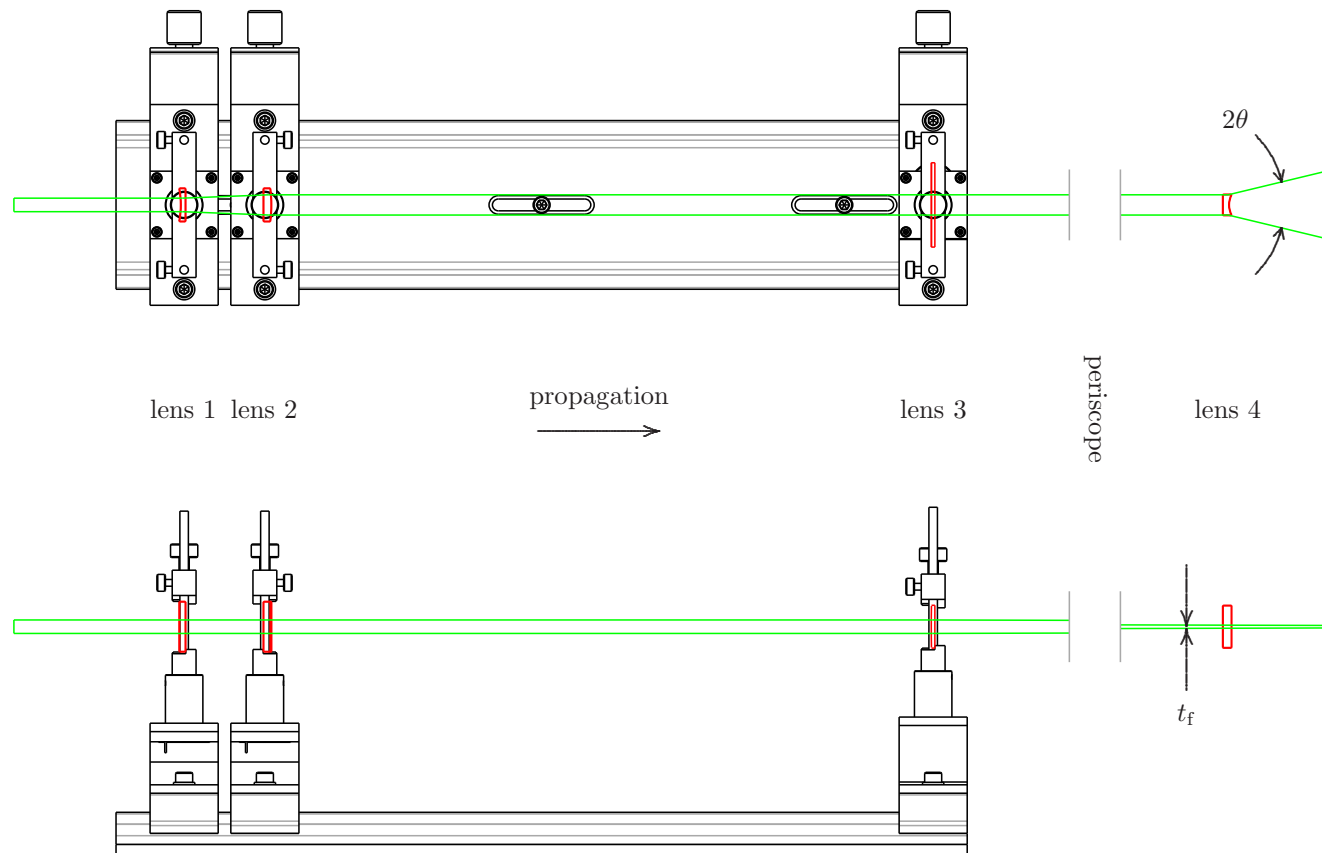


Fig. B.1: Sheet-formation optics. Lenses 1, 2, and 3 are mounted on the optical table (see Figure 3.4). Lens 4 is installed in the sheet expansion assembly (see Figure 3.6).

from the front focal point to the vertex of the first lens surface

$$\text{FFD} = f \left[ 1 + \frac{d(n-1)}{nR_2} \right]. \quad (\text{B.2})$$

The back focal distance (BFD) is defined as the distance from the vertex of the second lens surface to the rear focal point

$$\text{BFD} = f \left[ 1 - \frac{d(n-1)}{nR_1} \right]. \quad (\text{B.3})$$

Eqs. (B.1), (B.2), and (B.3) can be used to calculate the effective focal length, FFD, and BFD of each sheet-formation lens, and these results are listed in Table B.1. Note that all four lenses are manufactured from ultraviolet-grade fused silica with a refractive index of 1.500 at 266 nm. With these focal distances and a knowledge

Table B.1: Dimensions and focal distances of sheet-formation lenses. All dimensions are given in mm.

lens number	$R_1$	$R_2$	$d$	$f$	FFD	BFD
1	-50.9	$\infty$	3.1	-101.9	-101.9	-103.9
2	$\infty$	-76.3	5.0	152.7	149.4	152.7
3	704	$\infty$	2.1	1408.9	1408.9	1407.5
4	$\infty$	12.7	4.0	-25.4	-28.1	-25.4

of the separation between optics, simple geometry can be used to establish the width and thickness of the beam at critical points along the optical axis. The cross-sectional dimensions of the beam at the appropriate principal plane of each lens are listed in Table 3.2.

Referring to Figure B.1, lenses 1 and 2 expand the beam by a fixed amount horizontally relative to the surface of the optical table. This finite expansion is achieved by positioning the optics so that the front focal point of lens 2 coincides with the back focal point of lens 1. Following this alignment, the width of the beam after expansion is simply the ratio of the effective focal lengths multiplied by the

original beam width

$$w_2 = \frac{f_2}{f_1} w_1 = \frac{152.7}{101.9} \times 8 = 12.0 \text{ mm.} \quad (\text{B.4})$$

Lens 3 has a comparatively long focal length that generates a gradual thinning of the beam as it passes through the periscope and into the combustion chamber. The change in thickness per unit distance along the optical axis generated by lens 3 is

$$m = \frac{t_1}{f_3} = \frac{8}{1408.9} = 5.68 \times 10^{-3}. \quad (\text{B.5})$$

The distance from the principal plane of lens 3 to the focal point of lens 4 can be extracted from a CAD model of the experimental apparatus. The sheet thickness at the focal point of lens 4 is then

$$t_f = t_1 - mx = 8 - [(5.68 \times 10^{-3})(1064.8)] = 2.0 \text{ mm.} \quad (\text{B.6})$$

Lens 4 expands the laser beam into a sheet. The beam height at the principal plane is relatively large compared to the effective focal length, producing a divergence at the upper and lower beam extent of  $27.3^\circ$ . This comparatively large expansion invalidates the paraxial assumption, and the effective focal length must be modified to account for curvature of the principal plane. Then

$$|f'_4| = \sqrt{f_4^2 - \left(\frac{w_4}{2}\right)^2} = \sqrt{(-25.4)^2 - \left(\frac{12.0}{2}\right)^2} = 24.7 \text{ mm.} \quad (\text{B.7})$$

Based on this modified effective focal length, the divergence half angle of the sheet is

$$\theta = \tan^{-1} \left( \frac{w_4/2}{|f'_4|} \right) = \tan^{-1} \left( \frac{12.0/2}{24.7} \right) = 0.24 \text{ rad.} \quad (\text{B.8})$$

Note that this angle corresponds to the unclipped sheet extent (see Section 3.2.4).

## B.2 Frontal area calculation

A correction must be applied to the PLIF images to account for changes in the cross-section of the sheet as it passes through the combustor. As illustrated in

Figure B.2, the propagating laser front forms a series of curved surfaces, composed of points equidistant from the focal axis of the lens. Neglecting non-uniformities in the beam energy profile, the irradiance is constant throughout a frontal surface, and proportional to the surface area. The correction factor required at a general point,  $P$ , is therefore proportional to the area of the frontal surface containing  $P$ . A general expression for this frontal area is therefore required.

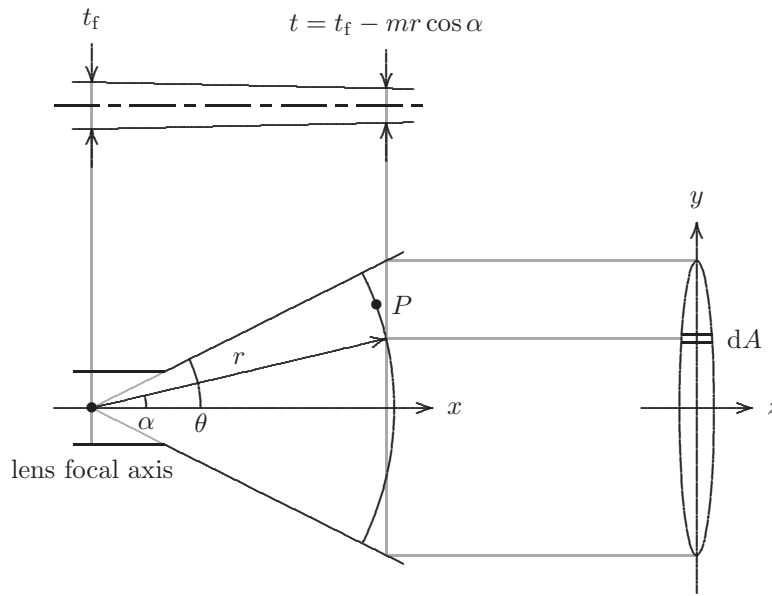


Fig. B.2: Laser sheet geometry.

Point  $P$  is situated distance  $r$  from the focal axis of the lens. An ellipse is formed by taking a cross-section of the sheet perpendicular to the horizontal axis. The elliptical cross-section passing through the end of a radial line, length  $r$ , inclined at angle  $\alpha$ , has the outline

$$\frac{y^2}{(r \cos \alpha \tan \theta)^2} + \frac{4z^2}{t^2} = 1. \quad (\text{B.9})$$

If  $y = r \sin \alpha$  then

$$\frac{\tan^2 \alpha}{\tan^2 \theta} + \frac{4z^2}{t^2} = 1. \quad (\text{B.10})$$

The maximum thickness of the elliptical cross-section is

$$t = t_f - mr \cos \alpha. \quad (\text{B.11})$$

The area of the surface element  $dA$  is

$$dA = 2zr \, d\alpha. \quad (\text{B.12})$$

Combining Eqs. (B.10), (B.11), and (B.12), and integrating yields

$$A = 2r \int_0^\theta (t_f - mr \cos \alpha) \sqrt{1 - \frac{\tan^2 \alpha}{\tan^2 \theta}} \, d\alpha. \quad (\text{B.13})$$

Numerical evaluation of Eq. (B.13) provides the frontal area at every imaged point in the sheet. The values of  $m$ ,  $t_f$ , and  $\theta$ , have been identified in Eqs. (B.5), (B.6), and (B.8) respectively.

From Eqs. (B.10) and (B.11), the sheet thickness at a specific radial and angular location is

$$z = \frac{t_f - mr \cos \alpha}{2} \sqrt{1 - \frac{\tan^2 \alpha}{\tan^2 \theta}}. \quad (\text{B.14})$$

This equation is used in Section 5.2.2 to identify the sheet thickness correction factor at every point in the sheet.

# References

- Advisory Council for Aeronautics Research in Europe (2002). Strategic Research Agenda 1, Volume 2.
- Aggarwal, S. K. (1998). A review of spray ignition phenomena: present status and future research. *Prog. Energy Combust. Sci.* *24*, 565–600.
- Ahmed, S. F., R. Balachandran, T. Marchione, and E. Mastorakos (2007a). Spark ignition of turbulent nonpremixed bluff-body flames. *Combust. Flame* *151*, 366–385.
- Ahmed, S. F., R. Balachandran, and E. Mastorakos (2007b). Measurements of ignition probability in turbulent non-premixed counterflow flames. *Proc. Combust. Inst.* *31*, 1507–1513.
- Ahmed, S. F. and E. Mastorakos (2006). Spark ignition of lifted turbulent jet flames. *Combust. Flame* *146*, 215–231.
- Allouis, C., F. Beretta, and A. Amoresano (2008). Experimental study of lean pre-mixed prevaporized combustion fluctuations in a gas turbine burner. *Combust. Sci. Technol.* *180*, 900–909.
- Anacleto, P., M. V. Heitor, and A. L. N. Moreira (1996). Mean and turbulent flowfields in a model RQL gas-turbine combustor. *Exp. Fluids* *22*, 153–164.
- Arnold, A., R. Bombach, B. Kappeli, and A. Schlegel (1997). Quantitative measurements of OH concentration fields by two-dimensional laser-induced fluorescence. *Appl. Phys. B* *64*, 579–583.

- Arnold, A., F. Dinkelacker, T. Heitzmann, P. Monkhouse, M. Schäfer, V. Sick, J. Wolfrum, W. Hentschel, and K.-P. Schindler (1992). DI diesel engine combustion visualised by combined laser techniques. *Proc. Combust. Inst.* *24*, 1605–1612.
- ASTM (2008). Standard ASTM D1655-08.
- Atkins, D. L., J. S. Ervin, and L. Shafer (2005). Experimental studies of jet fuel viscosity at low temperatures, using a rotational viscometer and an optical cell. *Energy Fuels* *19*, 1935–1947.
- Ballal, D. R. (2004, Jan). private communication, Kettering Laboratories, Room 462, 300 College Park, Dayton, Ohio, 45469-0140, United States.
- Ballal, D. R. and A. H. Lefebvre (1975). The influence of spark discharge characteristics on minimum ignition energy in flowing gases. *Combust. Flame* *24*, 99–108.
- Ballal, D. R. and A. H. Lefebvre (1977a). Flame quenching in turbulent flowing gaseous mixtures. *Proc. Combust. Inst.* *16*, 1689–1698.
- Ballal, D. R. and A. H. Lefebvre (1977b). Ignition and flame quenching in flowing gaseous mixtures. *Proc. R. Soc. Lond. A* *357*, 163–181.
- Ballal, D. R. and A. H. Lefebvre (1978a). Ignition and flame quenching of quiescent fuel mists. *Proc. R. Soc. Lond. A* *364*, 277–294.
- Ballal, D. R. and A. H. Lefebvre (1978b). Ignition of liquid fuel sprays at subatmospheric pressures. *Combust. Flame* *31*, 115–126.
- Ballal, D. R. and A. H. Lefebvre (1979). Ignition and flame quenching of flowing heterogeneous fuel-air mixtures. *Combust. Flame* *35*, 155–168.
- Ballal, D. R. and A. H. Lefebvre (1981). A general model of spark ignition for gaseous and liquid fuel-air mixtures. *Proc. Combust. Inst.* *18*, 1737–1746.
- Bazile, R. and D. Stepowski (1995). Measurements of vaporized and liquid fuel

- concentration fields in a burning spray jet of acetone using planar laser induced fluorescence. *Exp. Fluids* 20, 1–9.
- Beck, J. E., A. H. Lefebvre, and T. R. Koblisch (1991). Airblast atomization at conditions of low air velocity. *J. Propul. Power* 7, 207–212.
- Becker, J. and C. Hassa (2003). Liquid fuel placement and mixing of generic aero-engine premix module at different operating conditions. *J. Eng. Gas Turbines Power* 125, 901–908.
- Black, J. D. (1995). Investigation of fluorescence from bulk liquid fuel excited by Nd:YAG laser harmonics. Technical Report RR(OH)1443, Rolls-Royce Applied Science Laboratory, Derby, UK.
- Blanc, M. V., P. G. Guest, G. von Elbe, and B. Lewis (1947). Ignition of explosive gas mixtures by electric sparks. I. Minimum ignition energies and quenching distances of mixtures of methane, oxygen, and inert gases. *J. Chem. Phys.* 15, 798–802.
- Blanc, M. V., P. G. Guest, G. von Elbe, and B. Lewis (1949). Ignition of explosive gas mixtures by electric sparks. III. Minimum ignition energies and quenching distances of mixtures of hydrocarbons and ether with oxygen and inert gases. *Proc. Combust. Inst.* 3, 363–367.
- Blomeyer, M., B. Krautkremer, D. K. Hennecke, and T. Doerr (1999). Mixing zone optimization of a rich-burn/quick-mix/lean-burn combustor. *J. Propul. Power* 15, 288–295.
- Boileau, M., S. Pascaud, E. Riber, B. Cuenot, L. Y. M. Gicquel, T. Poinso, and M. Cazalens (2008a). Investigation of two-fluid methods for large eddy simulation of spray combustion in gas turbines. *Flow Turbul. Combust.* 80, 291–321.
- Boileau, M., G. Staffelbach, B. Cuenot, T. Poinso, and C. Bérat (2008b). LES of an ignition sequence in a gas turbine engine. *Combust. Flame* 154, 2–22.

- Boudier, G., L. Y. M. Gicquel, T. Poinso, D. Bissières, and C. Bérat (2007). Comparison of LES, RANS and experiments in an aeronautical gas turbine combustion chamber. *Proc. Combust. Inst.* 31, 3075–3082.
- Braig, W., H. Schulte, and C. Riegler (1999). Comparative analysis of the windmilling performance of turbojet and turbofan engines. *J. Propul. Power* 15, 326–333.
- Brandt, M., K. O. Gugel, and C. Hassa (1997). Experimental investigation of the liquid fuel evaporation in a premix duct for lean premixed and prevaporized combustion. *J. Eng. Gas Turbines Power* 119, 815–821.
- Burgoyne, J. H. and L. Cohen (1954). The effect of drop size on flame propagation in liquid aerosols. *Proc. R. Soc. Lond. A* 225, 375–392.
- Burland, G. N., K. A. Goreham, and R. J. Taunt (1984). The development of the high energy surface discharge spark igniter. In *29th International Gas Turbine Conference Exhibit*. ASME.
- Caines, B. N., R. A. Hicks, and C. W. Wilson (2001, Jul). Influence of sub-atmospheric conditions on the performance of an airblast atomiser. In *37th AIAA/ASME/SAE/ASEE Joint Propulsion Conference*, Salt Lake City, Utah.
- Calcote, H. F., C. A. Gregory Jr., C. M. Barnett, and R. B. Gilmer (1952). Spark ignition, effect of molecular structure. *Indus. Eng. Chem.* 44, 2656–2662.
- Canepa, E., P. D. Martino, P. Formosa, M. Ubaldi, and P. Zunino (2006). Unsteady aerodynamics of an aeroengine double swirler lean premixing prevaporizing burner. *J. Eng. Gas Turbines Power* 128, 29–39.
- Cant, R. S. and E. Mastorakos (2008). *An Introduction to Turbulent Reacting Flows*. London: Imperial College Press.
- Carrotte, J. F. and C. Batchelor-Wylam (2003). Characterisation of the instantaneous velocity and mixture field issuing from a lean-premixed module (LPM). In *Proc. ASME Turbo Expo*, Volume 2, New York, pp. 489–498. ASME.

- Çengel, Y. A. and M. A. Boles (1998). *Thermodynamics: An Engineering Approach* (3rd ed.). New York: McGraw-Hill.
- Chakraborty, N., E. Mastorakos, and R. S. Cant (2007). Effects of turbulence on spark ignition in homogeneous mixtures: A direct numerical simulation (DNS) study. *Combust. Sci. Technol.* 179, 293–317.
- Cheung, K. Y. and Y. Zhang (2006). Stereo imaging and analysis of combustion process in a gas turbine combustor. *Meas. Sci. Technol.* 17, 3221–3228.
- Ciajolo, A., A. Tregrossi, R. Barbella, R. Ragucci, B. Apicella, and M. De Joannon (2001). The relation between ultraviolet-excited fluorescence spectroscopy and aromatic species formed in rich laminar ethylene flames. *Combust. Flame* 125, 1225–1229.
- Cohen, H., G. F. C. Rogers, and H. I. H. Saravanamuttoo (1996). *Gas Turbine Theory* (4th ed.). Harlow, Essex: Longman.
- Coordinating Research Council (2004). Handbook of aviation fuel properties. Technical report.
- Danis, A. M., I. Namer, and N. P. Cernansky (1988). Droplet size and equivalence ratio effects on spark ignition of monodisperse n-heptane and methanol sprays. *Combust. Flame* 74, 285–294.
- Dietrich, D. L., N. P. Cernansky, M. B. Somashekara, and I. Namer (1990). Spark ignition of a bidisperse, n-decane fuel spray. *Proc. Combust. Inst.* 23, 1383–1389.
- Dowling, A. P. and S. Hubbard (2000). Instability in lean premixed combustors. *Proc. Inst. Mech. Eng. Part A* 214, 317–332.
- Eckstein, J., E. Freitag, C. Hirsch, and T. Sattelmayer (2006). Experimental study on the role of entropy waves in low-frequency oscillations in a RQL combustor. *J. Eng. Gas Turbines Power* 128, 264–270.
- European Aviation Safety Agency (2003). Certification Specification CS-E 910.

- Federal Aviation Administration (2000). Federal Aviation Regulation, Section 25.903.
- Gaydon, A. G. (1974). *The Spectroscopy of Flames* (2nd ed.). London: Chapman and Hall.
- Gaydon, A. G. and H. G. Wolfhard (1970). *Flames - Their Structure Radiation and Temperature* (3rd ed.). London: Chapman and Hall.
- Glassman, I. (1996). *Combustion* (3rd ed.). San Diego: Academic Press.
- Goddard, C. and M. Zedda (2007, Jul). private communication, Combustion Systems Department, Rolls-Royce plc., PO Box 31, Derby, DE24 8BJ, UK.
- Goodger, E. M. (1994). *An Overview of Jet Fuel Supply and Quality*. Norwich: Landfall Press.
- Gupta, A. K., M. S. Ramavajjala, J. Chomiak, and N. Marchionna (1991). Burner geometry effects on combustion and  $\text{NO}_x$  emission characteristics using a variable geometry swirl combustor. *J. Propul. Power* 7, 473–480.
- Hardalupas, Y., C. H. Liu, and J. H. Whitelaw (1994). Experiments with disk stabilised kerosene-fuelled flames. *Combust. Sci. Technol.* 97, 157–191.
- Hartung, G., J. Hult, C. F. Kaminski, J. W. Rogerson, and N. Swaminathan (2008). Effect of heat release on turbulence and scalar-turbulence interaction in premixed combustion. *Phys. Fluids* 20, 035110.
- Hecht, E. (2002). *Optics* (4th ed.). Harlow, Essex: Addison-Wesley.
- Hill, P. G. and C. R. Peterson (1992). *Mechanics and Thermodynamics of Propulsion* (2nd ed.). Addison-Wesley.
- Hornak, J. P. (Ed.) (2002). *Encyclopedia of Imaging Science and Technology*, Volume 1. New York: John Wiley & Sons.
- Ikeda, Y., N. Yamada, T. Nakajima, M. Ohta, M. Inada, and S. Mandai (2002).

- Spray combustion characteristics in a highly pressurized swirl-stabilized combustor. *Proc. Combust. Inst.* 29, 853–859.
- International Civil Aviation Organisation (1993). *Manual of the ICAO Standard Atmosphere* (3rd ed.). ICAO (CD-ROM).
- International Civil Aviation Organisation (2006). Annexes to the Convention on International Civil Aviation, Annex 16 – Environmental Protection, Volume II – Aircraft Engine Emissions.
- James, S., J. Zhu, and M. S. Anand (2006). Large-eddy simulations as a design tool for gas turbine combustion systems. *AIAA J.* 44, 674–686.
- Kaminski, C. F., J. Hult, M. Aldén, S. Lindenmaier, A. Dreizler, U. Maas, and M. Baum (2000). Spark ignition of turbulent methane/air mixtures revealed by time-resolved planar laser-induced fluorescence and direct numerical simulations. *Proc. Combust. Inst.* 28, 399–405.
- Kampa, M. and E. Castanas (2008). Human health effects of air pollution. *Environ. Pollut.* 151, 362–367.
- Kerrebrock, J. L. (1977). *Aircraft Engines and Gas Turbines*. Cambridge, Massachusetts: The MIT Press.
- Klein, M., N. Chakraborty, K. W. Jenkins, and R. S. Cant (2006). Effects of initial radius on the propagation of premixed flame kernels in a turbulent environment. *Phys. Fluids* 18, 055102.
- Koehler, W. (1970). Thermal lensing in a Nd:YAG laser rod. *Appl. Opt.* 9, 2548–2553.
- Koh, H., J. Jeon, D. Kim, Y. Yoon, and J.-Y. Koo (2003). Analysis of signal attenuation for quantification of a planar imaging technique. *Meas. Sci. Technol.* 14, 1829–1838.
- Kohse-Höinghaus, K. and J. B. Jeffries (Eds.) (2002). *Applied Combustion Diagnostics*. New York: Taylor and Francis.

- Kolner, B. H. (1991). Intensity noise enhancement in the half-wave plate/polarizer attenuator. *Opt. Lett.* *16*, 784–786.
- Krüger, V., C. Wahl, R. Hadeff, K. P. Geigle, W. Stricker, and M. Aigner (2005). Comparison of laser-induced incandescence method with scanning mobility particle sizer technique: The influence of probe sampling and laser heating on soot particle size distribution. *Meas. Sci. Technol.* *16*, 1477–1486.
- Lefebvre, A. H. (1989). *Atomization and Sprays*. New York: Hemisphere.
- Lefebvre, A. H. (1995). The role of fuel preparation in low-emission combustion. *J. Eng. Gas Turbines Power* *117*, 617–654.
- Lefebvre, A. H. (1999). *Gas Turbine Combustion* (2nd ed.). Philadelphia: Taylor and Francis.
- Lewis, B. and G. von Elbe (1961). *Combustion, Flames, and Explosions of Gases* (2nd ed.). New York: Academic Press.
- Li, Y. G. and R. L. Hales (2003). Steady and dynamic performance and emissions of a variable geometry combustor in a gas turbine engine. *J. Eng. Gas Turbines Power* *125*, 961–971.
- Locke, R. J., Y. R. Hicks, R. C. Anderson, and M. M. Zaller (1998). Optical fuel injector patternation measurements in advanced liquid-fueled, high pressure, gas turbine combustors. *Combust. Sci. Technol.* *138*, 297–311.
- Löfström, C., H. Kaaling, and M. Aldén (1996). Visualization of fuel distributions in premixed ducts in a low-emission gas turbine combustor using laser techniques. *Proc. Combust. Inst.* *26*, 2787–2793.
- Lorenzetto, J. E. and A. H. Lefebvre (1977). Measurements of drop size on a plain-jet airblast atomiser. *AIAA J.* *15*, 1006–1010.
- Marchione, T., S. F. Ahmed, R. Balachandran, and E. Mastorakos (2007, July). Effectiveness of localised spark ignition in recirculating n-heptane spray flames.

- In *21st International Colloquium on the Dynamics of Explosions and Reactive Systems*, Poitiers, France.
- Marchione, T., S. F. Ahmed, and E. Mastorakos (2007, Sep). Ignition behaviour of recirculating spray flames using multiple sparks. In *5th Mediterranean Combustion Symposium*, Monastir, Tunisia.
- McDonell, V. G., L. Arellano, S. W. Lee, and G. S. Samuelsen (1996). Effect of hardware alignment on fuel distribution and combustion performance for a production engine fuel-injection assembly. *Proc. Combust. Inst.* *26*, 2725–2732.
- McDonell, V. G. and G. S. Samuelsen (2000). Measurement of fuel mixing and transport processes in gas turbine combustion. *Meas. Sci. Technol.* *11*, 870–886.
- Muruganandam, T. M., B. -H. Kim, M. R. Morrell, V. Nori, M. Patel, B. W. Romig, and J. M. Seitzman (2005). Optical equivalence ratio sensors for gas turbine combustors. *Proc. Combust. Inst.* *30*, 1601–1609.
- Naegeli, D. W. and L. G. Dodge (1991). Ignition study in a gas turbine combustor. *Combust. Sci. Technol.* *80*, 165–184.
- Nicholas, J. (Ed.) (2005). *The Jet Engine* (6th ed.). Rolls-Royce plc.
- Nygren, J., J. Hult, M. Richter, M. Aldén, M. Christensen, A. Hultqvist, and B. Johansson (2002). Three-dimensional laser-induced fluorescence of fuel distributions in an HCCI engine. *Proc. Combust. Inst.* *29*, 679–685.
- Odgers, J. and A. Coban (1977). Energy release to static gas from a 12-Joule high energy ignition system. *ASME Pap* (77-GT-18).
- Ossler, F., T. Metz, and M. Aldén (2001). Picosecond laser-induced fluorescence from gas-phase polycyclic aromatic hydrocarbons at elevated temperatures. I. Cell measurements. *Appl. Phys. B* *72*, 465–478.
- Papoulis, A. and S. U. Pillai (2002). *Probability, Random Variables and Stochastic Processes* (4th ed.). New York: McGraw-Hill.

- Penner, J. E., D. H. Lister, D. J. Griggs, D. J. Dokken, and M. McFarland (Eds.) (1999). *Aviation and the Global Atmosphere*. Cambridge: Cambridge University Press.
- Peters, J. E. and A. M. Mellor (1980). An ignition model for quiescent fuel sprays. *Combust. Flame* 38, 65–74.
- Polymeropoulos, C. E. and S. Das (1975). The effect of droplet size on the burning velocity of kerosene-air sprays. *Combust. Flame* 25, 247–257.
- Pope, S. B. (2000). *Turbulent Flows*. Cambridge: Cambridge University Press.
- Press, W. H., S. A. Teukolsky, W. T. Vetterling, and B. P. Flannery (2007). *Numerical Recipes - The Art of Scientific Computing* (3rd ed.). New York: Cambridge University Press.
- Pucher, G. and W. D. Allan (2004). Turbine fuel ignition and combustion facility for extremely low temperature conditions. In *Proc. ASME Turbo Expo*, Volume 1, pp. 385–392. ASME.
- Pucher, G., G. Wang, M. F. Bardon, D. P. Gardiner, A. M. Namet-Allah, and A. Benaissa (2001). Enhanced ignition systems for aircraft altitude relight. In *48th Annual Conference of the Canadian Aeronautics and Space Institute*, Volume 48, pp. 611–620.
- Rah, S.-C., A. F. Sarofim, and J. M. Beér (1986). Ignition and combustion of liquid fuel droplets. Part I: Impact on pollutant formation. *Combust. Sci. Technol.* 48, 273–284.
- Rao, K. V. L. and A. H. Lefebvre (1976). Minimum ignition energies in flowing kerosene-air mixtures. *Combust. Flame* 27, 1–20.
- Read, R. W., J. W. Rogerson, and S. Hochgreb (2008, Jan). Relight imaging at low temperature, low pressure conditions. In *46th AIAA Aerospace Sciences Meeting and Exhibit*. Reno, Nevada.

- Richards, G. A. and A. H. Lefebvre (1989). Turbulent flame speeds of hydrocarbon fuel droplets in air. *Combust. Flame* 78, 299–307.
- Rose, H. E. and T. Priede (1959). An investigation of the characteristics of spark discharges as employed in ignition experiments. *Proc. Combust. Inst.* 7, 454–463.
- Rosin, P. and E. Rammler (1933). The laws governing the fineness of powdered coal. *J. Inst. Fuel* 7, 29–36.
- Rowe, A. L. (2005, July). private communication, Performance Department, Rolls-Royce plc., PO Box 31, Derby, DE24 8BJ, UK.
- Schulz, C. and V. Sick (2005). Tracer-LIF diagnostics: quantitative measurement of fuel concentration, temperature and fuel/air ratio in practical combustion systems. *Prog. Energy Combust. Sci.* 31, 75–121.
- Seyfried, H., C. Brackmann, A. Lindholm, M. Linne, F. Barreras, and R. v. d. Bank (2007). Optical diagnostics applied to a gas turbine pilot burner. *AIAA J.* 45, 2702–2709.
- Sick, V. and B. D. Stojkovic (2001). Attenuation effects on imaging diagnostics of hollow-cone sprays. *Appl. Opt.* 40, 2435–2442.
- Singh, A. K. and C. E. Polymeropoulos (1986). Spark ignition of aerosols. *Proc. Combust. Inst.* 21, 513–519.
- Smith, J. D. and V. Sick (2005). High-speed fuel tracer fluorescence and OH radical chemiluminescence imaging in a spark-ignition direct-injection engine. *Appl. Opt.* 44, 6682–6691.
- Song, J., C. Li, N. S. Kim, and K. Ueda (2000). Passively Q-switched diode-pumped continuous-wave Nd:YAG-Cr<sup>4+</sup>:YAG laser with high peak power and high pulse energy. *Appl. Opt.* 39, 4954 – 4958.
- Stojkovic, B. D. and V. Sick (2001). Evolution and impingement of an automotive

- fuel spray investigated with simultaneous Mie/LIF techniques. *Appl. Phys. B* 73, 75–83.
- Su, L. K. and N. T. Clemens (1999). Planar measurements of the full three-dimensional scalar dissipation rate in gas-phase turbulent flows. *Exp. Fluids* 27, 507–521.
- Turns, S. R. (1996). *An Introduction to Combustion - Concepts and Applications*. New York: McGraw-Hill.
- UK Ministry of Defence (2002). Defence Standard 91-91.
- Warnatz, J., U. Maas, and R. W. Dibble (2006). *Combustion* (4th ed.). Berlin: Springer-Verlag.
- Xiong, T., Z. Huang, and Y. Wang (1981). Some factors affecting altitude relighting performance of turbojet engine combustor. *ASME Pap* (81-GT-49).
- Zhu, M., A. P. Dowling, and K. N. C. Bray (2001). Self-excited oscillations in combustors with spray atomizers. *J. Eng. Gas Turbines Power* 123, 779–786.